國立交通大學

環境工程研究所

碩 士 論 文

鋯離子摻雜與金沉積對中孔洞二氧化鈦微結構與光催化還原二氧化碳研究

Microstructures and photoreductive behavior of the mesoporous TiO_2 photocatalysts: Effect of Zr^{4+} doping and Au deposition

研 究 生：胥穎亞

指導教授：張淑閔　副教授

中 華 民 國 一 百 年 八 月

中文摘要

近年來全球暖化的影響日趨嚴重，光催化還原 CO_2 被視為最理想的解決技術之一，其靈感來於自然界植物的光合作用，不但處理溫室氣體的同時，也提供可利用的碳氫化合物做為能源。本研究成功利用蒸發誘導自組裝法(evaporation-induced self-assembly)合成中孔洞鋯離子摻雜二氧化鈦，並另以沉積沉澱法(deposition-precipitation)在材料表面沉積奈米金顆粒。此中孔洞材料以三區段共聚高分子(triblock copolymer)作為孔洞模板，具有高的比表面積($103-217 \, m^2 \, g^{-1}$)及較集中的孔徑分部。分析結果顯示，鋯摻雜濃度決定鋯離子在二氧化鈦結構中的分佈，以致影響二氧化鈦結構與物化特性，當 Zr/Ti 整體元素比為 0.02-0.04 時，鋯離子傾向摻雜於 TiO_2 晶粒表面，除提高孔洞熱穩定性外，也使 TiO_2 晶粒由 9.6nm 增加至 11.6 nm，能隙由 3.09 提高至 3.15 eV，然而鋯離子在高濃度時傾向摻雜於內部晶格，除抑制 TiO_2 結晶外，也致使光催化氧化 RhB 的活性變差，當 Zr/Ti 比例為 0.03 與 Au 負載量為 1.0 wt.%時，TiO_2 有最高的光催化氧化活性。CO_2 光催化還原實驗以水氣作為還原劑，以批次反應槽中進行，而甲烷為反應唯一的偵測產物。相較於修飾的光觸媒，單純二氧化鈦擁有較高的還原活性，於第一小時可產生 0.73 $\mu mole \, g^{-1}$ 甲烷量，並在第四小時達最高累積量 1.03 $\mu mole \, g^{-1}$，隨後甲烷氧化速率提升，於第八小時降低為 0.45 $\mu mole \, g^{-1}$。摻雜鋯離子與沈積 Au 奈米顆粒雖使 TiO_2 初始甲烷產率降低為 0.23 與 0.33 $\mu mole \, g^{-1}$，然而卻抑制 CH_4 被氧化的逆反應速率，經 8 小時反應後，Zr-doped TiO_2 (Zr/Ti=0.03)與 Au-TiO_2 樣品累積甲烷量可分別達 0.81 與 0.54 $\mu mole \, g^{-1}$。EPR 結果顯示電荷能有效於觸媒表面轉移至 CO_2 與 H_2O，因此產生難還原的中間產物是導致低還原效率的原因，Au 奈米顆粒為電荷再結合的媒介，對光催化反應會造成負面影響，而 Zr^{4+} 摻雜導入的缺陷能階決定其反應活性與逆反應速率。

I

Abstract

Photocatalytic reduction of CO_2 that mimics natural photosynthesis is a promising technology to both reduces the greenhouse gas emissions and provides alternative energy sources. In this study, mesoporous TiO_2 and Zr-doped TiO_2 photocatalysts were successfully synthesized using an EISA process. In addition, Au nanoparticles were loaded through a deposition-precipitation (DP) method. These mesostructured materials possess large surface areas of 103-217m^2 g^{-1} and narrow pore size distributions. The concentration of Zr^{4+} ions determines the distribution of the doped ions in the TiO_2 matrix, so as the microstructures and physicochemical properties. When the Zr/Ti ratio was in the range of 0.02-0.04, the Zr^{4+} ions were doped within the boundaries. As the result, the thermal stability of the porous structure was improved. In addition, the crystallite size of the TiO_2 increased from 9.6 to 11.6 nm, and the corresponding bandgap increased from 3.09 to 3.15 eV. When the Zr/Ti ratio was over 0.05, the Zr^{4+} ions tend to be doped within the TiO_2 lattice, thus inhibiting crystallization and photocatalytic activity of the doped TiO_2 samples. The TiO_2 samples exhibited the highest activity for RhB degradation when the Zr/Ti ratio and Au-loading were 0.03 and 1.0 wt.%, respectively. Photoreduction of CO_2 with water vapor was carried out in a batch system. CH_4 was the only detectable product in the reduction. The pure TiO_2 exhibited the highest activity over the modified samples. It generated 0.45 μmole g^{-1} CH_4 in the first hour, while the Zr-doped TiO_2 (Zr/Ti= 0.03) and 1.0 wt.% Au-TiO_2 produced 0.23 and 0.33 μmole g^{-1}, respectively. The pure TiO_2 reached to the highest CH_4 yield of 1.03 μmole g^{-1} at 4th hour. The yield subsequently reduced to 0.45 μmole g^{-1} at the 8th hour because of increased reoxidation rate. The reoxidation of CH_4 was suppressed by the Zr-doped and Au-loaded TiO_2 samples, which resulted in 0.81 and 0.54

μ mole g^{-1} CH$_4$ after 8 hr irradiation.　EPR results show that interfacial charge transfer from the catalysts to the adsorbed CO$_2$ and water is prompt.　The formation of the intermediates which have high reductive barriers determines the low reduction efficiency.　The Au nanoparticles serve as the mediator to promote charge recombination, thus are detrimental for the photocatalytic activity.　On the other hand, the impurities energy levels introduced by the doped Zr^{4+} ions within the bandgap dominate the reductive activity of the doped TiO$_2$ and reoxidation rate of CH$_4$.

謝誌

　　白駒過隙，歲月如梭，繁華終需落幕，三年的碩士生涯即將終了，研究歷程看似艱辛，一路走來卻也甘之如飴，學海波瀾，蒼蒼茫茫不見彼岸，承蒙指導教授　張淑閔老師敦敦教誨，所受心志之磨練與知識能力之訓練，兢兢業業看待每個任務，殫思極慮地面對所有問題，竭盡全力擔負起自己責任。感謝同步輻射中心詹丁山博士的指導，亦師亦兄，在專業領域上給我幫助，遇到挫折與瓶頸也在旁提供建議。無論在研討會亦或是論文研究上，謝謝董瑞安教授不斷費心提點，受到刺激而時刻反視自己，在實驗中不迷失應循的方向。也謝謝吳紀聖教授對論文悉心指正，在研究上不吝給予寶貴的意見及建議，使本篇論文得以更臻完整。此外感謝實驗室的大學姐們Evelyn、Claire 和Wes在研究上無私的教導，學長Brad有如我的大兄長一般，不論是實驗或生活都照顧著我，在苦悶的研究生涯帶來無限的歡樂，還有兩位像大姐般的Michelle和Joe，在我幾番波折的實驗裡總是給予幫助和建議，大學長Steel也對我這小學弟毫無保留的指點迷津。學妹Jiphi帶給這陽剛味十足的實驗室一點傻傻的氣氛，和學弟Welly和Jason短暫的相處，卻也留下美好的記憶。而Ashley、Ian和小老弟Jeremy，是我實驗室最麻吉的三個好學弟，漫漫長夜有你們的陪伴從來不覺得孤單，離開你們使我惆悵不捨。也謝謝重訓的夥伴，俊男、台客、玉米頭和Jessica狗狗，研究之餘不忘強身健體。最後要感謝的是我的家人，給我精神上的支持和衣食無虞的生活，親愛的爸媽和妹妹對我的包容，體諒我無法陪在你們的身邊，卻也不過問在忙些什麼，讓我求學之路上沒有壓力。最後謝謝始終陪伴在身邊的蘇小紅，任性的妳卻很貼心，時常聽我抱怨卻要忍受我的壞脾氣，對我的決定妳總是無悔的支持和體諒，默默的幫我解決大小雜事，使我全心全意專注在研究上，辛苦妳了。如果感謝的人太多了，那不如就謝天吧!

<div align="right">

穎亞　謹誌

中華民國一百年八月

</div>

IV

Content Index

Figure Index

Table Index

Chapter 1.   Introduction

1-1.   Motivation

At present, increasing of greenhouse gas (GHG) such as CO_2, CH_4, N_2O, HFCs, PFCs, and SF_6 are the primary cause of global warming in an atmosphere.   The GHG representing the largest contribution of human activities is carbon dioxide (CO_2), releasing from fossil fuel combustion.   Recently, many efforts are achieved to reduce CO_2 emissions by two approaches: (1) post-treatment of carbon capture and (2) geological sequestration of CO_2 technology.   Nevertheless, these process are requires significant energy further than generation and a long-term storage of CO_2 underground is regarded as precarious[1].   A replacement and more preferable method to reduce CO_2 are as a fuel feedstock with energy from free and abundant sources.   Photocatalytic reduction of CO_2 by using sunlight the largest carbon-free energy source that is inspired by the natural photosynthesis of plants.   It is not only to decrease the amount of green house gases but also to convert the available solar energy to supply energy.

The semiconductors utilize light energy as the excitation source; the photoexcited electrons reduce CO_2 with reductant on the surface and form chemical bond energy.   A variety of photocatalysts are used such as TiO_2, ZnO, SnO_2, WO_3, Fe_3O_4, CdS, and ZnS, among them, titanium dioxide (TiO_2) is considered the most convenient candidates because it shows an excellent photocatalytic activity, large band gap ($\sim$ 3.2 eV) and specific oxidation-reduction power as well as it is cheap, harmless and stably.   However, the rate of photoreduction and light utilization are still a major challenge for researchers.

Since the discovery of mesoporous M41S materials by Mobil Oil Company using the ammonium surfactants as a template in 1992[2-3], many different methods have been developed to design and synthesize of silica and non-silica mesoporous materials for their

potential application[4-7].   Numerous synthesis strategies are reported, the evaporation induced self-assembly (EISA) is combined with sol-gel chemistry and self-assembly process to prepare highly ordered mesoporous oxide[8].   This method has been used to tailor the dimensions and shapes by adjusting precursor composition and relative humidity for tuning of hydrolysis-condensation rate, since slow self-assembly of the inorganic network around the template permits the formation of a well-defined mesoporous structure.   The synthesis of mesoporous metal oxides with hexagonal structures was first adapted by Stucky's group employing amphiphilic poly (alkylene oxide) block copolymers as structure-directing agents[9].   In particular, mesoporous TiO_2 materials have attracted extensive attention in photocatalytic application or energy conversion in terms of high surface area of the mesoporous structure and three-dimensionally (3D) architecture contribute to high photocatalytic efficiency.

However, the thermal treatment causes the collapse of mesoporous framework and loss of surface area due to the crystallization and the subsequently growth, which strongly limited the extended applications of TiO_2.   Recently, the hybrid inorganic structure has proved more flexible and stable as-synthesized because of incomplete inorganic polymerization.   Among the various metal oxides coupling with TiO_2-base catalysts, ZrO_2-TiO_2 composites are one of the most promising materials[10-11] which have tunable construction and attractive photocatalysis properties.   In addition, an improvement of CO_2 conversion efficiency was demonstrated that the surface modification of TiO_2 with metals, which can inhibit the recombination of electron-hole pairs, extend the range of wavelength and control the selectivity of products.   An Au/TiO_2 catalyst by deposition-precipitation (DP) method has received increasing attention since the discovery by Haruta *et al.*[12], which gain a high dispersion of gold nanoparticle on any forms of support.   To the best of our knowledge, some research reported that CO_2 photoreduction using metal-doped TiO_2 on silica framework

exhibit high activity and selectivity for production[13-15].   Whereas both advantage (surface modification by dopant or deposition and mesoporous structure as the framework can enhance photoreduction of CO_2, it is necessary to develop the mechanism of surface modification and mesopores on the photocatalytic reduction of CO_2 over TiO_2.

1-2.   Objectives

This study aims to investigate the photocatalytic behavior of mesoporous Au-loaded and Zr-doped TiO_2 photocatalysts for reduction of gaseous CO_2 with H_2O in a gas-phase.   The mesostructural TiO_2 and ZrO_2-TiO_2 samples were fabricated through an evaporation induced self-assembly (EISA) process.   Then, the Au-nanoparticles were then deposit on the mesoporous photocatalysts using a deposition-precipitation (DP) method.   The physicochemical properties of Au-doped ZrO_2-TiO_2 catalysts were characterized by N_2 adsorption and desorption isothermal analysis, Transmission electronic microscopy (TEM), Powder X-ray diffractometer (PXRD), X-ray photoelectron spectroscopy (XPS), UV-vis spectrophotometer and Thermo gravimetric analysis/Differential scanning calorimetry (TGA/DSC).   The adsorption and photocatalytic reduction tests of CO_2 were carried out in a batch reactor with water vapor as the reactants under the UV irradiation.   In addition, the charge trapping and transference were analyzed using electron paramagnetic resonance (EPR). X-ray absorption spectroscopy (XAS) was applied to correlate the microstructure and mechanism of photoreduction with several parameters, such as gold loading, support structure, pretreatment and condition of experiment (e.g. temperature and humidity).

Chapter 2.   Background and Theory

2-1.   Photocatalysis

2-1-1.   Principle of photocatalysis

Since 1972, Fujishima and Honda discovered the phenomena of photocatalytic splitting of water on semiconducting TiO_2 e1ectrodes under UV light[16], more attention has been focused on this material as a practical photocatalyst.   Semiconductors such as TiO_2, ZrO_2, SnO_2, ZnO, CdS and WO_3 have been applied in energy and environmental fields for photon-to-electricity conversion, water splitting, hydrogen storage, photocatalysis and sensing[17].   Unlike metals, which have a continuum of electronic states, semiconductors exhibit a void energy region (band gap) that extends from the top of the filled valence band (VB) to the bottom of the vacant conduction band (CB)[18].   Figure 2-1 illustrates the excitation of an electron from the VB to the CB initiated by the absorption of photons with energy equal to or greater than the band gap of the semiconductor.   The separated electron and hole could migrate to the surface (pathway A and B) or undergo recombination in the volume and at the surface (pathway C and D)[19].

The detailed mechanisms of the photocatalytic oxidation or reduction reactions on semiconductors by UV illumination are shown in Figure 2-2 and presented below stepwise[20]: Photocatalysis involves the generation of electron-hole pairs by UV absorption and the charge carriers can migrate rapidly to the surfaces of catalyst where they are oxidized or reduced with suitable substrates (Step 1).   The trapped hole can react with the chemisorbed OH group or the H_2O molecular on the surface to produce OH radicals (Step 2) or accept electrons from adsorbed organic compounds to convert them directly to radicals (Step 3).   In addition, oxygen or other oxidants including CO_2 can act as an efficient electron scavenger to

form superoxide radical (Step 4) or other reduced radicals (Step 5). The fundamental processes of photocatalysis involving with TiO_2 can be summarized as following:[21]

Charge carrier generation:

$$TiO_2 + hv \rightarrow h^+ + e^- \tag{2-1}$$

Charge carrier trapping:

$$e^- + Ti^{IV}OH \rightarrow Ti^{III}OH \tag{2-2}$$

$$h^+ + Ti^{IV}OH \rightarrow \left(Ti^{IV}OH^\bullet\right)^+ \tag{2-3}$$

Charge carrier recombination:

$$h^+ + e^- \rightarrow Energy \tag{2-4}$$

$$e^- + \left(Ti^{IV}OH^\bullet\right)^+ \rightarrow Ti^{IV}OH \tag{2-5}$$

$$h^+ + Ti^{III}OH \rightarrow Ti^{IV}OH \tag{2-6}$$

Interfacial charge transfer:

$$\left(Ti^{IV}OH^\bullet\right)^+ + Reductant \rightarrow Ti^{IV}OH + Reductant^{\bullet+} \tag{2-7}$$

$$Ti^{III}OH + Oxidant \rightarrow Ti^{IV}OH + Oxidant^{\bullet-} \tag{2-8}$$
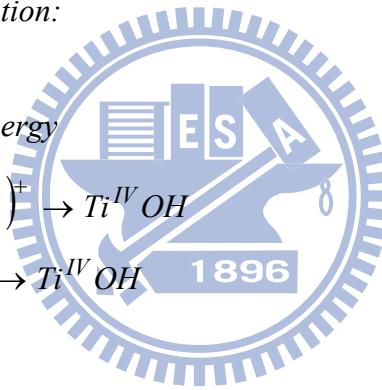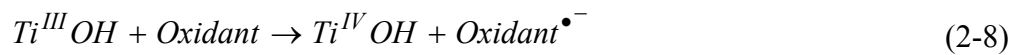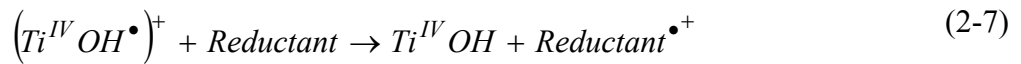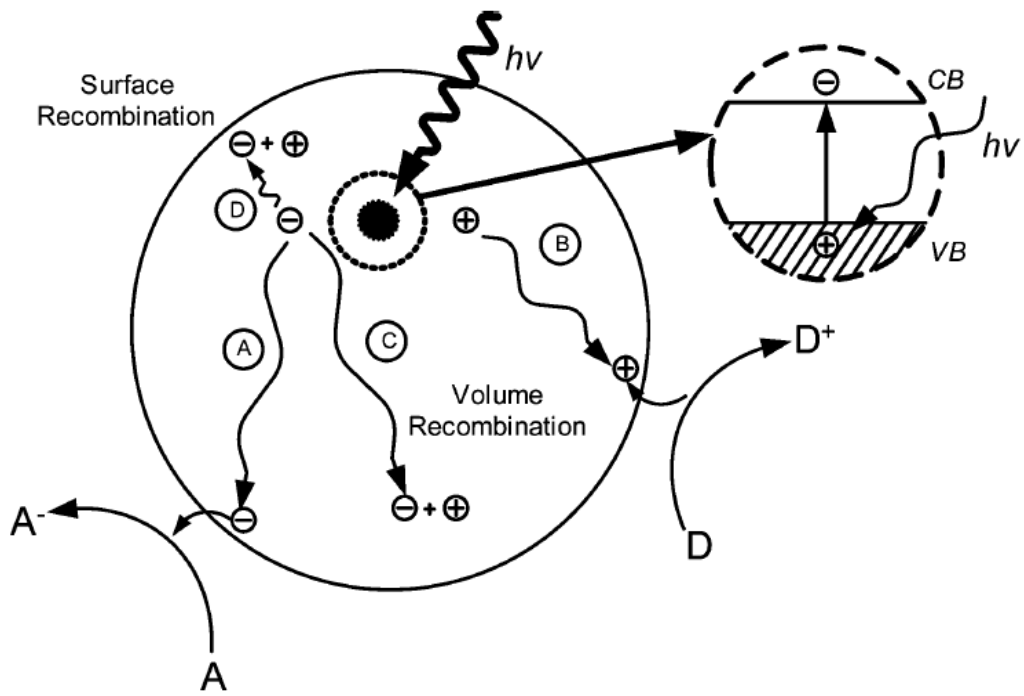
Figure 2-1 Schematic photoexcitation in a solid followed by excitation events.[19]
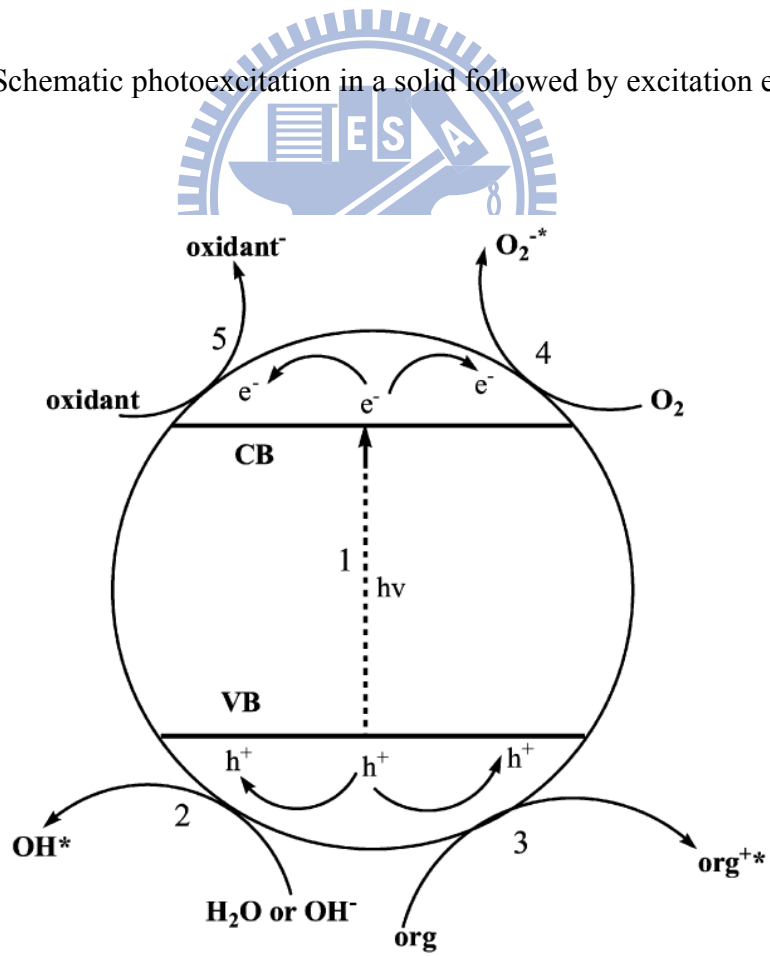
Figure 2-2 Mechanism of photocatalysis on semiconductors exposed to light irradiation.[20]

Contact between an n-type semiconductors such as TiO_2 and metals generally involves a redistribution of electric charges and the formation of a Schottky barrier as shown in Figure 2-3.   The Schottky barrier formed at the metal-semiconductor interface leads the metal and the semiconductor exhibiting excess negative charges and positive charges, respectively. Separation of charge carriers from the barrier region can serve as an efficient electron trap to prevent the electron-hole recombination on photocatalysts.   The height of the barrier (ϕ_b) is given by:

$$\phi_b = \phi_m - E_x \qquad\qquad (2\text{-}9)$$

where ϕ_b is the work function and E_x is the electron affinity.   Figure 2-4 illustrates the properties of Schottky barrier formed at a metal-semiconductor junction.   After migration of the photoexcited electron to the surface, electron trapping suppresses the recombination.
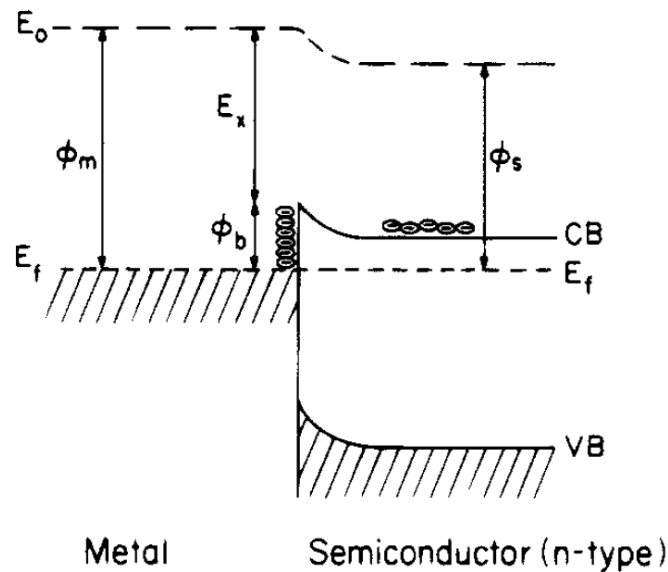
Figure 2-3 Schematic of a Schottky barrier.[19]
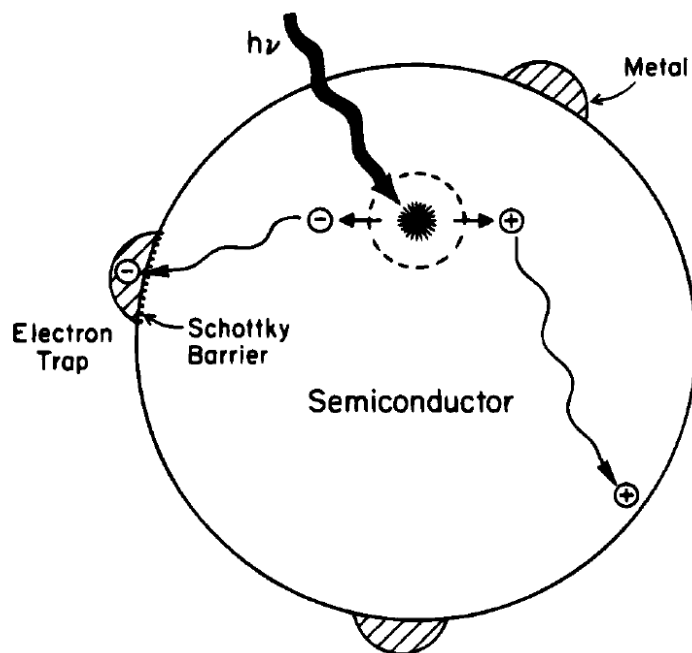
Figure 2-4 Schottky barriers on the surface of metal-semiconductor particle.[19]

2-1-2. Material properties of TiO$_2$

Semiconductors participate in a variety of photocatalytic reactions including oxidative degradation of organics, reduction of metal ions and evolution of hydrogen from water to remedy the problem of chemical waste and energy renewal. TiO$_2$ is the most investigated semiconductor which has large potential in photocatalysis, solar cells, sensor and photochromism because of its low cost, commercial availability, nontoxicity, chemical stability, ease of handling, high photocorrosion resistance and suitable optical/electronic qualities. This ability of TiO$_2$ is related to its optical properties. TiO$_2$ possesses a wide band gap (3.0 eV for the rutile phase and 3.2 eV for the anatase phase, as shown in Figure 2-5) that absorbs photons in the ultraviolet region, thus limiting its application under visible light.
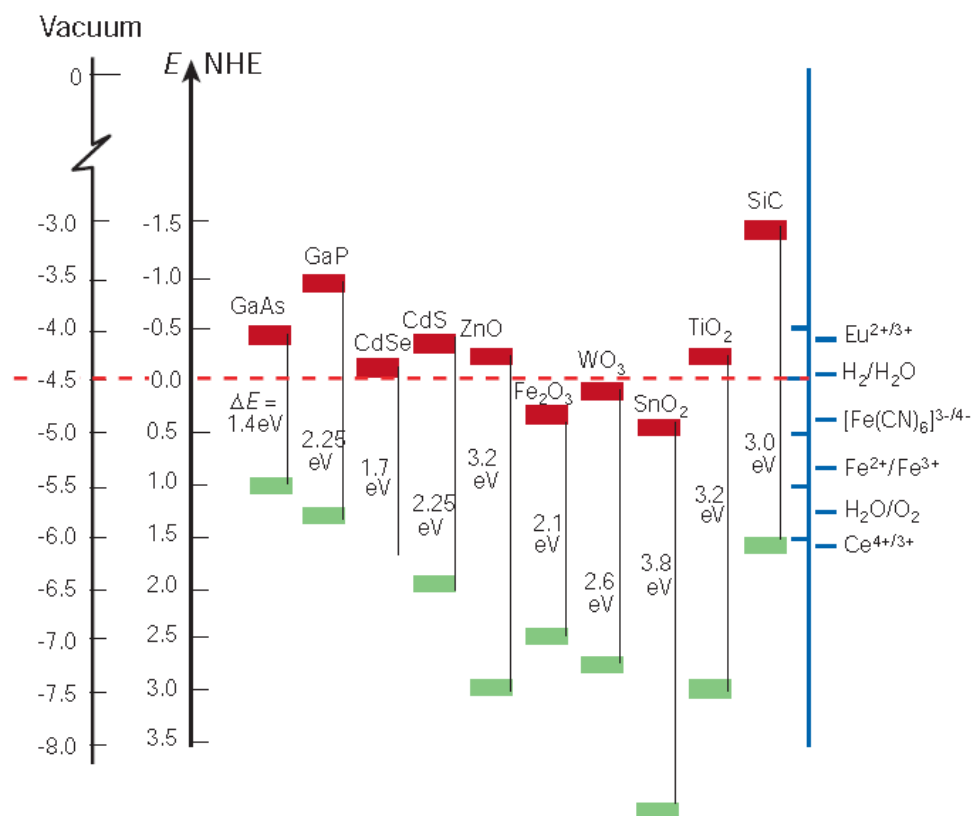
Figure 2-5 Energies of various semiconductors in aqueous electrolytes at pH= 1.[22]

In addition, the photocatalytic activity of TiO_2 is highly dependent on its porosity, surface area, bulk structure, particle size, crystal phase and crystallinity. TiO_2 has three polymorphs: anatase, rutile and brokite, and anatase is the most active phase[17]. Figure 2-6 shows the unit cell structure of rutile and anatase TiO_2 which are commonly used in photocatalysis. The basic building block consists of a titanium atom surrounded by a more or less distorted octahedron of six oxygen atoms[23]. These differences in lattice structures cause different mass densities and electronic band structures between the two crystals of TiO_2.
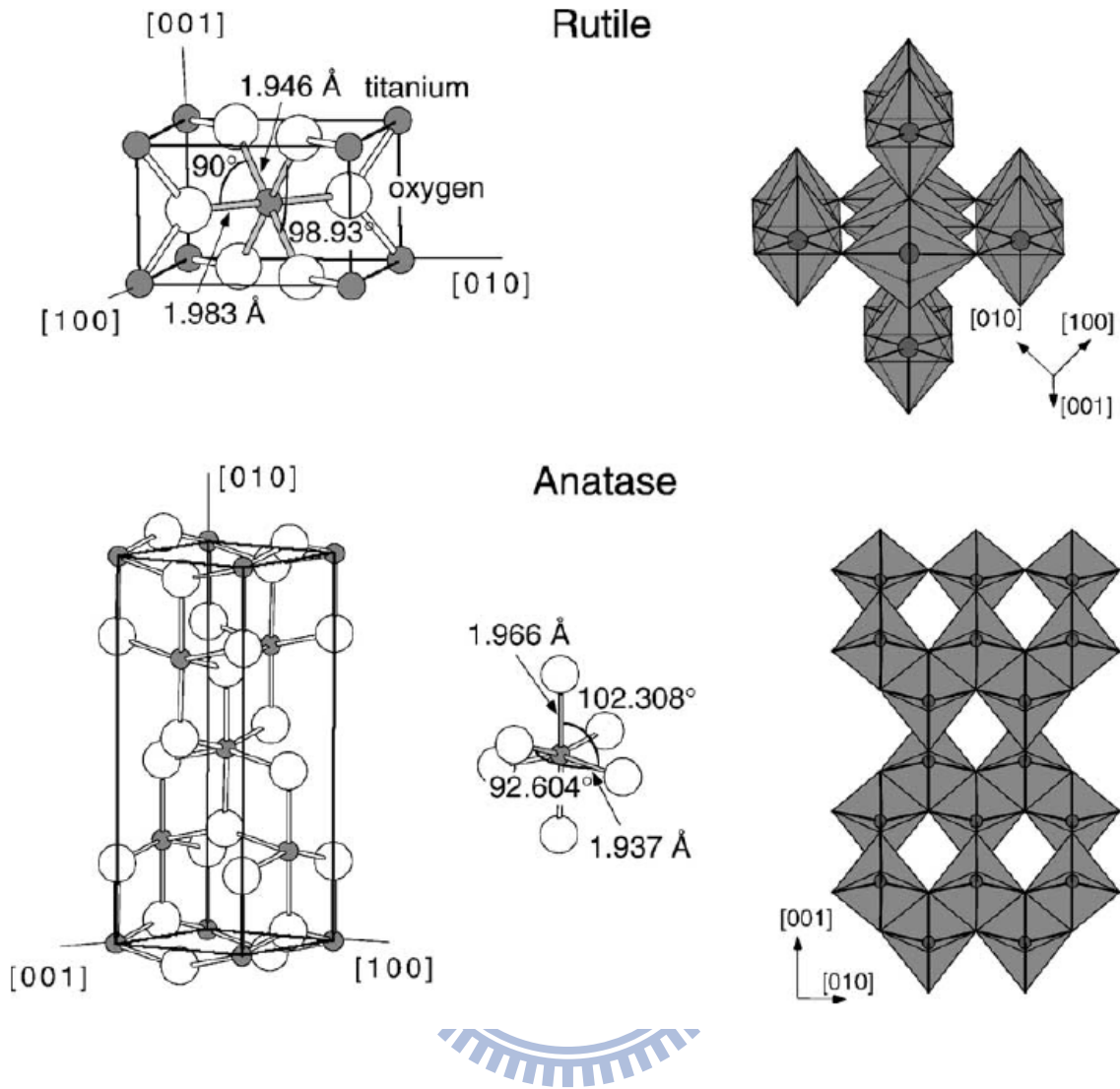
Figure 2-6 Bulk structure of rutile and anatase TiO$_2$.[24]

2-2.   Sol-gel method

The sol-gel processing of inorganic ceramic materials refers to the hydrolysis and condensation of alkoxide-based precursors have been extremely investigated since the earliest study of Ebelman *et al.*[25].   TiO$_2$ have been synthesized with the sol-gel method via an acid-catalyzed hydrolysis with titania precursor followed by condensation[26].   Sol-gel process offers a facile and available method for synthesis of nanoparticle or thin film that are either unitary or hybrid metal oxides, offers many advantages including excellent control and

selective of precursor solutions, easily modification of composition, customizable microstructure, relatively low reaction temperatures, the practicability of coating deposition on substrates, and simple and inexpensive equipment. The processing procedures can be characterized by a series of distinct steps (Figure 2-7):[27-28]

Step 1:   *Mixing*.   Stabilized solutions of the alkoxide or solvated metal precursor (the *sol)*, and hydrolysis and condensation reactions were initiated by mixing with precursor and water.

Step 2:   *Gelation*.   At gelation, the formation of an oxide or alcohol bridged network (the *gel*) by a polycondensation or polyesterification reaction was increased in the viscosity increases sharply of the solution.

Step 3:   *Aging*.   Aging of the gel (*syneresis*), the polycondensation reactions continue until the gel transforms into a solid mass, follow by contracting of the gel and expulsion of solvent from the gel pores.   The aging process of gels must develop to the prevention of cracks during drying because of Ostwald ripening and phase transformations may occur concurrently with syneresis.

Step 4:   *Dring*.   This process is complicated due to fundamental changes in the structure of the gel during drying the water or solvent is removed from the gel pore network. If isolated by thermal evaporation, the resulting product is termed a *xerogel*.   If the liquid is dried under hypercritical conditions an *aerogel* has been prepared with lower density.

Step 5:   *Dehydration or stabilization*.   The removal of surface-bound (M-OH) groups are removed from the pore network by calcinations at temperature up to 800 °C results in a stabilizing the gel against rehydration.

Step 6: *Densification.* Heating the porous gel at high temperatures (> 800 °C) causes densification and decomposition to occur. The pores of the gel network are collapsed and remaining organic species are volatilized.

Hydrolysis:

$$\text{Cl-M(Cl)(Cl)(Cl)-Cl} + 4H_2O \longrightarrow \text{HO-M(OH)(OH)(OH)-OH} + 4HCl \tag{2-10}$$

$$\text{OR-M(OR)(OR)(OR)-OR} + 4H_2O \longrightarrow \text{HO-M(OH)(OH)(OH)-OH} + 4HOR \tag{2-11}$$

Condensation:

$$\text{HO-M(OH)(OH)-OH} + \text{HO-M(OH)(OH)-OH} \longrightarrow \text{HO-M(OH)(OH)-O-M(OH)(OH)-OH} + H_2O \tag{2-12}$$

Gelation:

$$\tag{2-13}$$

+ $2H_2O$
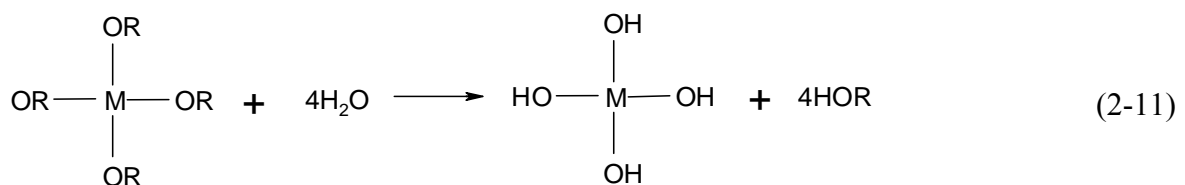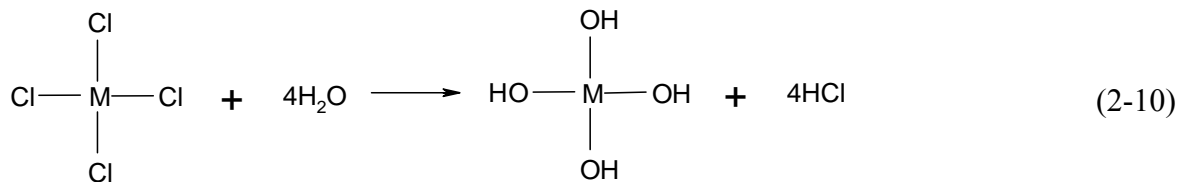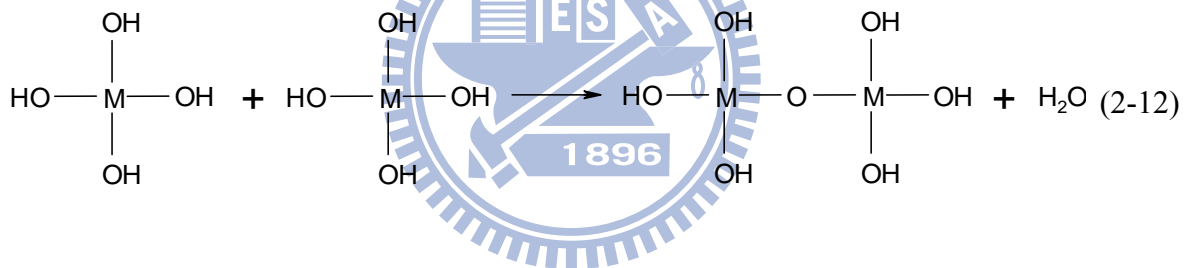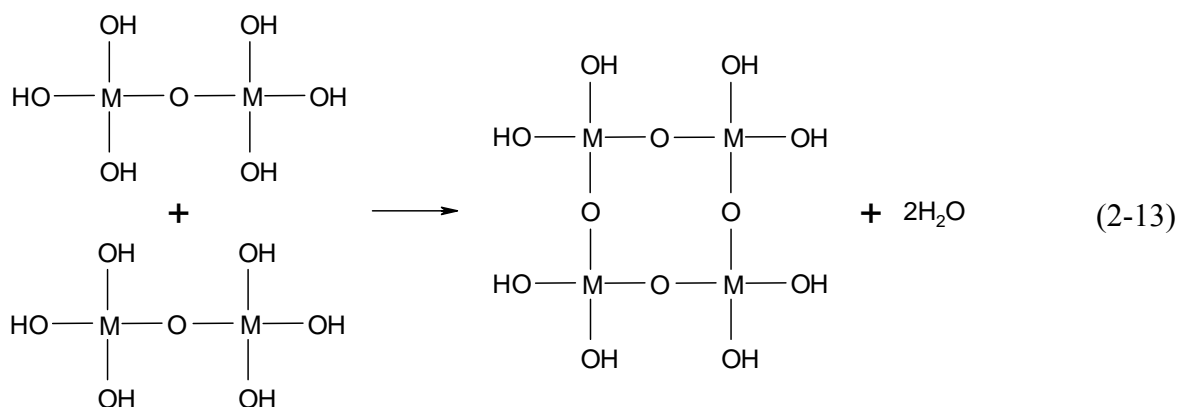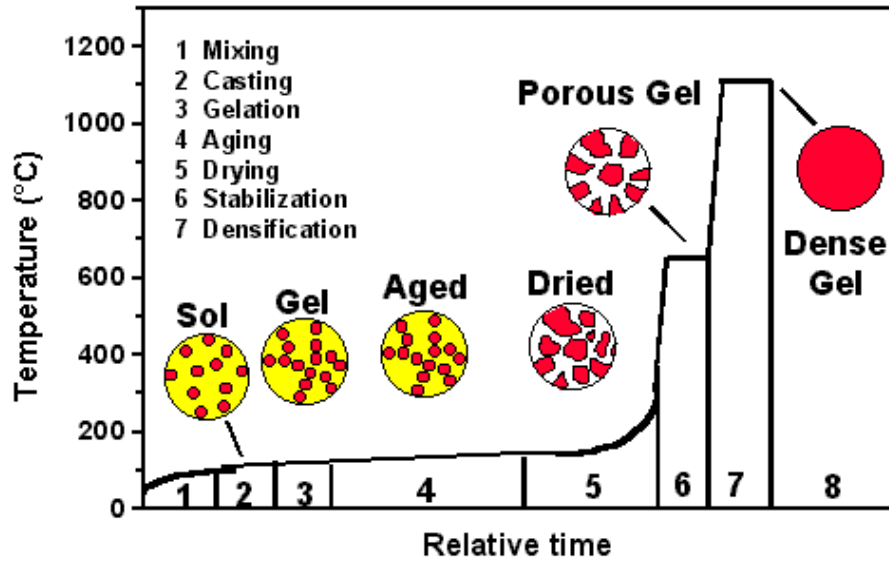
Figure 2-7 Gel-glass process sequence.[27]

2-3.   Mesoporous materials

Since the amazing discovery of zeolite with tailored pore structures and high surface areas, a variety of ordered porous materials have many applications in the areas of adsorption and catalysis[29].   According to the classical definition made by IUPAC, the porous structures can be divided into three categories: microporous ($d < 2$ nm), mesoporous (2 nm < $d < 50$ nm) and macroporous materials ($d > 50$ nm), based on their pore diameter.   Some examples are listed in Table 2-1

Table 2-1 Examples of porous materials and showing the pore size domains.[30]

Pore size regimes	Definition	Example	Actual size range
macroporous	$d > 500$ Å	glasses	> 500 Å
		aerogels	> 100 Å
mesoporous	20 Å $< d < 500$ Å	pillared layered clays	10 Å, 100 Å (a)
		M41S	16-100 Å
		zeolites, zeotypes	< 14.2 Å
microporous	$d < 20$ Å	activated carbon	Å

(a) Bimodal pore size distribution

2-3-1. Mechanisms and templates

In 1992, the synthesis of mesoporous molecular sieves as aluminosilicate M41S was discovered by scientist in Mobil Oil Corporation. The synthesis involves the co-condensation of an anionic species with cationic surfactants (S^+I^-)[3]. MCM-41, the remarkable one of the members of M41S, is prepared with a cationic surfactant, cetyltrimethylammonium $(C_{16}TMA^+)$, as a template (as shown in Figure 2-8)[31]. It possesses a highly ordered hexagonal arrangement of uniform pores whose dimensions can be confirmed with a varying channel (15-100 Å) and high surface area (> 1000 m^2g^{-1}). Other related phases such as MCM-48 and MCM-50 have a cubic and lamellar mesostructure, respectively (Table 2-2, Figure 2-9).
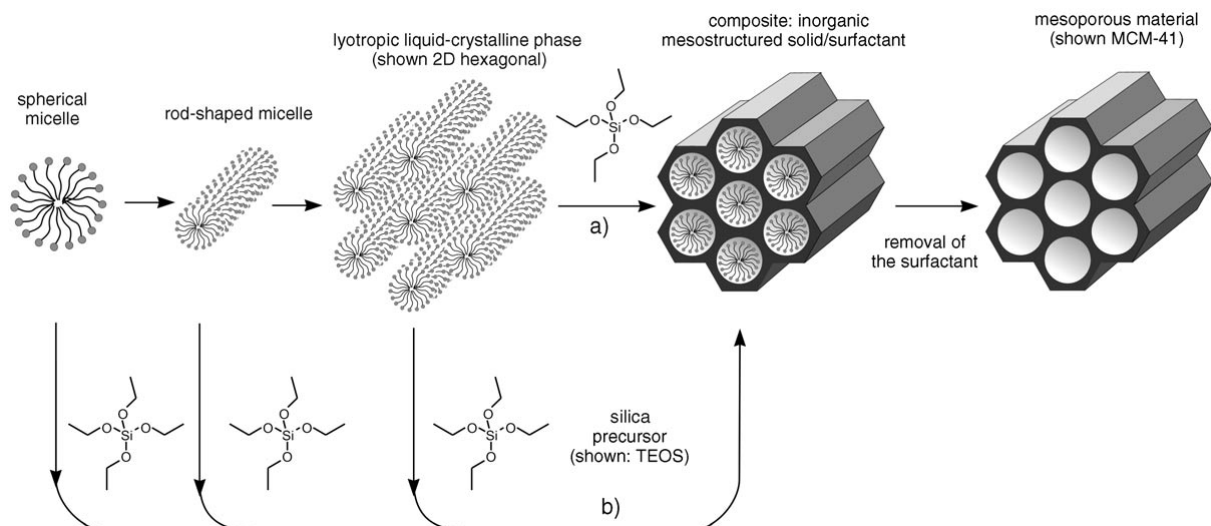
Figure 2-8 Two possible pathways for the liquid-crystal templating mechanism of MCM-41.[32]

Table 2-2 Mesophases of silicate molecular sieves and synthesis parameters.[33]

Name	Mesophase	Space group	Parameter
MCM-41	hexagonal	*P6m*	[surfactant] / [Si] < 1
MCM-48	cubic	*Ia3d*	[surfactant] / [Si] < 1-1.5
MCM-50	lamellar	*P2*	[surfactant] / [Si] < 1.2-2

(a) (b) (c)
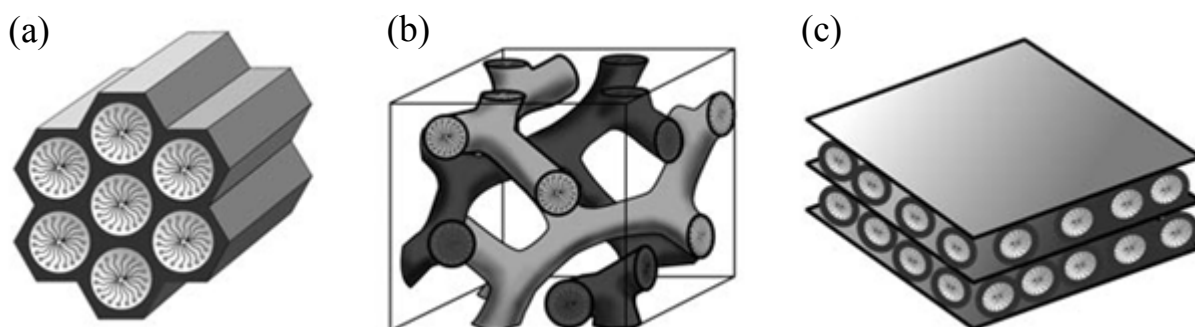
Figure 2-9 Illustrations of mesoporous M41S materials: (a) MCM-41, (b) MCM-48, and (c) MCM-50.[32]

Nonionic polymeric templates are later used in the synthesis of mesoporous silicas and other mesoporous oxides (as shown in Figure 2-10)[34]. The most useful groups of the surfactants are the triblock copolymers including poly(alkylene oxide)$_x$-poly(propylene oxide)$_y$-poly(ethylene oxide)$_x$, (PEO)$_x$(PPO)$_y$(PEO)$_x$, (trade name: Pluronic)[35-36]. These block co-polymers show excellent abilities on tailoring varied porous structure (Table 2-3), non-toxicity, specific interfacial character, commercial availability, biodegradability and low cost. The preparations of well-ordered hexagonal mesoporous material (SBA-15, Santa B Arbara No. 15) are achieved by using the amphiphilic block copolymers as structure-directing agents[37]. Compared to M41S and other silicates, SBA-15 exhibits high thermal stability which is contributed by tunable large pore sizes (50-300 Å) and thick wall (31-64 Å). Moreover, it allows more remarkable applications for the preparation of mesoporous oxides, such as Al_2O_3, TiO_2, ZrO_2 HfO_2, Nb_2O_5, Ta_2O_5, WO_3 and SnO_2[38-39], as well as a variety of mixture (e.g., $SiAlO_{3.5}$, $SiTiO_4$, Al_2TiO_5, $ZrTiO_4$ and ZrW_2O_8)[40].
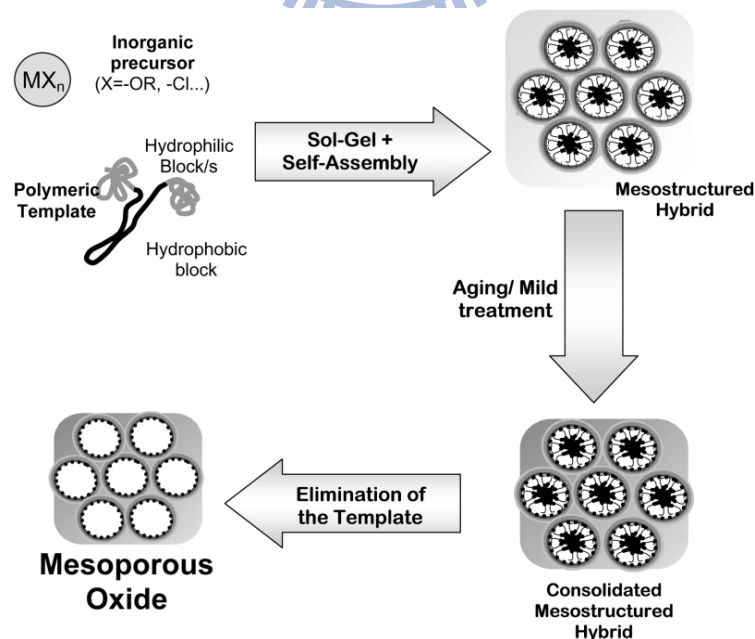
Figure 2-10 Schematic view of the mesoporous oxide prepared with polymeric template.[41]

Table 2-3 Mesophases and synthesis parameters of triblock copolymers.[37]

Name	Mesophase	Space group	Example
EO/PO < 0.07	hexagonal [a] lamellar [b]	$P6m$	$EO_5PO_{70}EO_5$
EO/PO =0.07-1.5	hexagonal	$P6m$	$EO_{20}PO_{70}EO_{20}$
EO/PO > 1.5	cubic	$Im\bar{3}m$	$EO_{80}PO_{30}O_{80}$

(a)　At low concentrations (0.5-1 wt %) and [b] higher concentrations (2-5 wt %)

2-3-2.　Mesoporous TiO_2

Recently, mesostructural metal oxides, which have high specific surface areas and pore volumes, as well as narrow pore size distributions where offer more active sites for catalytic reaction to occur, have attracted much attention.　For the photocatalytic applications of TiO_2, anatase is necessary since this phase shows high photocatalytic activity.　Unfortunately, synthesis of mesoporous TiO_2 is much more complicated compared to silica because titania precursor shows a high reactivity toward hydrolysis and condensation which leads a distorted structure.　The preparation of mesoporous TiO_2 powders and films using sol-gel method[42-45], hydrothermal method[46-48], microwave method[49], sonochemical method[50-51] and evaporation induced self-assembly (EISA) method[52-54] have been extensively investigated.　The first study of hexagonal arranged mesoporous TiO_2 prepared via a modified sol-gel method in the presence of alkyl phosphate surfactant as template was developed by Antonelli *et al.*[38].　Afterwards, they used dodecylamines as the template to prepare phosphorus-free mesostructured TiO_2[55].　Yoshitake *et al.*[56] also used amine surfactant and improved by a chemical vapor deposition (CVD) treatment with titania

precursor to stabilize the structure. Trong[57] used acetylacetone to control the condensation of TiO_2 and simply prepared lamellar and hexagonal mesoporous TiO_2 in the presence of cetyltrimethylammonium chloride ($C_{16}TMA^+Cl^-$). Pure titania and silica incorporated titania mesoporous materials have been successfully synthesized by Zheng *et al.*[58], who used urea as a template. Because ionic surfactants present strong interactions with inorganic walls, it is challenging to remove the surfactants from the metal oxides using extraction. And, the collapse of the inorganic structure may occur when the calcination is employed for surfactant removal. Thus, nonionic block copolymer appeared to be an excellent candidate for the formation of weak hydrogen bond with inorganic framework and surfactant composites. Uses of tripolymeric template to direct organization of mesoporous TiO_2 with worm-like distorted or hexagonal ordered structure are shown in Figure 2-11.
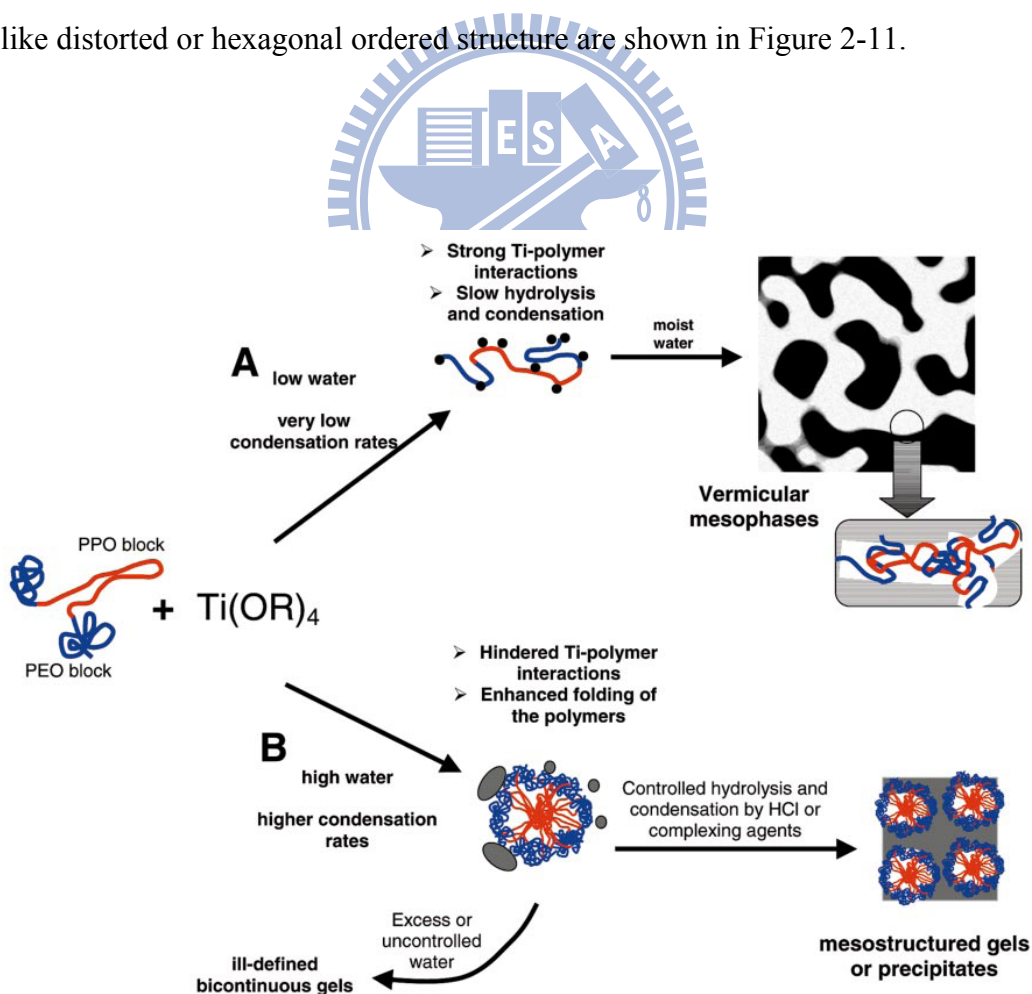
Figure 2-11 Mechanistic schemes for mesoporous TiO_2 with triblock copolymer.[59]

The nonionic block copolymers like $(PEO)_x(PPO)_y(PEO)_x$ have the additional advantage of relatively thick inorganic pore wall, improving the thermal stability of the material. Stucky et al.[9] used amphiphilic poly(alkylene oxide) block copolymers as structure-directing agents and $TiCl_4$ as the titania source to prepare mesostructral TiO_2. Calleja et al.[42] reported the synthesis of mesoporous TiO_2 with highest specific surface areas (> 300 m^2g^{-1}) of using the Pluronic P123 and titanium isopropoxide as the initial reaction agents to prepare a mesoporous TiO_2. Recently, evaporation induced self-assembly (EISA) has been investigated for the production of mesoporpous TiO_2[52]. EISA process controls and synchronizes the aggregation of micelles with the condensation of the inorganic framework, giving rise to well-defined porous structure. A succinct summary of some important works in this field are presented in Table 2-4.

However, pure TiO_2 materials usually have poor thermal stability and relatively low quantum efficiency, which strongly restricts its applications in photocatalysis. Combination with others metal oxides are the alternative approach for property tuning to enhance activity due to structural and electronic modification[60]. TiO_2-SiO_2 materials have been extensively used at first as catalysts and supports for a wide variety of reactions[61]. These mixed materials are not only taken advantage of both photocatalysis and mechanical stability, but also generation of new acid sites. Thus, a great deal of TiO_2-based binary metal oxides such as TiO_2-Al_2O_3, TiO_2-SnO_2, TiO_2-ZrO_2, TiO_2-WO_3 and TiO_2-P_2O_5 have been reported, among them, TiO_2-ZrO_2 is one of the most promising photocatalyst for tunable composition, abundant phases and more attractive photocatalysis properties. In these works, Zr^{4+} ions were mainly doped in the surface of TiO_2, the specific redox potential, higher surface area, stronger surface acidity and creation of surface defects are proposed as the reason for the improvement in the photocatalytic performance[62-64]. Furthermore, the first synthesis of mesoporous Zr-TiO_y using triblock copolymers as templates with hexagonal structure was

prepared by Stucky et al.[9]. Since then many efforts have been devoted to the fabrication of mesoporous TiO_2-ZrO_2 materials and some dramatically applications have been achieved[65-67]. Recently, Yuan *et al.*[68] published an efficient approach to fabricate ordered mesoporous TiO_2-ZrO_2 composites through evaporation induced self-assembly (EISA) process by using amphiphilic triblock copolymer F127 and P123 as structure-directing agents. Overview of all mesoporous TiO_2-ZrO_2, it is a challenge to avoid entrance of Zr^{4+} ions into bulk inside, which may facilitate the recombination of electron-hole pairs then reducing the photocatalytic activity.
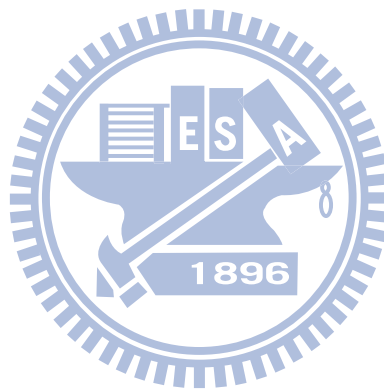
Table 2-4 Preparation of mesoporous TiO_2

Method	Ti precursor	Surfactant	Surface area (m^2/g)	Pore size (nm)	Ref
Sol-Gel	Tantalum ethoxide	Octadecylamine	Over 500	2.0-4.0	[55]
	Titanium isopropoxide	Pluronic P123	166-381	6.3-2.8	[42]
	Titanium isopropoxide	Pluronic P123	205	4.4	[43]
	Titanium isopropoxide	Triton X-100	187-487	4.6-3.8	[45]
	Titanium ethoxide	Pluronic P123	134-204	8.0-5.5	[44]
	Titanium isopropoxide	Pluronic P123	210-260	5.6-5.2	[69]
	Titanium isopropoxide	CTAB	123.8	12.6	[70]
Hydrothermal	Titanium isopropoxide	Pluronic P123	98.7-152.3	8.01-6.19	[71]
	Titanium *n*-butoxide	-	186.7-295.2	7.23-4.74	[46]
	Titanium sulfate	PEG 200	172.4-234.1	9.94-6.31	[72]
	Titanium sulfate	CTAB	317.5	2.5	[48]
	Titanium isopropoxide	Pluronic P123	87-295	10.1-6.9	[73]
Microwave	Titanium isopropoxide	Tetradecylamine	243-622	0.32-0.27	[49]
Sonochemical	Titanium isopropoxide	CTAB	853	1.5	[50]
	Titanium isopropoxide	Pluronic P123	112-128	6.7-9.3	[51]
EISA	Titanium isopropoxide	CTAB	260-384	2.5-1.9	[52]
	Titanium *n*-butoxide	Pluronic P123	115-151	14.0-8.3	[74]
	Titanium isopropoxide	CTAB	573	2.5	[54]

2-3-3. Evaporation induced self-assembly (EISA) process

Self-assembly (SA) can be generally defined as the spontaneous and reversible organization of molecular materials through non-covalent interactions (e.g. hydrogen bonding, Van der Waals forces, electrostatic forces, π-π interactions) with no external intervention. Typically examples of SA in materials include the formation of molecular crystals, colloids, lipid bilayer and molecular polymers with periodic assemblies[75].   Above the critical micelle concentration (CMC) in liquid phase, the amphiphilic surfactant was assembled into micelles, spherical or cylindrical structures that the hydrophilic parts of the surfactant in contact with solution while the hydrophobic parts within the interior of micelle (Figure 2-12). Further increases the concentration of surfactant result in the self-organization of micelles into well-ordered hexagonal, cubic, or lamellar mesostructures[8].

Mann *et al.*[76] successful developed a versatile approaches to the synthesis of organized inorganic materials, which present arrays of pores of tailored dimensions and a great variety of shapes.   This method was composed of four steps, including the (1) self-assembled templates (*transcriptive synthesis*), (2) cooperative assemblies of surfactant and inorganic block (*synergistic synthesis*), (3) spatially restricted reaction fields (*morphosynthesis*), and (4) combinations of these approaches (*integrative synthesis*) into sol-gel chemistry.   For example, using cetyltrimethylammonium bromide as template (CTAB), Sanchez *et al.*[52] demonstrated the formation of titania nanobuilding blocks (NBB), which are self-assembled within a liquid-crystal-like mesostructure around the micelles (Figure 2-13).
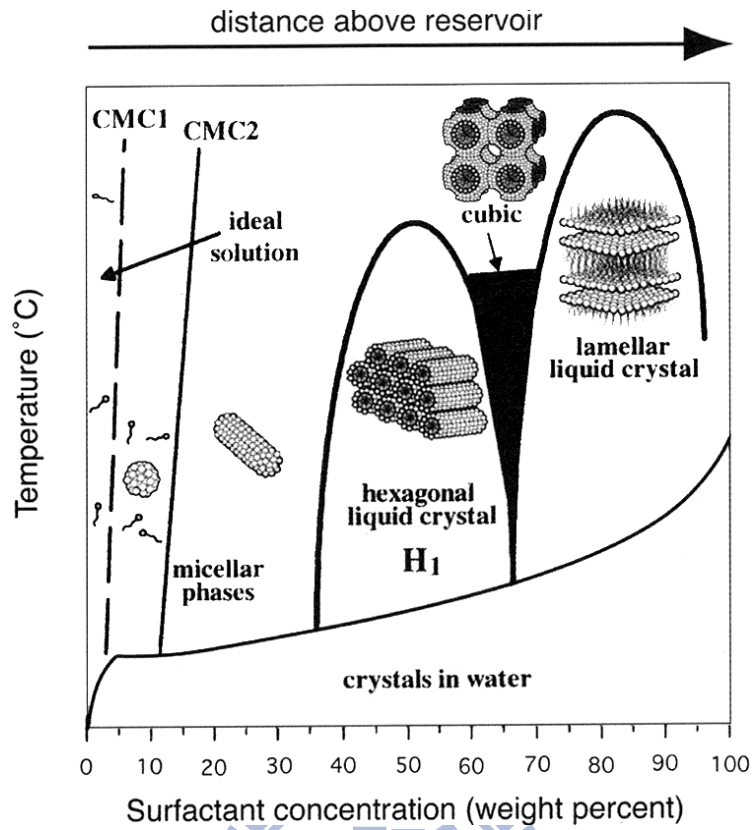
Figure 2-12 Schematic phase diagrams for the surfactant in solution.[77]
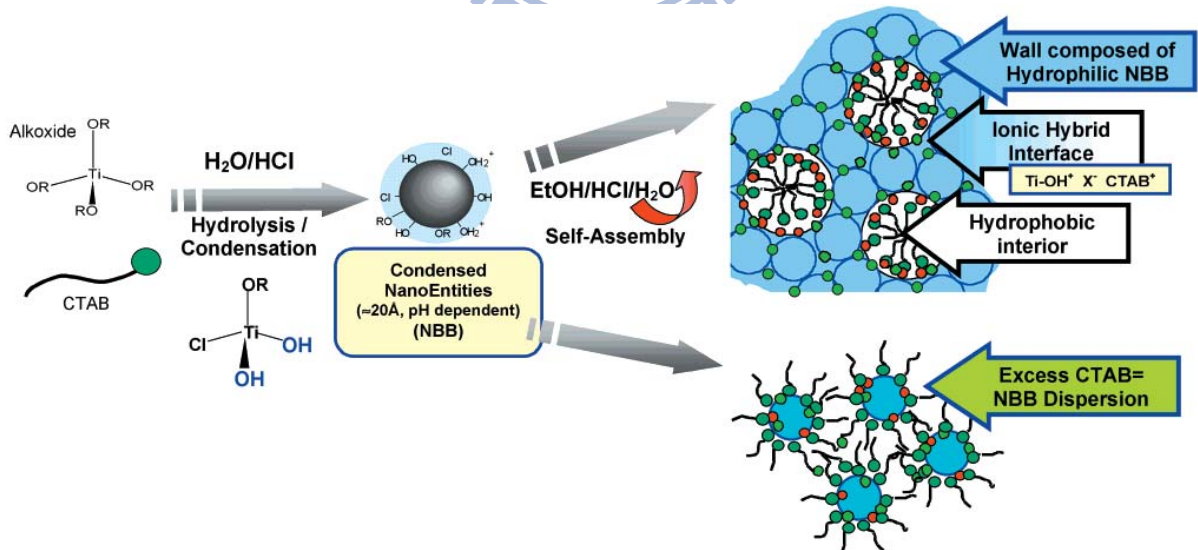
Figure 2-13 Formation pathways of TiO$_2$/CTAB hybrid nanobuilding blocks.[52]

2-4.   Surface modification

TiO$_2$ is regarded as the most efficient and environmental friendly photocatalyst. However, its large band gap (~3.2 eV) limits TiO$_2$ only active in the ultraviolet region which is lower than 10% of the overall solar intensity. Rapid recombination of the photoexcited electron-hole pairs at the surface also inhibits the quantum efficiency. To improve the photocatalytic activity, surface modification of TiO$_2$ is employed. So far, three benefits of the modifications to photocatalytic activity have been studied: (1) inhibiting recombination of electron and hole by increasing the charge separation, (2) increasing the wavelength response range and (3) changing the selectivity or yield of a particular product.

In recent years, the modification of TiO$_2$ with transition metals[78-80] (V, Cr, Mn, Fe, Co, Ni and Cu) and noble metals[81-82] (Au, Ag, Pt, Pd, Rh and Ru) for improved photocatalytic performance have been widely studied. The metal doped semiconductor exhibits a particular variation in the Fermi level to create the Schottky barrier. Kamat *et al.*[83] observed a greater photocatalytic reduction efficiency and higher photocurrent generation of Au/TiO$_2$ nanocomposites by shifting the Fermi level. Since Haruta *et al.*[84] developed a dramatic preparation method of golden titania catalysts by deposition-precipitation (DP) with NaOH as precipitating agent. The Au/TiO$_2$ materials have received particular attention owing to its peculiar properties which is sensitive to gold concentration, pH value, temperature of the solution and calcination temperature. Neither Au nor the TiO$_2$ support is catalytically active for CO oxidation at low temperature, but Au/TiO$_2$ system shows a synergetic effect for the reaction[85]. In the literature, these catalysts have been completely evaluated that the activity for CO oxidation is strongly dependent on the size of gold particles. Schüth *et al.*[86] investigated the influence of the synthesis condition on different supported gold catalysts for CO oxidation. The high catalytic activity of Au-doped metal oxide

catalysts depends strongly on the pH value during precipitation between 8 and 9. For different supported materials used, the increasing catalytic activity of gold catalysts was obtained by optimization of the isoelectric point of the support lies between 6 and 9. Grunwaldt et al.[87] was presented the differences between these catalysts by gold colloids about 2 nm size on TiO_2 and ZrO_2 in aqueous solutions. Although the particle size on different supports was comparable, the Au/TiO_2 catalyst showed significantly higher activity than the Au/ZrO_2 catalyst corroborating that the support plays a key role in CO oxidation. Recently, Petit et al.[88] revealed that the TiO_2-ZrO_2 was better than TiO_2 or ZrO_2 of CO oxidation as a result of a relatively high BET surface area, high surface acidity, high thermal stability and great mechanical strength.

2-5.   Photocatalytic reduction of CO_2

According to the Intergovernmental Panel on Climate Change (IPCC) assessment report in 2001, the global average surface temperature has increased by about 0.6 °C over the 20 th century, and most of the warming observed over the past 50 years is attributable to human activities. Emissions of greenhouse gases (GHGs) such as CO_2, CH_4, N_2O, HFCs, PFCs, and SF_6 are the primary cause of global warming that continue to change in the climate system and atmospheric composition throughout the 21st century. The primary contributor of human activities is carbon dioxide (CO_2) emissions from fossil fuel combustion. Since the beginning of the age of industrialization, the atmospheric concentration of CO_2 was increased about 35%, it was approximately more than 130 times greater than the quantity emitted by volcanoes, amounting to about 27 billion tonnes per year. Currently, a great amount of technologies have been developed to reduce CO_2 by three approaches: (1) efficient use of carbon-based energy sources, (2) use of alternative or carbon-free energy sources, and

(3) use of a post-treatment carbon-capture technology and storage of the captured CO_2[89]. The capture system refers to the removal of CO_2 from industrial flue gas by chemical or physical adsorption[90], cryogenic processes[91] and membrane separation process[92-93]. The captured CO_2 can be stored in deep ocean and aquifer, or injected into geological formations like depleted oil and gas wells for enhanced recovery of fossil fuel products. Furthermore, more attractive researches use CO_2 as a raw material for chemical method, photochemistry, reforming, electrochemical and biological transformation. However, the production of CO_2-free fuel by direct conversion into supply energy is still a challenge. Because CO_2 is a relatively inert and stable compound, the Gibbs free energy (ΔG) indicated that the equilibriums are highly unfavorable to the expected product (Table 2-5).

There are four main methodologies to transform CO_2 into useful chemicals: (1) use high energy starting materials such as hydrogen and organometallics (2) choose oxidized low energy synthetic targets such as organic carbonates (3) shift the equilibrium to the product side by removing a particular compound and (4) supply physical energy such as light or electricity[94]. Hence, the photocatalytic conversion of CO_2 into more useful compounds is one of the most promising method because use of solar energy is less energy-consuming than the conventional methods.

Table 2-5 Conversion of CO_2 with water into hydrocarbon.[95]

Reaction	$\Delta H°$ (kJ/mol)[a]	$\Delta G°$ (kJ/mol)[b]	n [c]	E (eV)[d]
$H_2O_{(l)} \rightarrow H_{2(g)} + \frac{1}{2}O_{2(g)}$	286.0	237	2	1.23
$CO_{2(g)} + 2\,H_2O_{(l)} \rightarrow HCOOH_{(l)} + \frac{1}{2}O_{2(g)}$	541.1	275	2	1.43
$CO_{2(g)} + H_2O_{(l)} \rightarrow HCHO_{(g)} + O_{2(g)}$	795.8	520	4	1.35
$CO_{2(g)} + 2\,H_2O_{(l)} \rightarrow CH_3OH_{(l)} + \frac{1}{2}O_{2(g)}$	727.1	703	6	1.21
$CO_{2(g)} + 2\,H_2O_{(l)} \rightarrow CH_{4(g)} + 2\,O_{2(g)}$	890.9	818	8	1.06
$CO_{2(g)} + H_2O_{(l)} \rightarrow \frac{1}{6}C_6H_{12}O_6 + O_{2(g)}$	467.3	480	4	1.25

[a] Enthalpy change at 298 K, calculated from enthalpy of formation ($\Delta H_f°$).
[b] Gibb's Free energy charge at 298 K.
[c] Numbers of electrons transferred.
[d] Potential energy stored per electron transferred.
[e] Photosynthetic reaction.
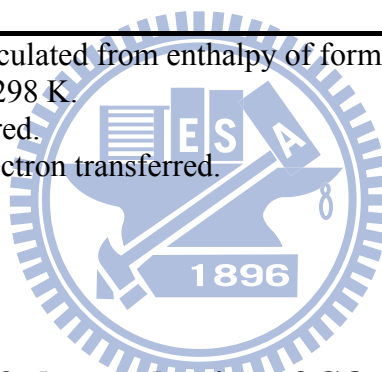
2-5-1. The mechanism of photoreduction of CO_2

The photocatalytic reduction of CO_2 by water or hydrogen as a reductant is convenient and efficient. Two important species involved in CO_2 photoreduction are hydrogen atom (·H) and carbon dioxide anion radical ($·CO_2^-$) produced by electron transfer from the conduction band as follows[94] [96]:

Photoexcited electrons (e^-) and positive holes (h^+):

$$TiO_2 \xrightarrow{\ hv\ } h_{vb}^+ + e_{cb}^-$$ (2-14)

Excited state of TiO₂:

$$\left(Ti^{4+} - O^{2-}\right) \xrightarrow{\quad hv \quad} \left(Ti^{3+} - O^{-}\right)^{*} \tag{2-15}$$

Hole (h⁺) react with water or hydrogen:

$$H_2 + 2\,h_{vb}^{+} \xrightarrow{\quad hv\left(Ti^{3+}-O^{-}\right)^{*} \quad} 2\,H^{+} \tag{2-16}$$

$$2\,H_2O + 4\,h_{vb}^{+} \xrightarrow{\quad hv\left(Ti^{3+}-O^{-}\right)^{*} \quad} 4\,H^{+} + O_2 \tag{2-17}$$
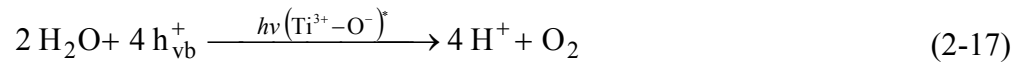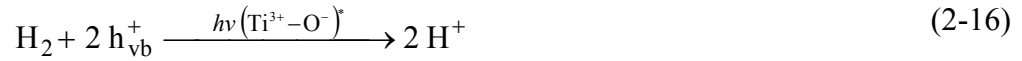
Hydrogen atom (•H) formation:

$$H^{+} + e_{cb}^{-} \xrightarrow{\quad hv\left(Ti^{3+}-O^{-}\right)^{*} \quad} \cdot H \tag{2-18}$$

Carbon dioxide anion radical (•CO₂⁻) formation:

$$CO_2 + e_{cb}^{-} \xrightarrow{\quad hv\left(Ti^{3+}-O^{-}\right)^{*} \quad} \cdot CO_2^{-} \tag{2-19}$$

It is expected that these radicals will form other stable substances:

Carbon monoxide (CO) formation:

$$\cdot CO_2^{-} + 2 \cdot H \xrightarrow{\quad \left(Ti^{3+}-O^{-}\right)^{*} \quad} CO + H_2O \tag{2-20}$$

$$2 \cdot CO_2^{-} + e^{-} \xrightarrow{\quad \left(Ti^{3+}-O^{-}\right)^{*} \quad} CO + CO_3^{2-} \tag{2-21}$$
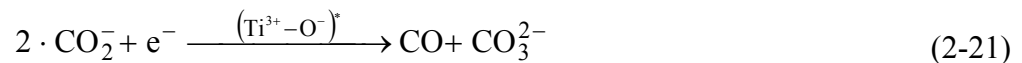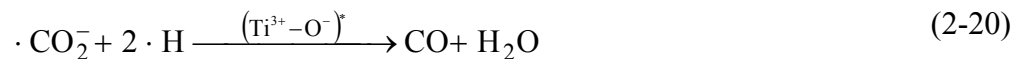
Formic acid (HCOOH) formation:

$$\cdot CO_2^{-} + \cdot H \xrightarrow{\quad \left(Ti^{3+}-O^{-}\right)^{*} \quad} HCOO^{-} \tag{2-22}$$

$$HCOO^{-} + H^{+} \xrightarrow{\quad \left(Ti^{3+}-O^{-}\right)^{*} \quad} HCOOH \tag{2-23}$$

Formaldehyde (HCOH) formation:

$$HCOO^- + \cdot H \xrightarrow{\left(Ti^{3+}-O^-\right)^*} HCO^- + H_2O$$

$$HCO^- + H^+ \xrightarrow{\left(Ti^{3+}-O^-\right)^*} HCOH$$

(2-24)

Methane (CH$_4$) formation:

$$\cdot CO_2^- + 7 \cdot H \xrightarrow{\left(Ti^{3+}-O^-\right)^*} \cdot CH_3 + 2\, H_2O$$

(2-26)

$$\cdot CH_3 + \cdot H \xrightarrow{\left(Ti^{3+}-O^-\right)^*} CH_4$$

(2-27)
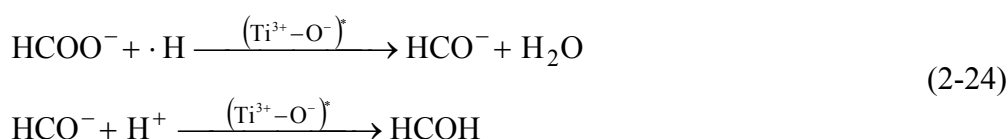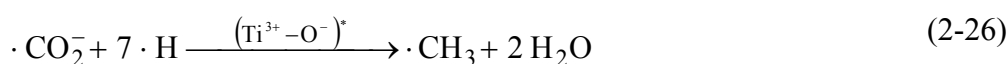
Methanol (CH$_3$OH) formation:

$$\cdot CH_3 + H_2O \xrightarrow{\left(Ti^{3+}-O^-\right)^*} \cdot CH_3O$$

(2-28)

$$\cdot CH_3O + \cdot H \xrightarrow{\left(Ti^{3+}-O^-\right)^*} CH_3OH$$

(2-27)

Ethylene (C$_2$H$_4$) or ethane (C$_2$H$_6$) formation:

$$\cdot CH_3 + \cdot CH_3 \xrightarrow{\left(Ti^{3+}-O^-\right)^*} C_2H_4 + H_2$$

(2-30)

$$\cdot CH_3 + \cdot CH_3 \xrightarrow{\left(Ti^{3+}-O^-\right)^*} C_2H_6$$

(2-31)

Although the pioneering works on the mechanisms of CO_2 photoreduction in aqueous phase were suggested by Inoue[97] and some researchers have attempted to fully understand, the reaction yield and selectivity of desired products is indefinably. Several examples have pointed out that the activity of photoreduction generally depends on the light radiation, pressure, temperature, reductant and CO_2/H_2O mole ratio. Kaneco *et al.*[98] demonstrated that the reaction rate varies with UV irradiation time. At low light intensities, the rate increases linearly with intensity; at intermediate light intensities, the rate is dependent on the square root of intensity; and at high intensities, the degradation rate is constant. Mizuno *et*

al.[99] reported an increase in pressure of CO_2 significantly accelerated the reduction in both water and the caustic solution. This result can be attributed that increasing pressure increases the availability of CO_2 adsorbed on the TiO_2 surfaces, so that the selectivity of photocatalytic reduction of CO_2 in water is accelerated. In addition, the reaction rate can be increased by raising the collision frequency and diffusion rate at high temperature. Anpo *et al.*[100] observed that the total yields of CH_4, CH_3OH, and CO are larger at 323 K than at 275 K under UV irradiation. It is clear that the photocatalytic reactions proceed more efficiently at higher temperatures. This research also shows the improvement of photocatalytic reactivity with an increase in the ratio of the H_2O to CO_2; however, an excess amount of H_2O suppresses the reaction rates. Yoneyama *et al.*[101] used various solvents including water, acetonitrile, 2-propanol, and dichloromethane for photoreduction of CO_2 and found that the CO decreased with the increase of the dielectric constant of the solvent. Such results are due to that the $\cdot CO_2^-$ can be greatly stabilized by high dielectric constant solvent, thus resulting in weak interactions with the photocatalytic surface. Tseng *et al.*[102] indicate that the methanol yield increases by adding NaOH. The caustic solution dissolves more CO_2, then OH^- in aqueous solution also serves as a strong hole scavenger to prevent the recombination of charge carriers.

2-5-2. The photocatalytic reduction of CO_2 over TiO_2

In 1979, Inoue *et al.*[97] have firstly reported that HCHO, HCOOH, CH_3OH and a trace amount of CH_4 are produced by the photoreduction of CO_2 with H_2O under xenon- and mercury-lamp irradiation of aqueous suspension systems containing a variety of semiconductor powders such as WO_3, TiO_2, ZnO, CdS, GaP, and SiC. In later years, many research groups have investigated the mechanism and efficiency of photocatalytic reduction

of CO_2 using variety of semiconductors. TiO_2 catalysts are considered as the most suitable candidates because of low cost and high stability. In particular, the wide band gap of TiO_2 provides sufficient negative and positive redox potentials in conduction bands (CB) and valence bands (VB), respectively, as shown in Figure 2-14. Halmann et al.[103] concluded the summarized photoreduction of CO_2 on TiO_2 in aqueous suspension systems. Because of the low solubility of CO_2 in water, the photoreduction was performed in a gas-solid interface. Since recent work in solid-gas systems were introduced by Anpo et al.[104], several researchers reported the photocatalytic reduction of CO_2 by TiO_2 with gaseous H_2O. Because the efficiency of CO_2 reduction was negligible when water vapor was used as the reductant, the enhancement of reaction rate, solar utilization and the selectivity of products become the most attractive issues in CO_2 photoreduction technology.

Loading TiO_2 with metals have been demonstrated to suppress recombination of charge carriers, thus increasing CO_2 conversion efficiency. Several researchers[102] used sol-gel method derived Cu/TiO_2 catalysts for photoreduction of CO_2 in aqueous phase and found the yield of methanol is much higher than those without Cu loading. They noted that the copper is an effective electron trapper with optimal loading. Yamashita et al.[105] reported that CH_4 was formed from the photoreduction of CO_2 with H_2O in the presence of TiO_2 and additional yield of CH_3OH was observed when Cu was incorporated into the TiO_2. Mul et al.[106] investigated the mechanism of photocatalytic conversion of CO_2 and H_2O on Cu/TiO_2 by means of in-situ DRIFT spectroscopy. Results show that the residual carbon which adsorbed on the catalyst surface is involved in photocatalytic CO_2 reduction. Ishitani et al.[107] reported that CO_2 photoreduction using Pd, Rh, Pt, Au, Cu, and Ru deposited on TiO_2 photocatalyst produces CH_4 and acetic acid, and the Pd/TiO_2 exhibited high selectivity for CH_4 production. Zhang et al.[108] used a gas-solid heterogeneous system for photoreduction of CO_2 with H_2O on Pt-loaded TiO_2 catalyst. The Pt-metal content could obviously improve

the photocatalytic activity toward CH_4 production, and Pt/TiO_2 nanotube was more active than Pt/TiO_2 nanoparticle catalyst. Other studies have investigated the synergistic effect of both metal loading and porous support to enhance photocatalytic reduction of CO_2. Sasirekha *et al.*[15] prepared the Ru-doped anatase TiO_2, which is supported on silica by a solid-state dispersion method, and tested its photoreduction behavior for CO_2 in aqueous phase. The TiO_2/SiO_2 catalysts exhibited higher photocatalytic activity than the powdered TiO_2 catalyst, but the $Ru-TiO_2/SiO_2$ has a detrimental effect due to the metal hinders the formation of Ti-O-Si bond. Recently, Li *et al.*[14] prepared mesoporous silica supported Cu/TiO_2 nanocomposites through a one-pot sol-gel method, and photoreductive experiments were carried out in a continuous-flow reactor using CO_2 and gaseous water as the reactants under the irradiation of xenon lamp. This significantly enhancement of photoreduction rate of CO_2 was attributed to the synergistic combination of Cu deposition and high surface area of SiO_2 support. A summary of the important literatures in photoreduction of CO_2 by TiO_2 between 1995 and 2010 is presented in Table 2-6.
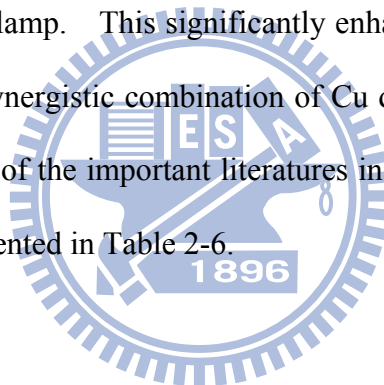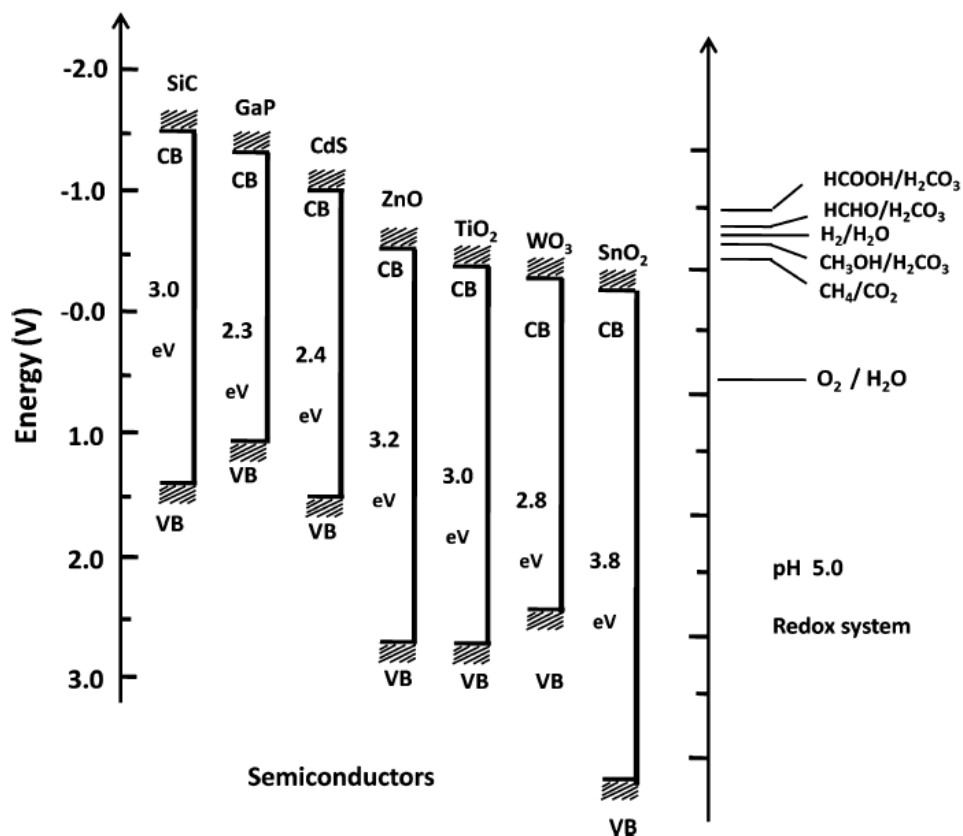
Figure 2-14 A schematic illustration of the energy correlation between semiconductor photocatalysts and redox couples in water.[1]

Table 2-6 Summary of the CO_2 photoreduction on TiO_2.

Photocatalyst	Reductant	Light source	Product	Ref
TiO_2	Water	75W high pressure Hg lamp, $\lambda > 280$ nm	CO, CH_4 and CH_3OH	[100]
TiO_2	Liquid CO_2	990 W Xe lamp	HCOOH	[109]
TiO_2	0.2 M NaOH solution	4.5 kW Xe lamp	CH4 and HCOOH	[99]
TiO_2	1 M 2-propanol solution	4.2 kW Xe lamp Methane	CH_4	[110]
TiO_2/zeolite	Water	75W high pressure Hg lamp, $\lambda > 280$ nm	CH_4 and CH_3OH	[13]
TiO_2/zeolite	Water vapor	High pressure Hg lamp, $\lambda > 280$ nm	CH_4 and CH_3OH	[111]
TiO_2/SiO_2	1 M 2-propanol solution	500 W high-pressure Hg arc lamp	Formate and CO	[101]
Rh/TiO_2	H_2	Hg lamp, $\lambda > 280$ nm, 370 nm, 450 nm	CO and CH_4	[112]
TiO_2, Cu/TiO_2	0.2 N NaOH solution	8 W Hg lamp, $\lambda = 254$ nm	O_2 and CH_3OH	[102]
Cu/TiO_2	0.2 N NaOH solution	8 W Hg lamp, $\lambda = 254, 365$ nm	CH_3OH	[113]
Cu-Fe/TiO_2	Water vapor	150 W high pressure Hg lamp	CH_4 and C_2H_4	[114]
N3-dye Cu-Fe/TiO_2	Water vapor	Solar light	CH_4 and C_2H_4	[115]
TiO_2/SiO_2, Ru-TiO_2/SiO_2	H_2	1000 W high-pressure Hg lamp, $\lambda = 365$ nm	CH_4, HCHO and HCOOH,	[15]
Pt/TiO_2	Water vapor	300W high pressure Hg lamp, $\lambda = 365$ nm	CH_4	[108]
Cu/TiO_2-SiO_2	Water vapor	Xe lamp	CH_4	[14]
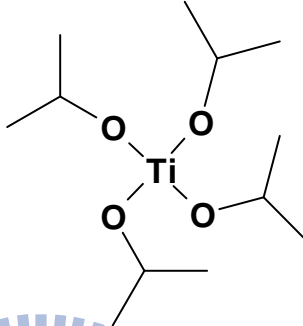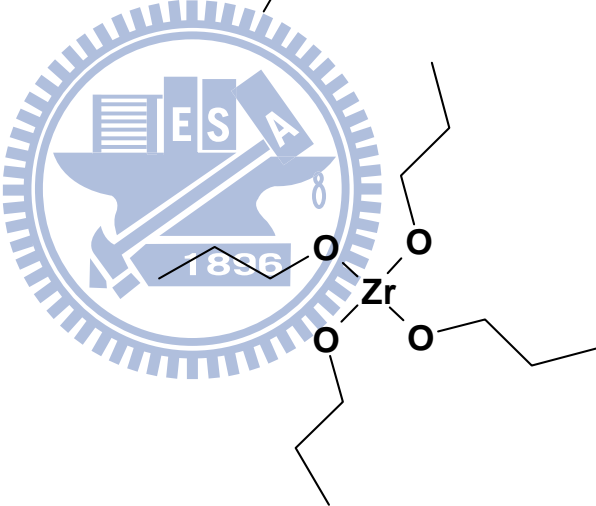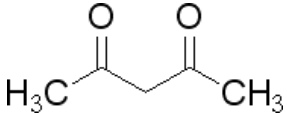
Chapter 3.   Materials and methods

Figure 3-1 shows the flowchart of the experimental design in this study.   Catalysts are synthesized through the evaporation induced self-assembly (EISA) process.   Their microstructures and physiochemical properties are characterized by means of TEM, TGA, UV-vis, XRD, XPS, XAS and N_2 adsorption isothermal.   The adsorption and photoreduction experiments are employed to evaluate their photocatalytic activity, and EPR is carried out to clarify the mechanism of the photocatalytic reduction of CO_2 with H_2O.

3-1.   Materials

Poly(ethylene   glycol)-*block*-poly(propylene   glycol)-*block*-poly(ethylene   glycol) (Pluronic P123, $EO_{20}PO_{70}EO_{20}$, M = 5800, Sigma-Aldrich) was used as the structure directing agent.   Titanium isopropoxide (TTIP, $Ti(OC_3H_7)_4$, Acros, 98.0 %), Zirconium (IV) tetra-propoxide (ZTP, $Zr(OCH_2CH_2CH_3)_3$, Acros, 70.0 %) and hydrogen tetrachloroaurate (III) trihydrate ($HAuCl_4 \cdot 3H_2O$, Aldrich, 99.9 %) were used as the precursor of titanium, zirconium and gold, respectively.   Absolute ethanol (CH_3CH_2OH, Sigma-Aldrich) was used as the solvent to dissolve the precursors.   Acetylacetone (Acac, $CH_3COCH_2COCH_3$, Fluka, 99.5 %) was used as the chelating agent to control the hydrolysis and condensation of the TiO_2 and ZrO_2.   Hydrochloric acid (HCl, J. T. Baker, 36.5 %) and sodium hydroxide (NaOH, Riedel-de Haën, 99.0 %) were used to adjust the pH value of solution.   They were shown in Table 3-1.

Table 3-1 The structural formula of materials used in this study.

Chemical	Structural formula
Pluronic P123	x=20, y=70, z=20
Titanium isopropoxide	
Zirconium (IV) tetra-propoxide	
Hydrogen tetrachloroaurate (III) trihydrate	
Acetylacetone	

Figure 3-1 Flowchart of experimental design in this study.

3-2. Preparation of mesoporous Au-loaded and Zr-doped TiO$_2$ samples

Mesoporous Zr-doped TiO$_2$ samples were prepared via an evaporation induced self-assembly (EISA) process. The preparation procedure is shown in Figure 3-2. Pluronic P123 (4.56 g, 0.786 mmol) was firstly dissolved in absolute ethanol (46.8 mL). Then, hydrochloric acid (0.14 m) and deionized water (4.16) were slowly added into the above mixture with vigorous magnetic stirring for 30 min. At the same time, titanium isopropoxide (12 mL), zirconium (IV) tetra-propoxide (x-y mL) together with acetylacetone (4.06 mL) were mixed in a brown glass vial form a reddish yellow complex solution. The complex was added to the surfactant solution to undergo hydrolysis under vigorous stirring for 1 hr. Subsequently, the gel was aged at ambient condition without any perturbation. After approximately 2 days, yellow translucent glasslike xerogel was obtained upon solvent evaporation. The xerogel was heated about at 100 °C for 24 hr (ramp of 0.5 °C min^{-1}) to improve the condensation of the inorganic network, and the surfactant was removed through calcination at 400 °C (ramp of 0.5 °C min^{-1}) for 4 hr in air. The mesoporous TiO$_2$ is called TiO$_2$, and the Zr-doped TiO$_2$ samples with various doping amount are named as Zr$_x$TiO$_2$, where x = 0.01, 0.02, 0.03, 0.04, 0.05 and 0.10. The introduction of gold nanoparticles on the mesoporous TiO$_2$ support was achieved via a deposition-precipitation (DP) method, which the procedure is as shown in Figure 3-3. A HAuCl$_4$ aqueous solution (4.0 × 10^{-3} M) was added to deionized water (20 mL) with vigorous stirring. The pH value was adjusted to 8.0 by dropwise addition of NaOH (1 M), and then 0.5 g of mesoporous TiO$_2$ was dispersed in the mixture. The resulting solution was heated at 80 °C with continuously stirring for 1 h and the precipitates were separated by centrifugation. As-synthesized samples were dried and finally calcined at 300 °C for 2 hr in air. Based upon synthesis stoichiometry, the Au-loaded TiO$_2$ catalysts are called x% Au-TiO$_2$ where the x resents 0.1, 0.5, 1, 2, 4 and 8 wt % Au-loading.
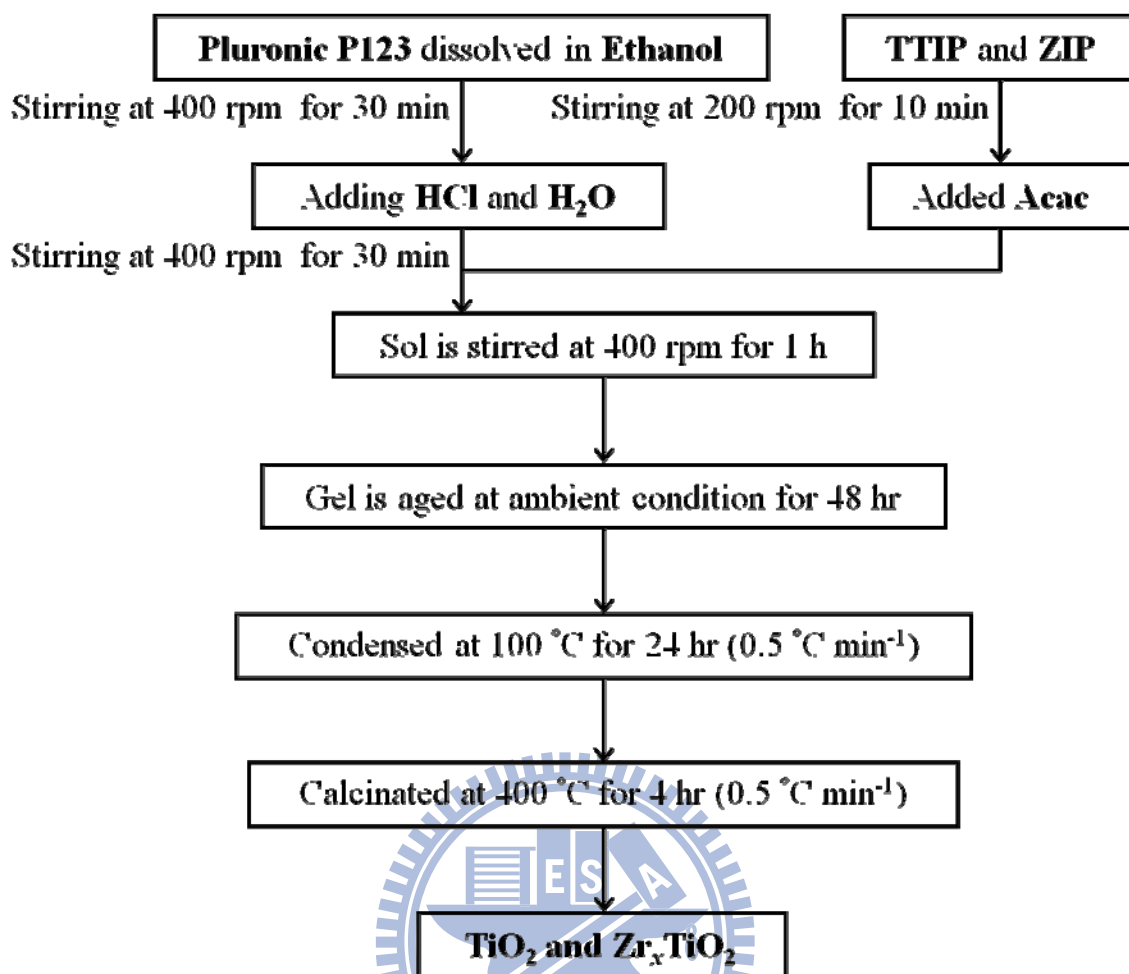
Figure 3-2 Synthetic process of mesoporous TiO_2 and Zr_xTiO_2 samples via an EISA method.

Table 3-2 Preparation mesoporous of TiO_2 and Zr_xTiO_2 samples and corresponding names.

Sample name	TTIP	ZIP	P123	Acac	HCl	H_2O	EtOH
TiO_2	1	0	0.02	1	0.04	6	20
$Zr_{0.01}TiO_2$	1	0.01	0.02	1.01	0.04	6	20
$Zr_{0.02}TiO_2$	1	0.02	0.02	1.02	0.04	6	20
$Zr_{0.03}TiO_2$	1	0.03	0.02	1.03	0.04	6	20
$Zr_{0.04}TiO_2$	1	0.04	0.02	1.04	0.04	6	20
$Zr_{0.05}TiO_2$	1	0.05	0.02	1.05	0.04	6	20
$Zr_{0.1}TiO_2$	1	0.1	0.02	1.1	0.04	6	20
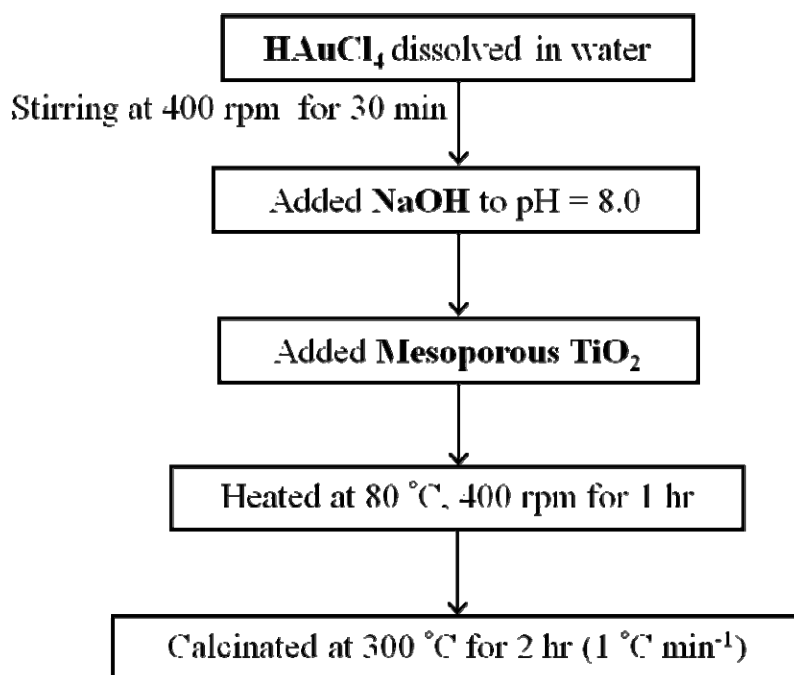
Figure 3-3 Synthetic process of Au-doped mesoporous TiO_2 catalyst via a DP method

Table 3-3 Preparation conditions of Au-loaded TiO_2 samples and corresponding names.

Sample name	TTIP	Au[a]	P123	Acac	HCl	H_2O	EtOH
0.1% Au-TiO_2	1	0.1	0.02	1	0.04	6	20
0.5% Au-TiO_2	1	0.5	0.02	1	0.04	6	20
1.0% Au-TiO_2	1	1.0	0.02	1	0.04	6	20
2.0% Au-TiO_2	1	2.0	0.02	1	0.04	6	20
4.0% Au-TiO_2	1	4.0	0.02	1	0.04	6	20
8.0 % Au-TiO_2	1	8.0	0.02	1	0.04	6	20
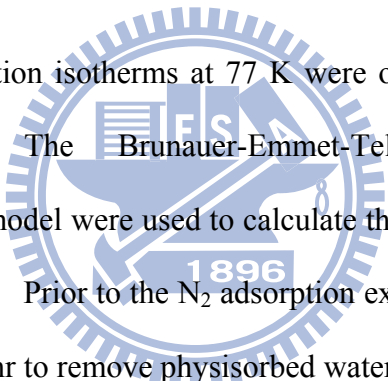
[a] represent weight percent

3-3.   Characterization

3-3-1.   High Resolution Transmission Electron Microscopy (HTEM)

The inner structure of the catalyst was analyzed using a high resolution transmission electron microscopy (HRTEM, Philips TECNAI 20) working at a 200 keV accelerating voltage.   The powders were dispersed into acetone with ultrasonication for 30 min, and then the suspension was dropped on a copper grid placed into the specimen stage.

3-3-2.   Nitrogen adsorption and desorption isothermal

N_2 adsorption and desorption isotherms at 77 K were obtained using a Micromeritics, TriStar 3000 instrument.   The Brunauer-Emmet-Teller (BET) equation and Barret-Joyner-Halenda (BJH) model were used to calculate the specific surface area and pore size distributions, respectively.   Prior to the N_2 adsorption experiment, over 0.2 g of catalyst was degassed at 120 °C for 12 hr to remove physisorbed water.

3-3-3.   X-ray Powder Diffractometry (XRPD)

X-ray diffraction (XRD) patterns of the catalysts were recorded with a X-ray powder diffractometer (XRPD, MAC Sience, MXP18) using Cu Kα radiation (λ = 0.1546 nm) in the range of 20° to 70° (2θ) with a sampling width of 0.02° and scanning speed of X° min^{-1}. The operating conditions of instrument were at an accelerating voltage of 30 kV and an emission current of 20 mA.   The crystalline size (D) of all samples was calculated via a Scherrier's equation:

$$D = \frac{K \times \lambda}{\beta \times \cos\theta} \tag{3-1}$$

D: Crystalline size

K: Scherrier constant (0.89)

λ: Wavelength of X-ray source (Cu Kα radiation, λ = 0.1546 nm)

β: Full width at half maximum (FWHM)

θ: Scatting angle

3-3-4. Electron Paramagnetic resonance (EPR)

The electron paramagnetic resonance spectrometer (EPR, Bruker EMX-10/12) was used to examine the photo-induced charge carriers at X-band frequency.   The measurements were carried at 77 K in darkness and UV irradiation.   A 250 W Hg lamp (Moritex ,MUV-250U-L) exhibiting a major output wavelength at 365 nm was positioned at a fixed distance from sample cavity.   The conditions of the instrument were set at a center field of 3500 G and sweep width of 2000 G.   The microwave frequency was 9.49 GHz and the power was 1.0 mW.

3-3-5. Thermo Gravimetric Analysis and Differential Scanning Calorimetry (TGA/DSC)

The measurements of organic content and thermal transition of the samples were carried out thermo gravimetric analysis (TGA, TA 5100) and differential scanning calorimetry (DSC, Netzsch 404).   The samples were heated from temperature to 900 °C with a heating ramp of

5 °C min^{-1} under an air flow at 60 mL min^{-1}.

3-3-6.   X-ray Photoelectron Spectroscopy (XPS)

The surface chemical compositions and speciation on the catalysts were examined by X-ray Photoelectron Spectroscopy (XPS, ESCA PHI 1600) using an Al Kα radiation (1486.6 eV).   The photoelectron was collected into the analyzer with pass energy of 23.5 eV.   The collection step size in wide range scan (survey) and high resolution analysis (multiplex) were 1.0 and 0.1 eV, respectively.   All analytic process was controlled under ultrahigh vacuum at the pressure below 1.0×10^{-8} Torr.   The binding energies were referenced to the Ti 2p peak at 458.8 eV of the catalyst framework.   For the qualification and quantification of each element, curve fitting of XPS spectra was performed on program with appropriate parameters including the binding energy, doublet separation and full-width at half maximum.   The atomic ratio was calculated from the integrated peak area which was normalized by sensitive factors.   The equation for atomic ration calculation is shown below:

$$\frac{n_1}{n_2} = \frac{I_1 / ASF_1}{I_2 / ASF_2} = \frac{A_1 / ASF_1}{A_2 / ASF_2} \tag{3-2}$$

n_x: atomic number

I_x: intensity of species on XPS spectra

ASF_x: atomic sensitive factor of element

A_x: peak area of XPS spectra

3-3-7.　UV-vis Spectrometer

A diffuse reflectance UV-vis spectrophotometer (Hitachi, U-3010) was used to characterize the electronic structure of the catalysts.　The UV-vis spectra were acquired from 900 to 200 nm with a scanning rate of 150 nm min^{-1}.　All the analysis used aluminum oxide (Al_2O_3) as the reference which was considered a total reflection material.　The band gap of catalysts was determined from the absorption edges converted from the reflectance spectra using a Kubelka-Munk equation:

$$F(R) = \frac{(1-R)^2}{2R} = \frac{k}{S} \tag{3-3}$$

k: absorption coefficient

S: scatting coefficient

R: %R reflectance

3-3-8.　X-ray Absorption Spectroscopy (XAS)

The X-ray absorption spectroscopy (XAS) uses synchrotron radiation to investigate the structural and electronic properties of the X-ray absorbing atom and about its local environment.　The Ti K-edge and Zr-edge X-ray absorption spectroscopy (XAS) spectra were recorded in transmission mode for synthesized powders mounted on a Scotch tape at beamline 01C1 and 16A1 with a double-crystal Si (111) monochromator for energy scanning, respectively..

3-3-9.　CO$_2$ Adsorption Test

CO$_2$ adsorption-desorption isotherm was performed at 273 K using an adsorption apparatus (Micromeritics, TriStar 3000).　Over 0.2 g catalyst was loaded into an adsorption tube and degassed with pure N$_2$ gas at 120 °C for 12 hr.　The saturated adsorption amount and the adsorption constant were calculated using the Langmuir equation:

$$\frac{P/P_0}{\theta} = \frac{1}{X_m K} + \frac{1}{X_m} \times \frac{P}{P_0} \qquad (3\text{-}4)$$

P: gas pressure at 273K

P_0: saturated vapor pressure at 273K

θ: adsorbed amount on surface

X_m: saturated adsorbed amount on surface

K: Langmuir equilibrium constant

3-3-10.　CO$_2$ Photoreduction Test

Before the photocatalytic reaction, the catalyst was heated at 120 °C for 1 hr and irradiated with UV light (305 nm, 30 W) in O$_2$ for 12 hr to purify the surface.　A batch reactor and a gaseous system were designed for the photocatalytic reduction of CO$_2$ (as shown in Figure 3-4 and 3-5).　First, a 0.05 g sample was dispersed on the glass fiber filter paper (ADVANTEC GC-50), and then the filter paper was placed on the stainless holder in the middle of reactor.　The CO$_2$ (99.99%) stream with different vapor content was obtained via mixing one CO$_2$ stream with another one, which passed through a water bubbler

to be fully humidified (Humidity > 95 %), at different volume ratios.   The reactant gas was then introduced to the cylindrical Pyrex glass reactor with a quartz window at the top. The cylindrical reactor has 55 mm in height and 85 mm in outside diameter, and the total volume is 220 ml.   A stainless steel holder was placed into the reactor to support the glass fiber membrane loaded with the catalyst.   To fulfill the reactor with the humidified CO_2, the gas stream purged the reactor at a rate of 50 mL/min for 1 hr.   The photocatalytic reduction of CO_2 was carried out in a stainless box surrounded with 16 UV lamp (305 nm, 8 W for each lamp) for 8 hr.   The gas (0.2 mL) was sampled using a side-port gaseous tight needle at various intervals, and the concentrations of CO_2 and intermediates were measured by using a gas-chromatography (GC) equipped with a capillary column (30 m $\times$ 0.53 mm, Supel-Q^{TM} Plot), a thermal couple detector (TCD) and a flame ionization detector (FID).   The yield of product at any given time in the reaction was determined by means of a calibration curve.   A CH_4 standard gas was prepared for the calibration curve.   A 10 μL of CH_4 gas was injected into the reactor fully filled with N_2.   Then, 20, 50 100, 200, 300, 400 and 500 μL of the mixture were analyzed by GC and calculated the injected CH_4 amounts.   The quantification of CH_4 was performed by a FID based upon the apparent intensity of 2.41 min for CH_4 compound, allowing the simultaneous analysis of N_2 and CO_2 by a TCD (see Appendix A).

Quantum efficiency (Φ_E) is an essential parameter to determine the photoreduction activity that can be evaluated with Equation 3-5.   First, the total moles of photons were calculated from the period of photon flux by the Equation 3-6.   The absorbed photon flux was detected by photometer of 120 mW/cm^2 as shown in Figure 3-6.   and the surface area received UV irradiation was 8.04 cm^2.   And the each photon energy at 305 nm wavelength is 6.5 $\times$ 10^{-19} J.   The eight moles of electrons are required to produce 1 mol of methane from CO_2.   All methane yields of samples were compared by the initial and total quantum efficiency at 1 hr and 8 hr of UV illumination, respectively.

$$\text{Quantum efficiency}\,(\Phi_E)\,\% = \frac{8\ \text{moles of methane yield}}{\text{moles of photon absorbed by catalyst}} \times 100 \qquad (3\text{-}5)$$

$$\text{Moles of Absorbed photon by catalyst} = \frac{\text{photon flux} \times \text{irradiated area} \times \text{time}}{\text{each photon energy} \times 6.02 \times 10^{23}} \qquad (3\text{-}6)$$

Flow controller

UV lamp

Batch reactor

CO$_2$

Water Bubbler

GC
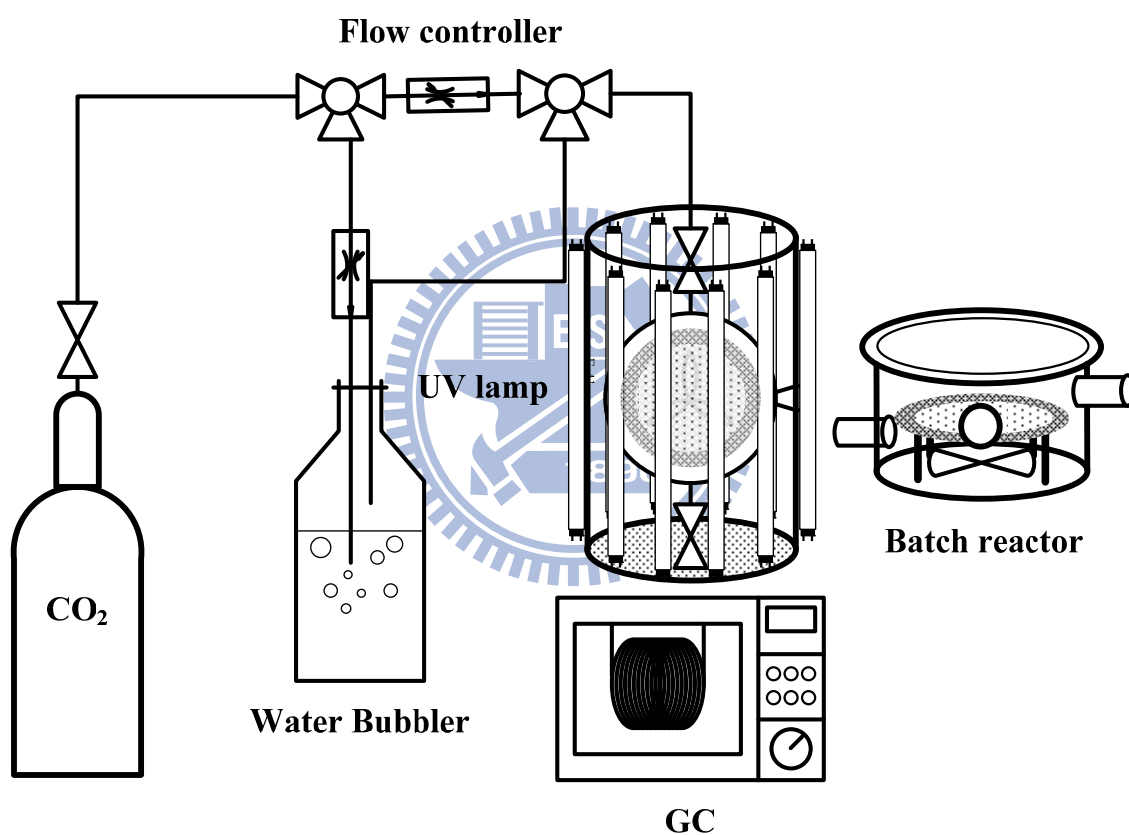
Figure 3-4 Schematic illustration of the experimental setup for photoreduction of CO$_2$.
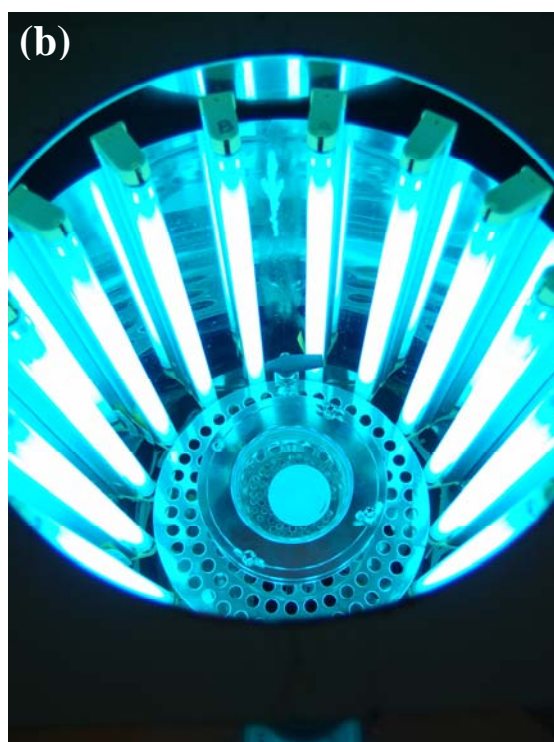
Figure 3-5 Photographs of the (a) photocatalytic reactor and (b) illuminated system.
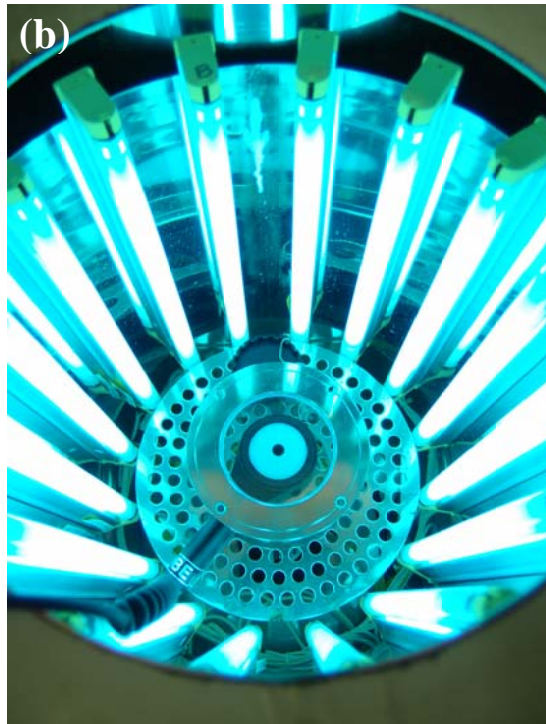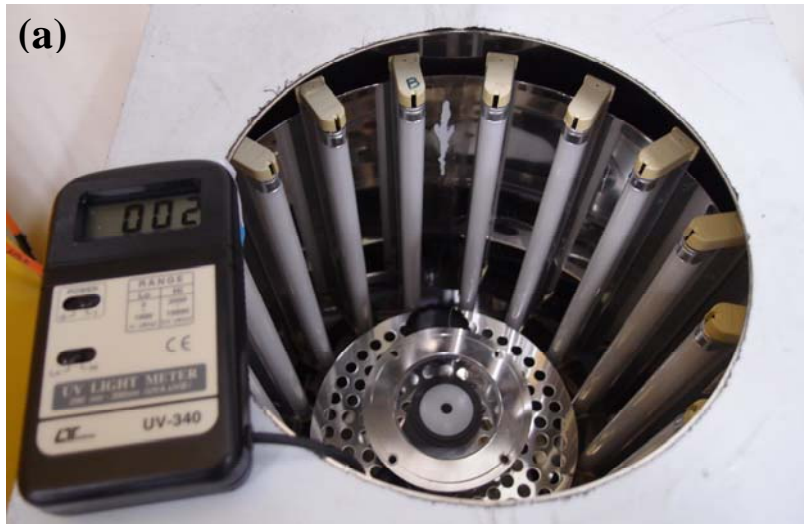
Figure 3-6 Photographs of the (a) photometer and (b) illuminated photometer system.

Chapter 4.   Results and Discussion

4-1.   Thermal analysis

To understand the thermal properties of synthesized samples, the weight loss and heat flows of samples were examined in terms of the thermogravimetric analysis (TGA) curves and differential scanning calorimetry (DSC) measurements.   Figure 4-1 shows the DSC and TA/DTG profile of the as-prepared TiO_2 sample under air flow.   Below 200 °C, 10 wt % mass loss is due to removal of volatile species such as water, ethanol or hydrochloric acid. Two exothermic stages at 200-300 °C and 300-425 °C, which causes remarkable 40 and 10 wt % mass losses, respectively, indicate the partial decomposition and severe oxidation of P123.   The surfactant was completely burned out to result in mesoporous TiO_2 powders above 425 °C.
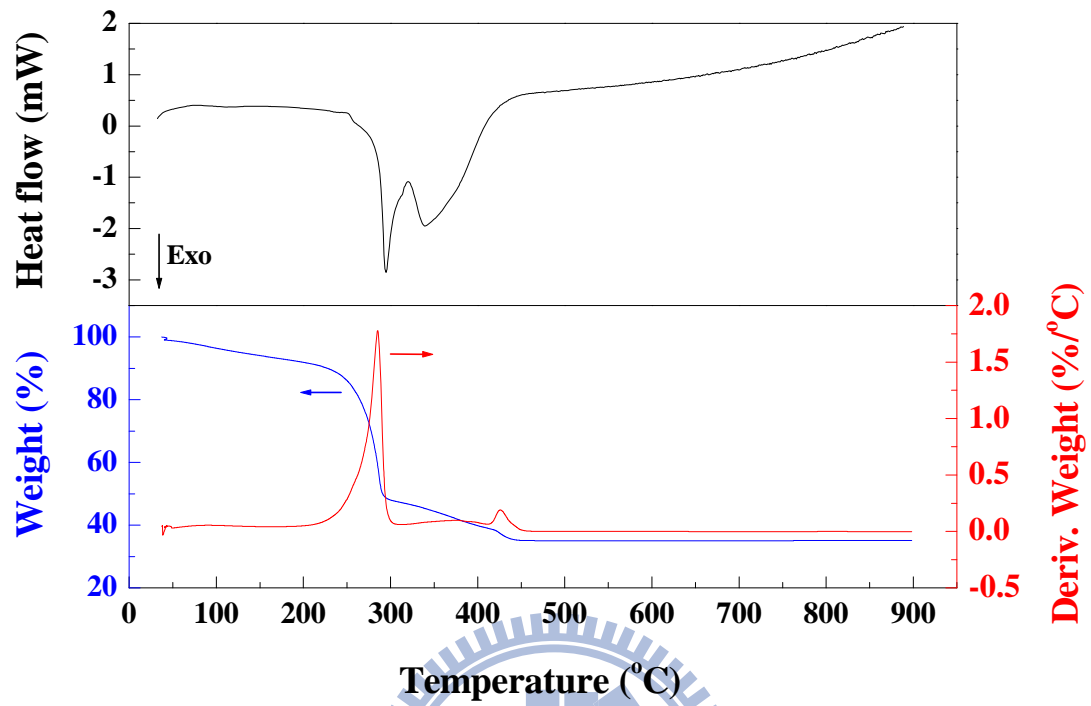
Figure 4-1 The DSC and TG/DTG curves of the as-prepared TiO$_2$ sample heated in air.

4-2.   Chemical composition

The chemical compositions and chemical states at the surface sites and in the bulk lattice of catalysts were characterized using XPS and ICP-MS.   Figure 4-2 shows the wide range scanned XPS spectra and high resolution scanned spectra of the mesoporous TiO_2, Zr_xTiO_2 and Au-TiO_2 samples.   In addition to Ti (2p) and O (1s) photoelectron lines, Zr(3d) and Au (4f) peaks were found the wide range scanned spectra, indicating the presence the incorporated elements on the TiO_2 surface (See Appendix B).   The Ti^{4+} ions, Zr^{4+} ions, and Au elements were indentified from the doublet peaks of Ti ($2p_{3/2}$), Ti ($2p_{1/2}$), Zr ($3d_{5/2}$), Zr ($3d_{3/2}$), Au ($4f_{7/2}$) and Au ($4f_{5/2}$) centered at 458.2, 464.0, 181.8, 184.5, 83.8, and 87.4 eV, respectively[88].   The surface Zr/Ti ratios were calculated from their integrated peak areas normalized with corresponding sensitive factors.   Table 4-1 lists the surface and total Zr/Ti atomic ratios.   It is noted that the surface Zr/Ti ratios were slightly larger than the bulk values when the total Zr/Ti ratio was lower than 0.08, indicating that most Zr^{4+} ions were doped at the TiO_2 surface lattice instead of homogeneously dispersed in the bulk.   The inhomogeneous distribution of Zr^{4+} ions was more significant at its low concentrations. Such phenomenon is attributed to the faster gelation of TiO_2 than that of ZrO_2 in the presence acetyl acetone which effectively chelates to Ti^{4+} and Zr^{4+} ions to slow the hydrolysis down. Compared to 6-coordinated Ti^{4+} ions, Zr^{4+} ions, which contain 7 or 8 coordinations, are more strongly bonded with acetyl acetone to have relatively slower hydrolysis and gelation rates. Thus, TiO_2 colloids are formed followed by co-precipitation of Zr-doped TiO_2 at the surface. Similar result was found in the non-hydrolytic sol-gel-derived Zr-doped TiO_2 samples when tri-octylphosphine oxide was used as the chelating agent[116].   The inhomogeneous distribution was inhibited when the concentration of the precursor of ZrO_2 increased in the sol solution because of its increased formation rate.   The surface-to-bulk Zr/Ti ratio of the doped TiO_2 was only 1.0 when the total Zr/Ti ratio was 0.1.   Table 4-2 lists the added and

total Au/Ti atomic ratios for the Au-load materials.   The total Au/Ti ratios ranged between 0.001 and 0.008 which were similar to the added ratios at low concentrations (ranged between 0.1% and 1.0%).   However, the total Au/Ti ratios ranging 2.0% to 8.0% were smaller than the added ratios by 2-5 times.   These results indicate that almost Au nanoparticles were successfully loaded on TiO_2 in the DP process at low concentrations. Over amounts of Au ions led to significant loss from deposition because of limited loading capacity of the TiO_2 samples.

Figure 4-3 displays the high resolution scanned O (1s) XP spectra of the TiO_2 and Zr_xTiO_2 samples.   The O (1s) spectra can be deconvoluted into M-O and M-OH species (M = Ti or Zr) with the binding energies centered at 530.1 and 531.7 eV, respectively.   Table 4-1 lists the M-OH/M-O ratios of pure TiO_2 and Zr_xTiO_2 samples.   The pure TiO_2 contained at the surface M-OH/M-O ratio of 0.22.   The M-OH/M-O ratio increased from 0.28 to 0.69 when the surface Zr/Ti ratios increased from 0.02 to 0.14.   This result reveals that incorporation of Zr^{4+} ions enhances surface hydrophicility of TiO_2 because of their higher coordination numbers than those of Ti^{4+} ions.   Similar results were observed in the mesoporous TiO_2-ZrO_2 composites which exhibited superior hydrophilicity[66].
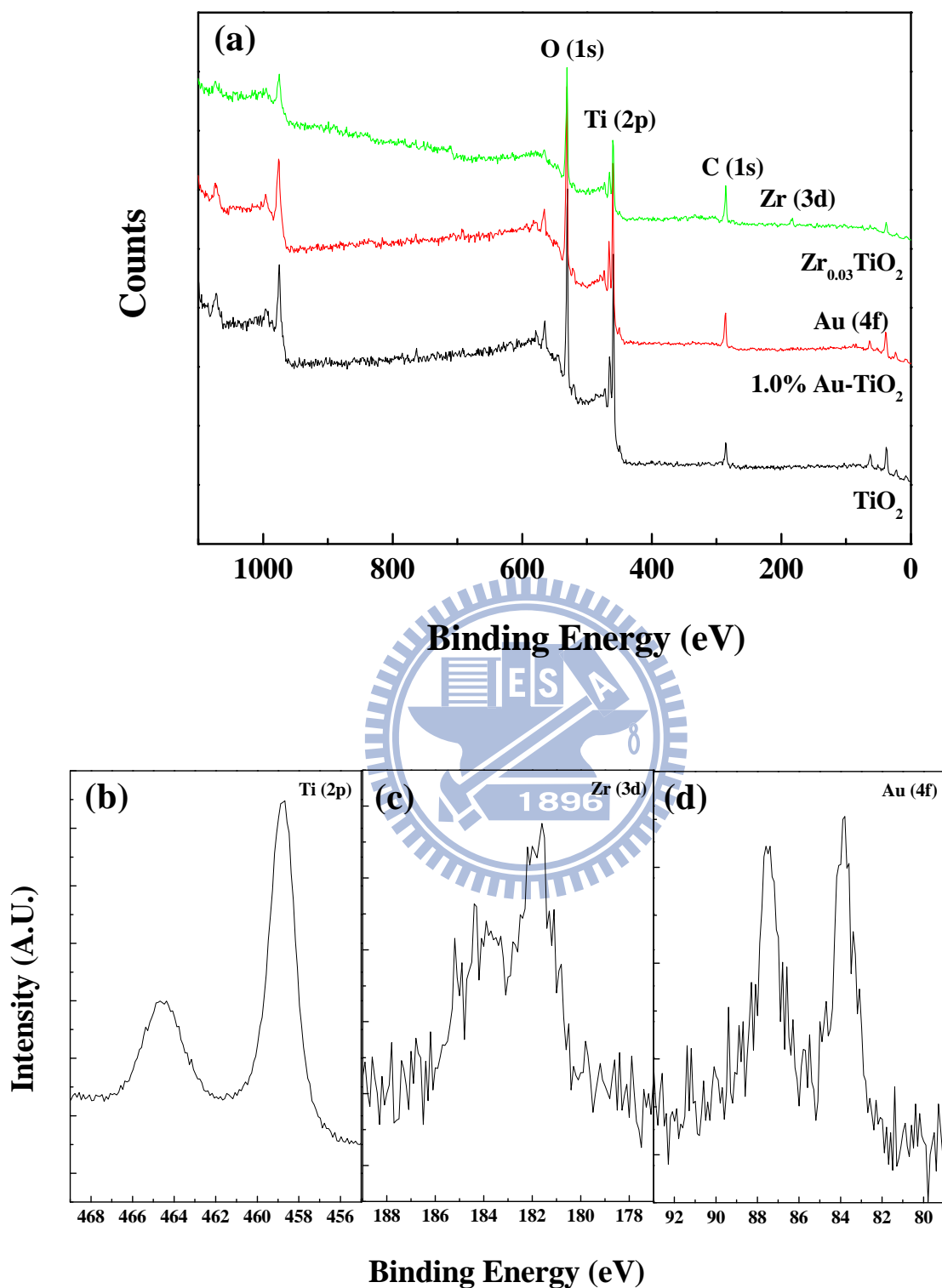
Figure 4-2 (a) The wide-ranged XP spectra and high resolution of (b) Ti (2p), (c) Zr (3d) and Au (4f) XP spectra of TiO_2, Zr_xTiO_2 and Au-TiO_2 samples.

Table 4-1 The surface chemical compositions of TiO_2 and Zr_xTiO_2 samples.

Sample	Surface Zr/Ti	Bulk Zr/Ti	Surface ratio/bulk ratio (A/B)	Ti-OH/Ti-O
TiO_2	-	-	-	0.21
$Zr_{0.01}TiO_2$	0.02	0.01	2.00	0.28
$Zr_{0.02}TiO_2$	0.07	0.04	1.75	0.30
$Zr_{0.03}TiO_2$	0.08	0.06	1.33	0.33
$Zr_{0.04}TiO_2$	0.11	0.08	1.37	0.37
$Zr_{0.05}TiO_2$	0.11	0.11	1.00	0.58
$Zr_{0.1}TiO_2$	0.14	0.14	1.00	0.69

- represents not available.

Table 4-2 The chemical compositions of Au-TiO_2 samples

Sample	Add Au/Ti	Total Au/Ti
0.1% Au-TiO_2	0.001	0.001
0.5% Au-TiO_2	0.005	0.005
1.0% Au-TiO_2	0.01	0.008
2.0% Au-TiO_2	0.02	0.010
4.0% Au-TiO_2	0.04	0.014
8.0% Au-TiO_2	0.08	0.016
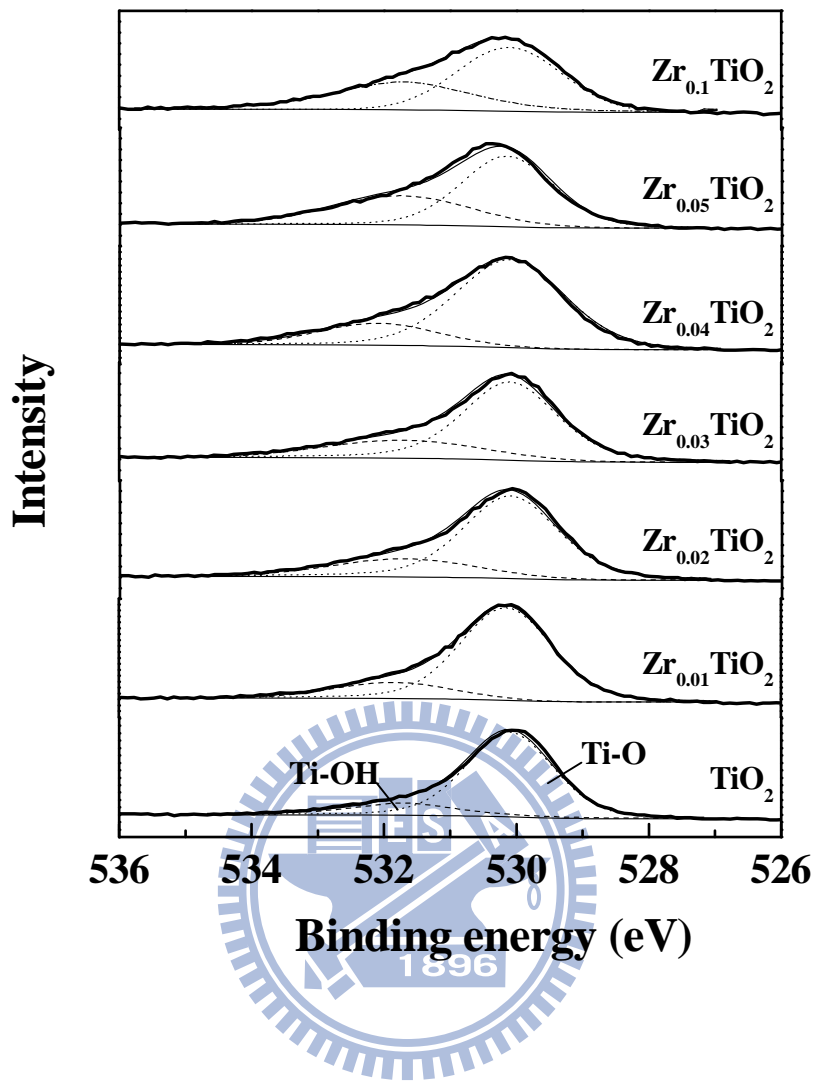
Figure 4-3 The O (1s) XP spectra of TiO$_2$ and Zr$_x$TiO$_2$ samples.

4-3.   Pore Structure

Figure 4-4 shows the N_2 adsorption and desorption isotherm and pore size distribution of P25 and mesoporous TiO_2.   The Degussa P25 exhibited type II adsorption an hysteresis loop of H3 type in the higher P/P_0 range, indicating the inter-particle porous features[117].   The TiO_2, prepared in this study, exhibited typical type IV adsorption isotherm with sharp capillary condensation steps between the relative pressures (P/P_0) of 0.4-0.8, implying the mesoporous structure with a narrow pore size distribution.   Its hysteresis loop was close to the H2 type, revealing the presence of ink-bottle shaped or cage-type pores in the given material[118].

Figure 4-5 displays the N_2 adsorption and desorption isotherm and pore size distribution of Zr-doped TiO_2 samples.   Incorporation of Zr^{4+} ions into the TiO_2 lattice changed the hysteresis loop from type H2 to H1 when the Zr/Ti ratio was ranged between 0.02 and 0.04, revealing uniform cylindrical geometry of mesoporous structure   In addition, the major pore size of the mesoporous TiO_2 samples shifted from 3.6 nm to 4.9 nm.   The presence of impurities at low concentrations assists the stability of the porous structure against thermal induced shrinkage and distortion.)   However, high concentrations of Zr^{4+} ions resulted in bi-modal mesoporous structures.   Two size distributions centered at 3.4 and 4.6 nm were obtained.   Zhou et al.[66] found the similar structure in their ZrO_2-TiO_2 mesoporous samples prepared using the P123 as the template through sol-gel process.   The bi-modal structure in this study is presumably due to reconstructive reaction field during the EISA process.   High concentrations of Zr^{4+} ions overall reduced the gelation rate.   The slow gelation enabled P123 self-assembling into small micelles to result in small pore size.   This effect is dominant because the pore size centered at 3.4 nm contained large portion.   When most solvent was evaporated from the system at the end of self-assembly, the concentrated sol

solution rapidly increased the gelation rate, thus leading to the large pore size of 4.6 nm. On the other hand, deposition of Au nanoparticles did not alter the porous structure of the TiO_2 samples. All Au-TiO_2 samples exhibited H2 type hysteresis loop, indicating that the Au nanoparticles were primarily deposit outside the pore channels (Figure 4-6).

Table 4-2 summarizes the BET specific surface areas, pore volumes and pore sizes of the catalysts. P25 contained a specific surface area of 48.3 m^2 g^{-1} and an aaverage inter-particle pore size of 30.0 nm. The presence of amphiphilic triblock copolymer in the EISA process led to the mesoporous structure of TiO_2 samples and contributed to the high surface area of 108 m^2/g. The Au-TiO_2 samples had surface areas of 102-110 m^2 g^{-1} and mean pore sizes of 8.2-11.4 nm, which are similar to those of pure TiO_2 sample. These results suggest that the Au nanoparticles obtained through deposition-precipitation method are well dispersed on the TiO_2 samples and do not block the pore channels. The Zr-doped TiO_2 samples possessed higher surface areas and larger pore volumes than the pure TiO_2 sample, except for the $Zr_{0.01}TiO_2$ sample which had similar texture (surface area: 121 m^2/g) as the pure TiO_2. The surface areas and pore volumes of the Zr_xTiO_2 catalysts with the x= 0.02-0.04 were 121-151 m^2 g^{-1} and 0.31-0.36 cm^3/g, respectively. The doped Zr^{4+} ions suppressed pore shrinkage during the thermal treatment to effectively preserve the high surface areas and large pore volumes. High Zr^{4+} ion loading (Zr/Ti= 0.05-1.00) dramatically increased the surface area of the mesoporous TiO_2 sample to 200-217 m^2 g^{-1}. Although the $Zr_{0.05}TiO_2$ and $Zr_{0.1}TiO_2$ samples exhibited reduced pore sizes (D_{mean}: 5.7-5.8 nm), they contained high pore volumes of 0.29-0.31 cm^3g^{-1}. This finding supports the reaction-filed determined textures.

TEM images in Figure 4-7 show that composites with Zr/Ti ratios from 0.01 to 0.1 and TiO_2 have typical 3-D wormhole-like mesostructure (See Appendix C). The replicated

mesoporous metal oxide exhibits a regular spherical morphology with a diameter ranging from about 7.5 to 1.5 nm. The particles are randomly oriented and the size of Zr_xTiO_2 samples was decreased with the Zr/Ti ratios increasing. The HRTEM micrograph indicates the presence of lattice fringes which demonstrates that the pore walls of the mesopores are composed of anatase nanocrystals (Figure 4.7 b and d). The pure mesoporous TiO_2 had well anatase crystalline with a d-spacing of (1 0 1) crystallographic plan of 0.83 nm. However, the $Zr_{0.03}TiO_2$ samples had a relativity smaller d-spacing of 0.42 nm consistent with the XRD results discussed later. The TEM and HRTEM images obtained for the Au-loaded TiO_2 are presented in Figure 4.7 e and f, respectively. The majority of mean diameter integrated upon crystallized TiO_2 were estimated between 10 and 20 nm and no significant change occurs of mesoporous structure during reaction.
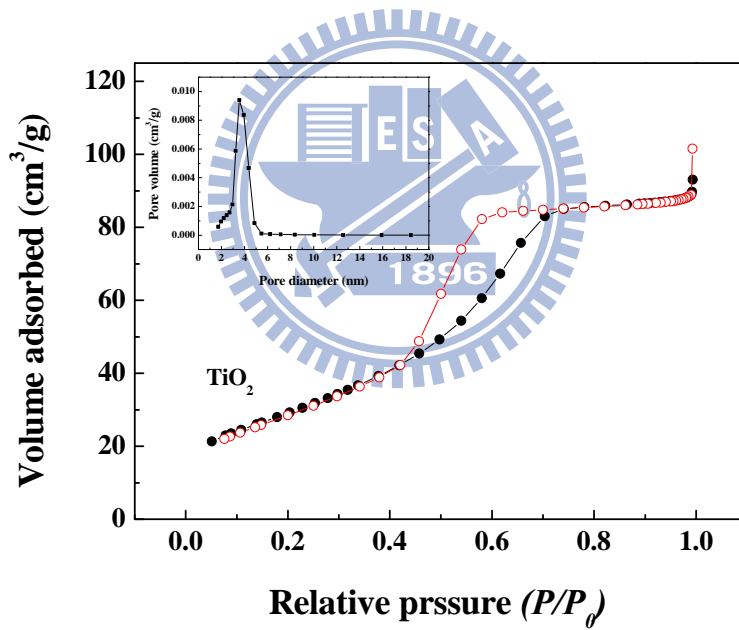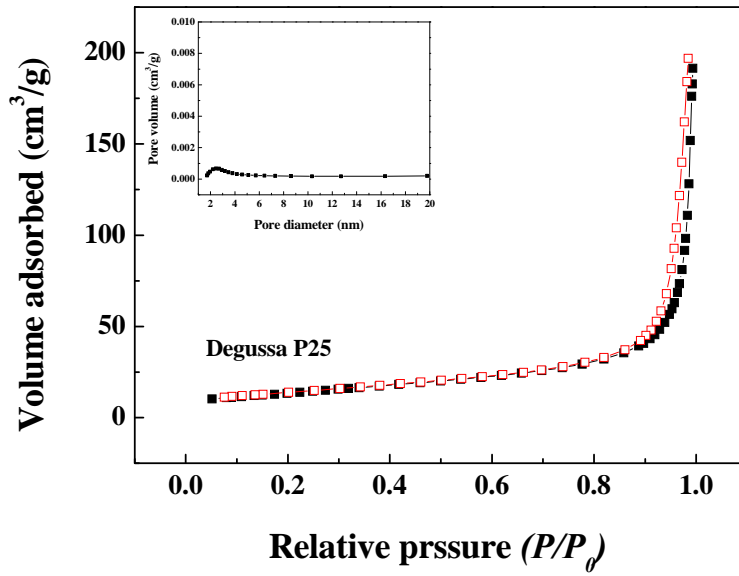
Figure 4-4 N$_2$ adsorption and desorption isotherm and BJH pore size distribution of pure TiO$_2$.
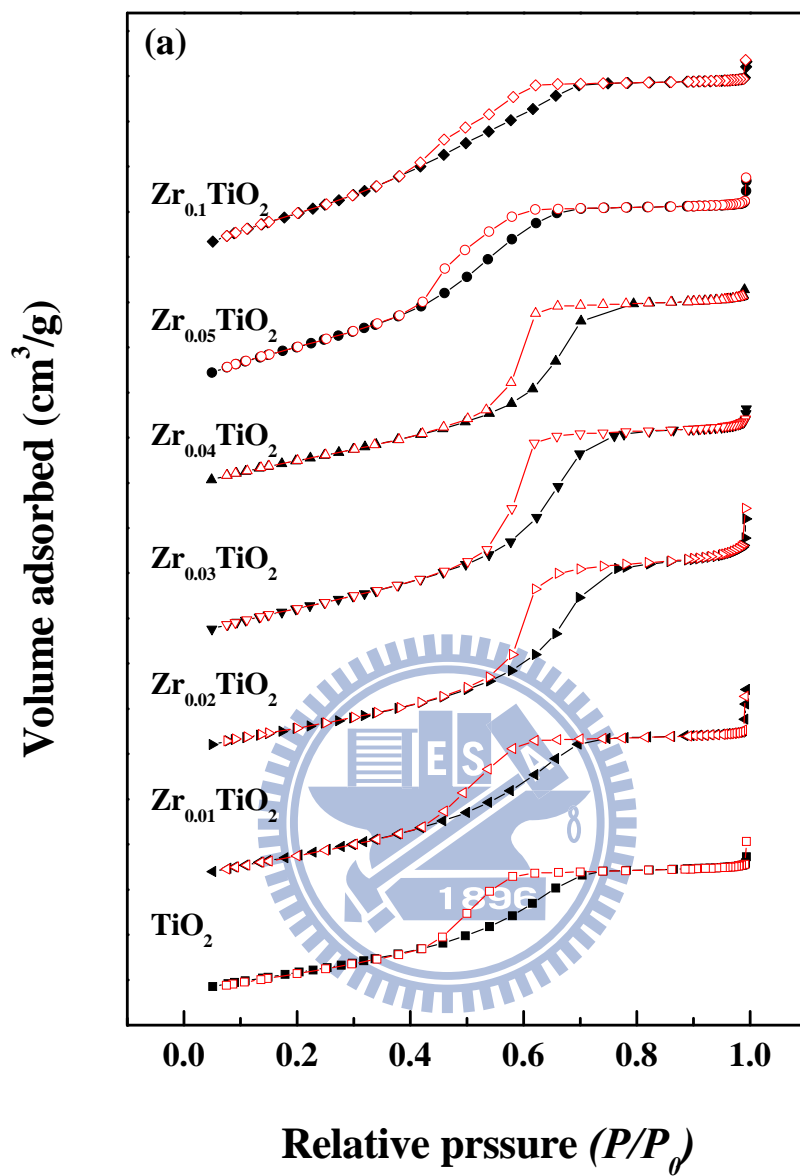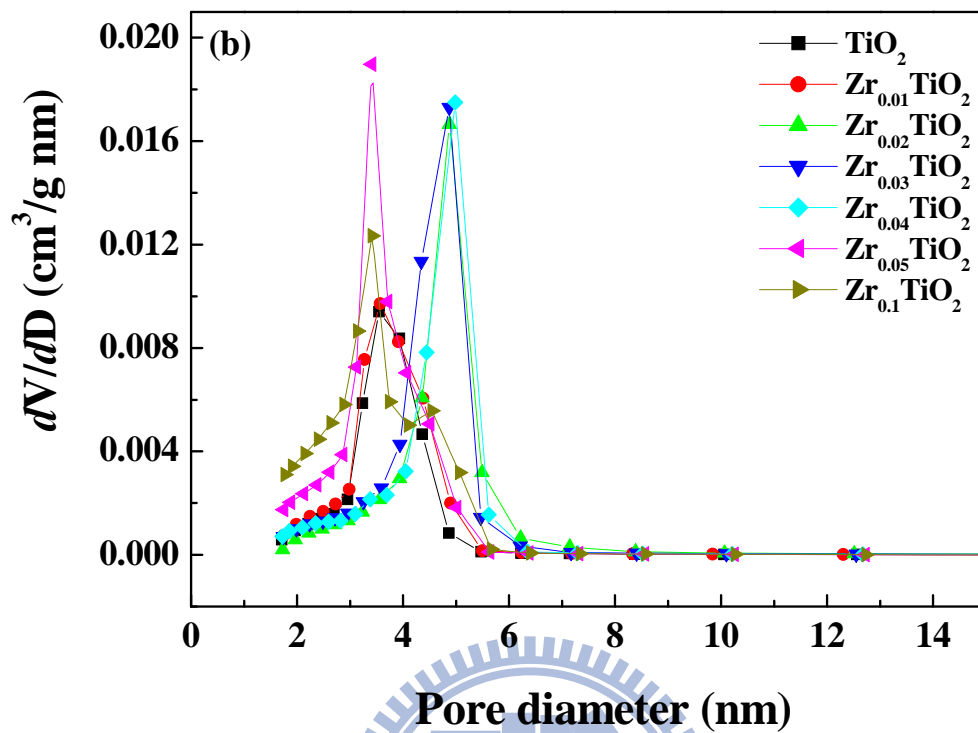
Figure 4-5 (a) N_2 adsorption and desorption isotherm and (b) pore size distribution of Zr_xTiO_2.
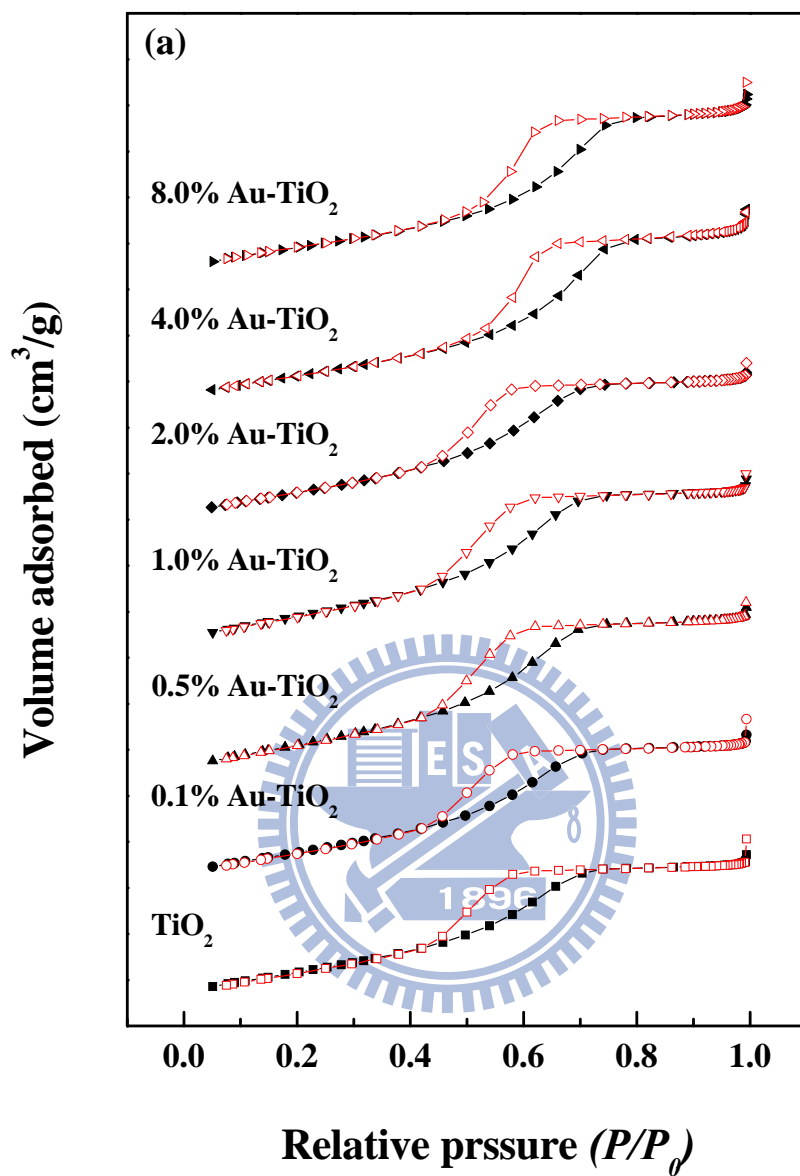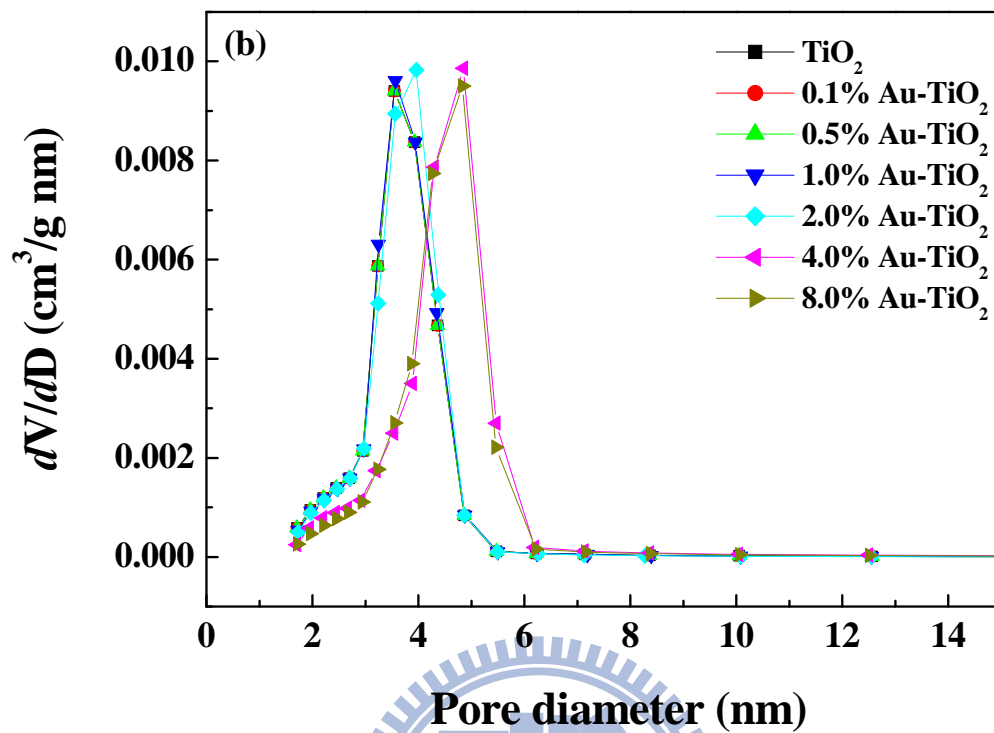
Figure 4-6 (a) N$_2$ adsorption and desorption isotherm and (b) pore size distribution of Au-TiO$_2$.

Table 4-3 Hysteresis loop types, Specific surface area (S_{BET}), pore volume (V_{pore}), mean pore size (D_{mean}) and major pore size (D_{major}) of catalysts.

Sample	Hysteresis loop	S_{BET} (m^2 g^{-1})	V_{pore} (cm^3 g^{-1})	D_{mean} (nm)	D_{major} (nm)
P25	H3 type	48	0.36	30.0	-
TiO$_2$	H2 type	108	0.26	9.7	3.55
Zr$_{0.01}$TiO$_2$	H2 type	121	0.24	9.9	3.6
Zr$_{0.02}$TiO$_2$	H1 type	126	0.31	14.6	4.9
Zr$_{0.03}$TiO$_2$	H1 type	150	0.32	8.4	4.9
Zr$_{0.04}$TiO$_2$	H1 type	151	0.36	9.6	5.0
Zr$_{0.05}$TiO$_2$	bimodal	200	0.29	5.8	3.4
Zr$_{0.1}$TiO$_2$	bimodal	217	0.31	5.7	3.4
0.1% Au-TiO$_2$	H2 type	108	0.26	10.9	3.6
0.5% Au-TiO$_2$	H2 type	110	0.29	10.8	3.6
1.0% Au-TiO$_2$	H2 type	108	0.24	9.1	3.6
2.0% Au-TiO$_2$	H2 type	108	0.22	8.2	4.0
4.0% Au-TiO$_2$	H2 type	104	0.29	11.4	4.8
8.0% Au-TiO$_2$	H2 type	102	0.24	9.5	4.8
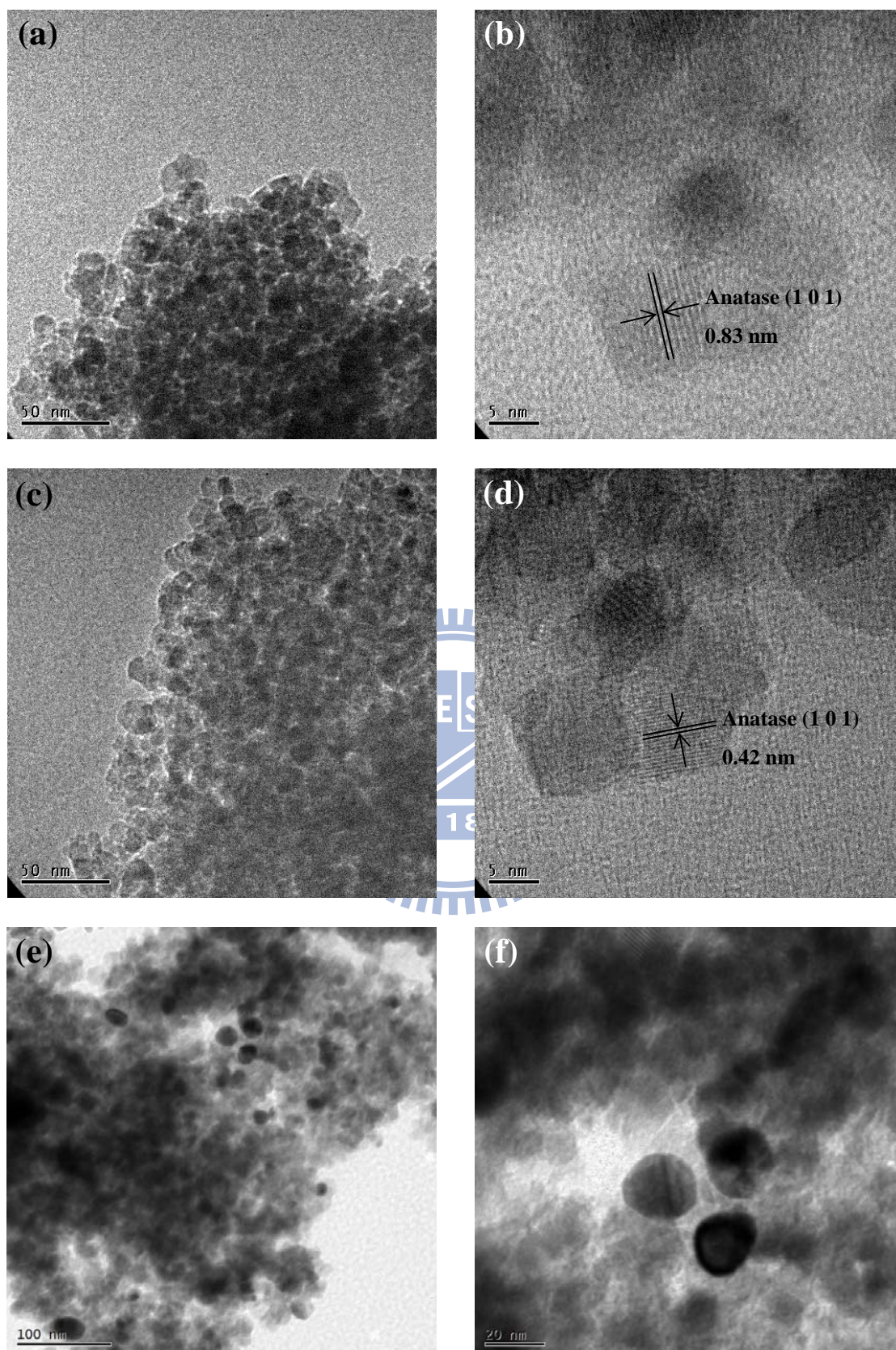
Figure 4-7 TEM images of (a) mesoporous TiO_2, (b) $Zr_{0.03}TiO_2$ and (c) 1.0% Au-TiO_2, and HRTEM images of (d) mesoporous TiO_2, (e) $Zr_{0.03}TiO_2$ and (f) 1.0% Au-TiO_2.

4-4.   Crystalline structure

X-ray diffraction (XRD) patterns of the TiO_2, Zr_xTiO_2 and $Au-TiO_2$ samples are shown in Figure 4-8.   The anatase TiO_2 was the only crystalline phase observed in the XRD patterns and no diffraction peaks of ZrO_2, $ZrTiO_4$ or gold were found.   The anatase (101) diffraction peak of the pure TiO_2 sample centered at 25.3° 2θ position.   Loading Au nanoparticles and incorporation of few amounts of Zr^{4+} ions (total Zr/Ti=0.01) have little influence on the position of the diffraction peak.   However, the $Zr_{0.02}TiO_2$ and $Zr_{0.03}TiO_2$ samples up-shifted the peak to 25.5-25.7° 2θ position, indicating the reduced d-spacing. This phenomenon was different from the literature results[62, 64, 116] which the partial substitution of Ti^{4+} ions species by Zr^{4+} ions expanded the cell volume owning to the larger ionic radius of Zr^{4+} ion (0.72 Å) than that of Ti^{4+} ion (0.65 Å).   The compression of anatase (1 0 1) profile in this study reveals that the Zr^{4+} ions are introduced between crystal domains not substituted for the Ti^{4+} ions in the TiO_2 lattice.   In addition, the thermal induced shrinkage of the amorphous Zr-doped TiO_2 moiety in the grain boundaries might compress the TiO_2 anatase crystals.   The anatase (1 0 1) diffraction peak returned to 25.3° when the concentration of the Zr^{4+} ions increased to 4 %.   It is presumably due to that excess Zr^{4+} ions are segregated from the amorphous doped TiO_2 moiety to reduce it volume and release the stress of anatase crystals during thermal treatment.   However, the ZrO_2 crystals are too tiny to be detected.   Poor crystallinity of $Zr_{0.05}TiO_2$ and $Zr_{0.1}TiO_2$ samples were observed.   The heavy doping of Zr^{4+} ions retards the crystallization of TiO_2.

The average crystallite sizes of the TiO_2 , Zr_xTiO_2 and $Au-TiO_2$ samples are calculated according to the Scherrer formula from the broadening of diffraction peaks of the anatase (1 0 1) of TiO_2 and the results are listed in Table 4-3.   The TiO_2 and $Au-TiO_2$ samples have similar crystallite sizes of 9.5-9.6 nm.   The Zr^{4+} ions at the Zr/Ti ratio of 0.01 slightly

decreased the crystallite size to 8.7 nm because of defect induced lattice strain.)   When the Zr/Ti ratios increased to 0.02-0.04, reduced gelation rate increased the crystallite size to 10.3-11.6 nm.   High loading of Zr^{4+} ions suppressed the TiO_2 crystallization and resulted in small crystallite sizes of 4.5 nm.

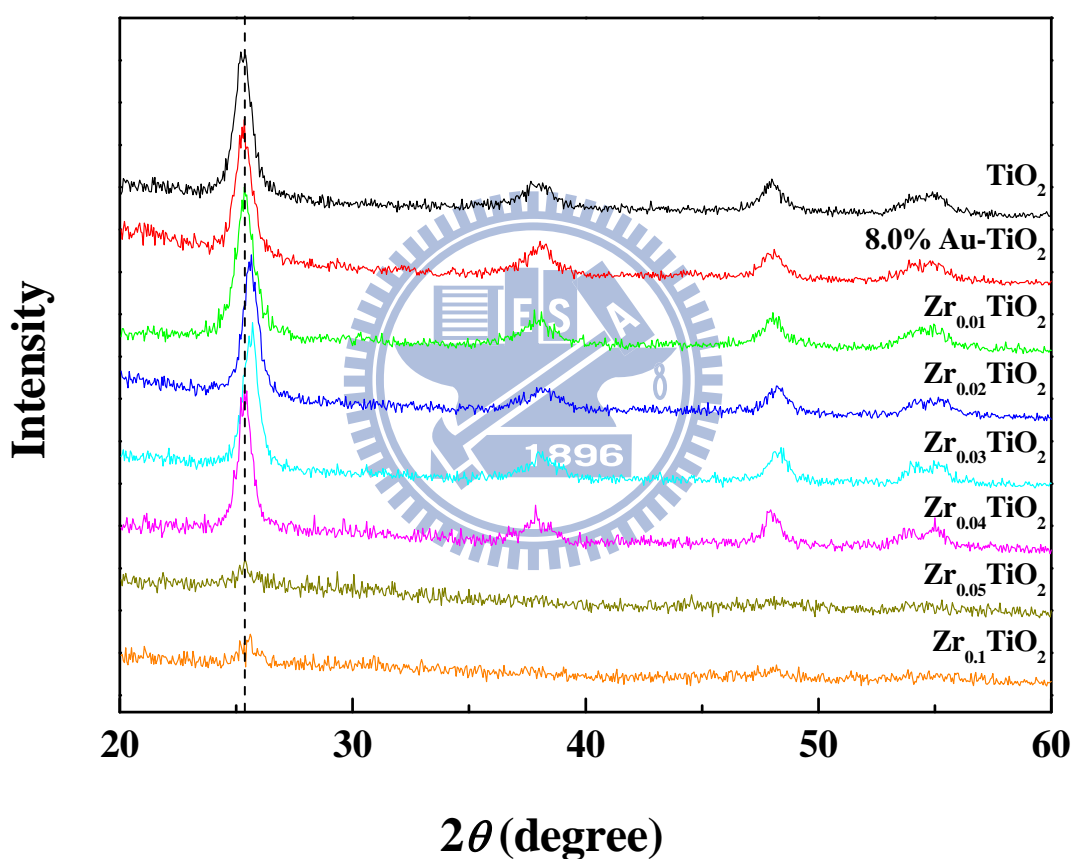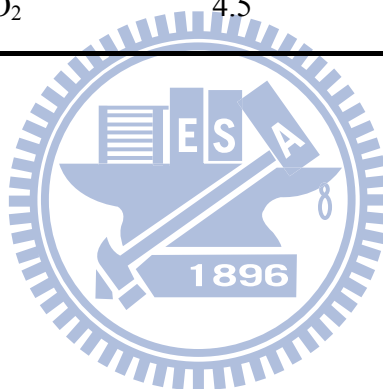Figure 4-8 XRD patterns of mesoporous TiO_2 and Zr_xTiO_2 samples.

Table 4-4 Crystallite sizes of mesoporous TiO_2 and Zr_xTiO_2 samples.

Sample	Crystalline size (nm)
TiO_2	9.6
8.0% Au-TiO_2	9.5
$Zr_{0.01}TiO_2$	8.7
$Zr_{0.02}TiO_2$	10.5
$Zr_{0.03}TiO_2$	10.3
$Zr_{0.04}TiO_2$	11.6
$Zr_{0.05}TiO_2$	6.8
$Zr_{0.1}TiO_2$	4.5

4-5.   Local geometric structure

The X-ray absorption spectroscopy (XAS) using synchrotron radiation is a powerful technique to investigate the local structural details and electronic properties of the X-ray absorbing atoms and about its local environment.   In this research, the XANES technique offers a detailed and quantitative picture of the local structure around Ti atoms.   Figure 4-9 (a) shows the XANES of Ti K-edge X-ray absorption spectra of TiO_2, Zr_xTiO_2 samples and the reference compound: anatase TiO_2.   Anatase structure of the mesoporous sample was confirmed from their similar absorption features to those of the reference sample.   As shown in Figure 4-9 b, the pre-edge structure at the Ti K-edge for anatase TiO_2 features four peaks labeled as A_1, A_2, A_3, and B, corresponding to transitions of the inner electron to Ti 3d, 4p, and 4s hybridized states.   The origin of A_1 peak was assigned to an exciton band or a transition from $1s \rightarrow 1t_{1g}$, while the origins of A_2 and A_3 are designated to $1s \rightarrow 2t_{2g}$ and $1s \rightarrow 3e_g$ transitions in an octahedral field, respectively.   The feature B is attributed to a Ti 4p character hybridized with the Ti 4s and O 2p orbitals.   Luca *et al.*[119] reported that the A2 feature is associated with poorly crystalline surface region and lattice distortion, respectively. In addition, the relative intensity of A_2 and A_3 absorptions increase with decreasing crystallite sizes of anatase crystals.   In this study, we found that the A2 intensity increased with the Zr^{4+} ion-loading.   We attribute this phenomenon to the increased surface areas.   The post-edge beyond the D transitions become poorly resolved as the Zr^{4+}-content increased because of reduced crystallite sizes.

The EXAFS spectra of anatase crystalline, TiO_2 and Zr_xTiO_2 samples are shown in Figure 4-10 a.   Large surface portion of the doped TiO_2 at high Zr-ion loading reduced the oscillation amplitude.   In addition, the presence of impurities which resulted in high degree of structural disorder could diminish the fine features.   The magnitude Fourier transforms

(FT) EXAFS of selected samples is shown in Figure 4-10 b.   These FT-EXAFS spectra show the existence of two shells of backscattering atoms around the central Ti element.   The first and second shells in these Fourier transforms are from single scattering paths, Ti-O and Ti-Ti bonds, respectively.   The bond distance of Ti to the first-shell O atom and second shell Ti atom was similar.   But the reduction in amplitude of the FT peaks with increasing Zr/Ti ratios, indicating the nearest Ti-O bonds and nearest neighbor Ti-Ti bonds experience an increase in mean square relative displacement (MSRD) with decreasing crystallinity.   For $Zr_{0.1}TiO_2$ sample, the absence of Ti-Ti bonds also represents the poor crystallization of TiO_2, which is in agreement with its XRD result.

Structure parameters are obtained from the fitting of the FT-EXAFS spectra.   The peaks of FT-EXAFS contain many contributions from both single and multiple scattering paths and they were fitted with a single set of distances (R) and Debye-Waller factors (σ^2) and then float the energy zero (e_0) to calculate the coordination numbers (N).   Figure 4-11 (a) shows the Ti K-edge FT-EXAFS of the pure metal oxides. The best fit parameters of coordination numbers and interatomic distances of the first and second shells around the Ti element in the mesoporous TiO_2 sample are listed in Table 4-4.   The Ti element had Ti-O and Ti-Ti coordinations with coordination number of 2.0 and 1.2 and bond length of 1.94 and 3.03 Å, respectively.   These coordination numbers are far less than the theoretical values (6 for Ti-O and 8 for Ti-Ti coordination) because of large portion of surface TiO_2 species.   The Zr K-edge XAS spectra of mesoporous ZrO_2 and Zr_xTiO_2 samples were also acquired (See Appendix D).   Figure 4-11 (b) shows the Zr K-edge FT-EXAFS of the mesoporous ZrO_2 and Zr_xTiO_2 samples.   The mesoporos ZrO_2 sample exhibits a tetragonal phase.   Table 4-5 lists the fitting parameters for the Zr elements.   The coordination number of Zr-O and Zr-Zr bond for the mesoporous ZrO_2 were 2.7 and 4.4, and the corresponding bond length was 2.04 and 3.41 Å, respectively.   Similar to the mesoporous TiO_2 sample, the low coordination

number of the Zr element in the mesoporous ZrO_2 sample is resulted from it high surface area. It is noted that the Zr-O coordination in the $Zr_{0.01}TiO_2$ sample was 6.8. In addition, Zr-Ti coordinations were obtained. These features reveal the incorporation of Zr^{4+} ions within the TiO_2 framework. The Zr-Zr coordination was additionally found when the Zr/Ti ratio was larger than 0.03. The low Zr-O coordination number (2.0) in the $Zr_{0.03}TiO_2$ indicates that the Zr ions were mainly doped within the TiO_2 surface lattice. The result supports the microstructure of the sample deduced from its XRD pattern. When the Zr/Ti ratio increased from 0.03 to 0.05, the Zr-Ti and Zr-Zr coordination number increased from 1.0 to 2.3 and decreased from 2.2 to 1.2, respectively, indicating the high concentration of Zr^{4+} ions drives some of them being doped into the inside TiO_2 lattice. Incorporation of the Zr^{4+} ions inside the TiO_2 framework becomes more significant as its loading further increases. In the $Zr_{0.1}TiO_2$ sample, Zr-O coordination increased to 3.4. In addition, the absence the Zr-Ti coordination and the increased Zr-Zr coordination number (6) also reveal the formation of ZrO_2 tiny clusters from their segregation. Such segregation allows TiO_2 anatase crystals turning from the compression state back to their normal structures.
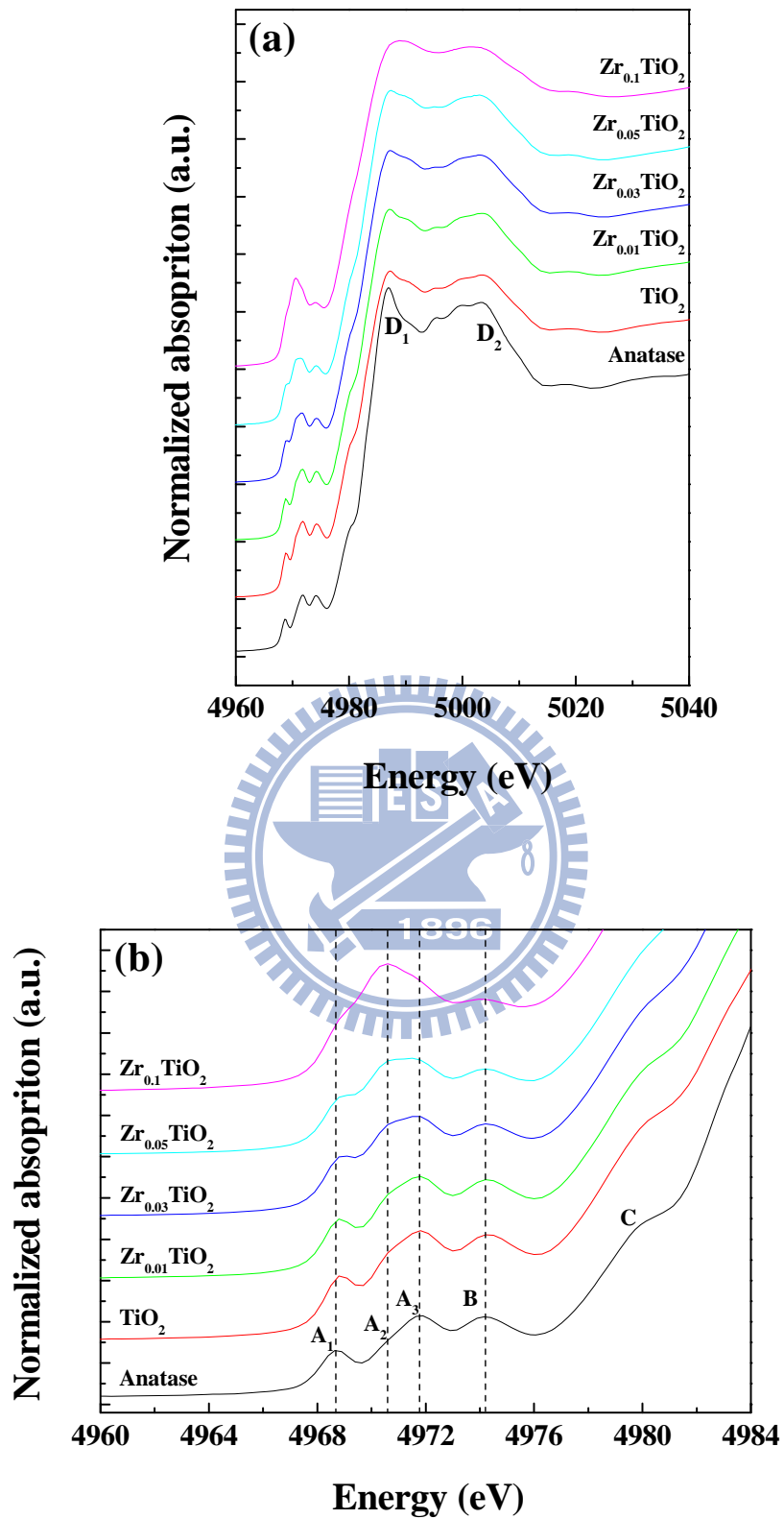
Figure 4-9 (a) Complete Ti K-edge XANES spectra (b) and pre-edge region of crystalline anatase TiO_2, mesoporous TiO_2 and Zr_xTiO_2 samples.
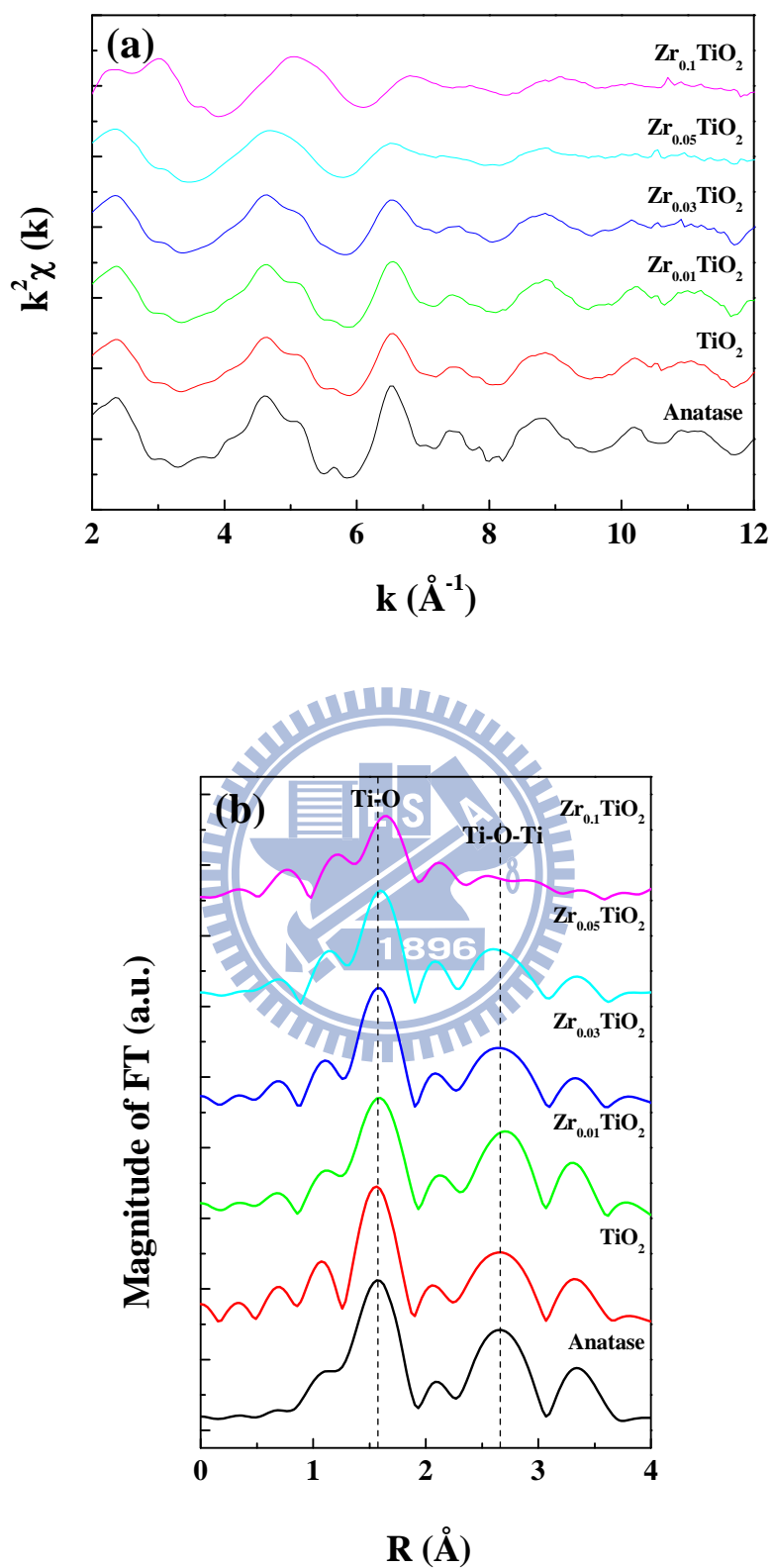
Figure 4-10 (a) Ti K-edge EXAFS spectra and corresponding (b) FT-EXAFS spectra of anatase TiO_2, mesoporous TiO_2 and Zr_xTiO_2 samples.
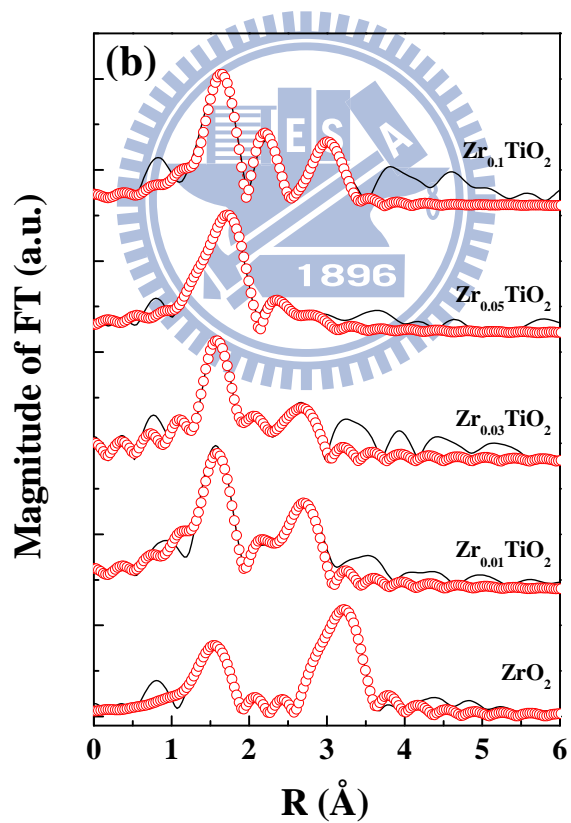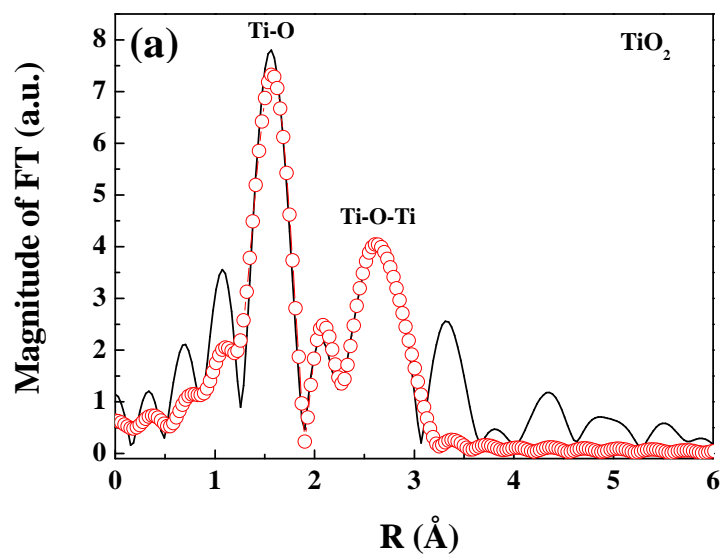
Figure 4-11 Fitted FT-EXAFS spectra of (a) mesoporous TiO_2, and (b) mesoporous ZrO_2 and Zr_xTiO_2 samples. Solid and symbolic lines represent the experimental and fitting curves, respectively.

Table 4-5 EXAFS fitting results at Ti K-edge of mesoporous TiO_2 samples.

Sample	Shell	N	R (Å)	σ^2 (Å^2)	R factor
Anatase (ref)	Ti-O	4	1.93	-[a]	
	Ti-O	2	1.98	-	
	Ti-Ti	4	3.04	-	-
	Ti-Ti	4	3.78	-	
TiO_2	Ti-O	2.0	1.94	0.0010	
	Ti-Ti	1.2	3.03	0.0020	0.0035

[a] References data.

Table 4-6 EXAFS fitting results at Zr K-edge of mesoporous ZrO_2 and Zr_xTiO_2 samples.

Sample	Shell	N	R (Å)	σ^2 (Å^2)	R factor
Tetragonal (ref)	Zr-O	4	2.10	-[a]	
	Zr-O	4	2.32	-	-
	Zr-Zr	12	3.62	-	
M-ZrO_2	Zr-O	2.7	2.04	0.0050	0.0003
	Zr-Zr	4.4	3.41	0.0070	
$Zr_{0.01}TiO_2$	Zr-O	6.8	2.09	0.0065	
	Zr-Ti	1.0	2.34	0.0066	0.0015
	Zr-Ti	3.7	3.12	0.0070	
$Zr_{0.03}TiO_2$	Zr-O	2.0	2.06	0.0010	
	Zr-Ti	1.0	2.31	0.0075	0.0003
	Zr-Zr	2.2	2.97	0.0090	
$Zr_{0.05}TiO_2$	Zr-O	2.0	2.02	0.0020	
	Zr-Ti	2.3	2.20	0.0050	0.0011
	Zr-Zr	1.2	3.01	0.0090	
$Zr_{0.1}TiO_2$	Zr-O	3.4	2.10	0.0030	
	Zr-Zr	3.4	2.71	0.0060	0.0015
	Zr-Zr	2.6	3.40	0.0070	

[a] References data.

4-6.   Optical property

The intrinsic and extrinsic band gaps of the photocatalysts were determined by using UV-vis spectrophotometry.   The UV-vis absorption spectra of TiO_2 and Zr_xTiO_2 were shown in Figure 4-12.   Based on the adsorption edges of UV-vis absorption curves, the estimated band gaps were listed in Table 4-6.   The intrinsic band gap of TiO_2 was 3.09 eV which is smaller than that of anatase TiO_2 (3.2 eV), revealing that the mesoporous material possess numerous defects caused by the spheroidic micelle during evaporation-induced process.   The band absorptions of the $Zr_{0.02}TiO_2$ and $Zr_{0.03}TiO_2$ slightly shift to shorter wavelengths of 3.15 and 3.14 eV, respectively, indicating broadened band gaps.   This phenomenon proved that the TiO_2 lattice would be condensed with a trace amount of Zr^{4+} ions on the surface to prevent the defect generation, corresponding to XRD results.   Due to the formation of defects caused by excess Zr^{4+} ions incorporated into the lattice of TiO_2, the red shifts and reduced band gaps were resulted since the Zr/Ti ratios increases above 0.04. The extrinsic band gap decrease from 2.41 to 2.34 eV when the doping concentration of the Zr^{4+} ion increased from 4% to 1%.

The UV-vis spectra of pure TiO_2 and Au-loaded TiO_2 are displayed in Figure 4-13.   It is apparent that a broad absorption peak can be found and the sub-band gaps of these samples were 3.08 to 3.11 eV.   Moreover, a new significant absorption peak occurred in the region of 500-650 nm are observed for 0.5% $Au-TiO_2$ and 1.0% $Au-TiO_2$ samples.   This phenomenon is attributed to the surface plasmon resonance (SPR) effect of spatially confined electron in the gold nanoparticles.   For the 0.1% Au/TiO_2, a very weak surface plasmon resonance adsorption band in the region is observed.   It is well known that the surface plasmon resonance of metallic nanoparticles is associated with particle size, loading amount and surrounding environment.   The results clearly demonstrated that the $Au-TiO_2$ had a

significant red-shift of absorption peak due to the large particle size with loading increased.

Compared with the SPR band of Au nanoparticles ranged at 500-650 nm, the 2.0%, 4.0% and

8.0% $Au-TiO_2$ catalysts show an extrinsic band gap from 2.46 to 2.42 eV.   It is because that

the interparticle electron transfer between gold cluster and TiO_2 drive the hole migrated to

higher energy level to extend the absorption region
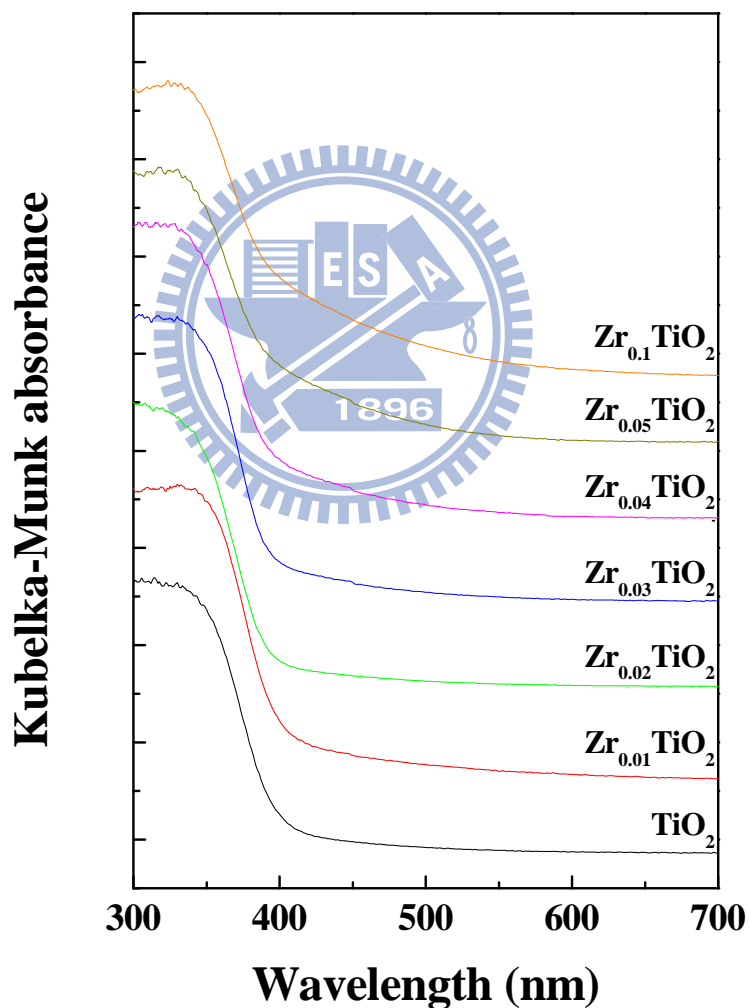
Figure 4-12 UV-vis spectra of mesoporous TiO_2 and Zr_xTiO_2 samples.

Table 4-7 Band gap energy of mesoporous TiO_2 and Zr_xTiO_2 samples.

Sample	Intrinsic Band gap (eV)	Extrinsic Band gap (eV)
TiO_2	3.09	-[a]
$Zr_{0.01}TiO_2$	3.08	-
$Zr_{0.02}TiO_2$	3.15	-
$Zr_{0.03}TiO_2$	3.14	-
$Zr_{0.04}TiO_2$	3.08	2.41
$Zr_{0.05}TiO_2$	3.03	2.38
$Zr_{0.1}TiO_2$	2.99	2.34

[a] Not detectable.

8.0% Au-TiO$_2$

4.0% Au-TiO$_2$

2.0% Au-TiO$_2$

1.0% Au-TiO$_2$

0.5% Au-TiO$_2$
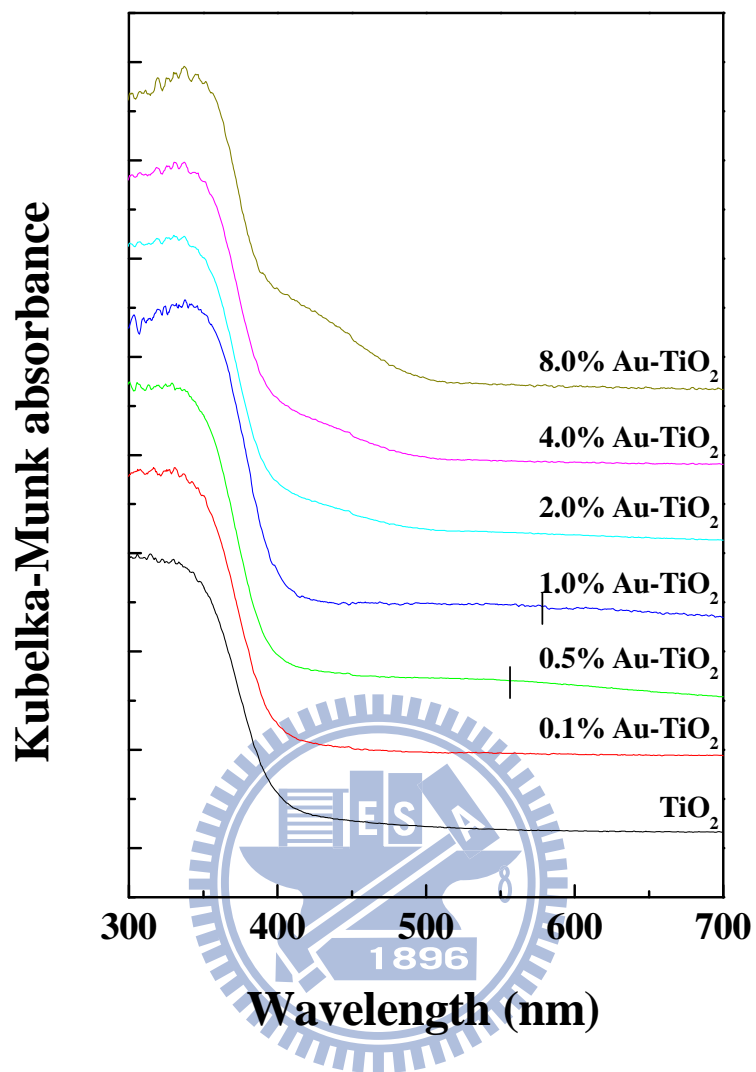
0.1% Au-TiO$_2$

TiO$_2$

Figure 4-13 UV-vis spectra of mesoporous TiO$_2$ and x% Au-TiO$_2$ samples.

Table 4-8 Band gap energy of mesoporous TiO_2 and $x\%$ Au-TiO_2 samples.

Sample	Intrinsic Band gap (eV)	Extrinsic Band gap (eV)
TiO_2	3.09	-
0.1% Au-TiO_2	3.10	-
0.5% Au-TiO_2	3.11	-
1.0% Au-TiO_2	3.10	-
2.0% Au-TiO_2	3.10	2.46
4.0% Au-TiO_2	3.09	2.43
8.0% Au-TiO_2	3.08	2.42

[a] Not detectable.

4-7.   Photodegradation of RhB

To select a catalyst which exhibits the highest photocatalytic activity for the following photoreduction experiment, photodecomposition of Rhodamine B (RhB) by the pure and doped TiO_2 was carried out.   Figure 4-14 shows the decoloration of RhB in the presence of the pure and Zr-doped TiO_2 samples.   Compared to pure TiO_2, the reduced reactivity of $Zr_{0.01}TiO_2$ is due to that the defects created by Zr^{4+} ions which promote the charge recombination.   The $Zr_{0.02}TiO_2$ and $Zr_{0.03}TiO_2$ samples exhibited higher degradation efficiency attributed to the fine TiO_2 crystal and a few defects at the surface lattice. However, an excessive number of defects can facilitate the charge recombination and decrease the amounts of effective charge carries.   It is demonstrated that the $Zr_{0.04}TiO_2$ and $Zr_{0.04}TiO_2$ present lower photoactivity toward RhB.   Figure 4-15 displays the photocatalytic activities of the pure and Au-TiO_2 samples.   These results indicated that the Au-loaded samples exhibited lower photoactivity.   All the Au-loaded TiO_2 samples have similar pore structure, crystalline phase and band gap, implying that the coverage of TiO_2 caused by Au nanoparticles had a negative influence on the photocativites.   The 1.0% Au-TiO_2 sample has higher degradation rate due to its optimal Au content, it is associated with the fine Au nanoparticles and sufficient activity sites of TiO_2.   The $Zr_{0.03}TiO_2$ and 1.0% Au-TiO_2 were selected for the following photoreduction of CO_2.

However, the RhB was totally decomposed by Degussa P25 within just 2 minutes.   The TiO_2, Zr_xTiO_2 and Au-TiO_2 materials exhibited lower degradation efficiencies compared to the commercial catalyst.   These results reveal that high specific surface area has little contribution to the photoactivity of the porous TiO_2 in aqueous phase.   High surface tension between the liquid and the inorganic wall prevent the target compound entering into the pores and leads the internal surface area becoming useless.
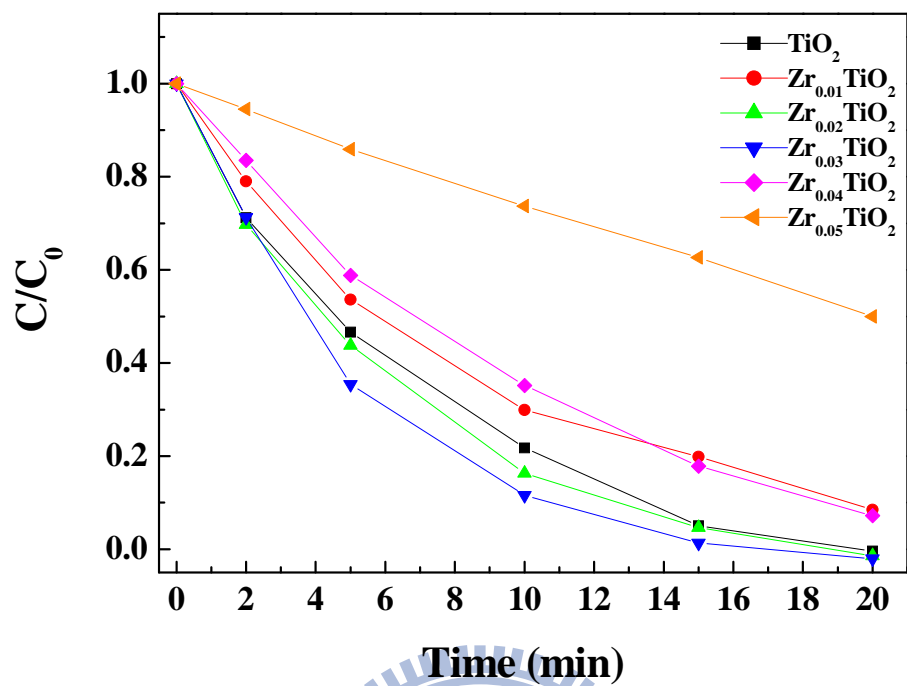
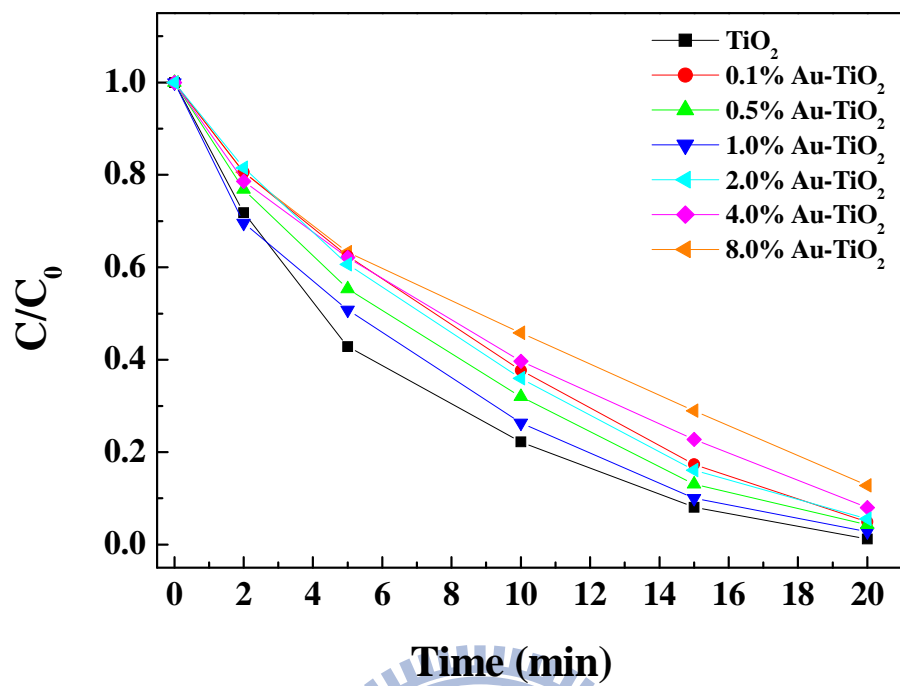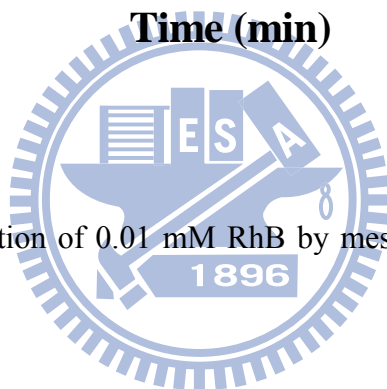Figure 4-14 The photodegradation of 0.01 mM RhB by mesoporous TiO_2 and Zr_xTiO_2 samples.

Figure 4-15 The photodegradation of 0.01 mM RhB by mesoporous TiO_2 and x% $Au\text{-}TiO_2$ samples.

4-8. CO$_2$ adsorption isotherm

The surface property and specific surface area play an important role in photocatalytic reduction of gaseous CO$_2$, which determined the adsorption affinity and capacity of reactant on the catalyst surface. The CO$_2$ adsorption-desorption isotherms of the samples were examined (See Appendix E), and the adsorption constant (K) and adsorption capacity (X_m) were derived according to the Langmuir equation. Table 4-8 lists the K and X_m values of the commercial P25, mesoporous TiO$_2$, Zr$_{0.03}$TiO$_2$ and 1.0% Au-TiO$_2$. The X_m values of P25 and TiO$_2$ were 9.88 mg CO$_2$ g^{-1} and 24.45 mg CO$_2$ g^{-1} and the K values were 59.53 g mg^{-1} and 102.25 g mg^{-1}, respectively. Relative to P25, the higher adsorption capacity and adsorption affinity of the TiO$_2$ are resulted from the larger specific surface area as well as the surface defect and oxygen vacancies. Compared to the TiO$_2$, the surface area of Zr$_{0.03}$TiO$_2$ increased by 1.4 times, but its adsorption capacity (29.33 mg CO$_2$ g^{-1}) was only increased by 1.2 times. The lower adsorption constant of the doped TiO$_2$ is attributed to its fine structure on the surface. The 1.0% Au-TiO$_2$ has a similar adsorption constant of 114.74 g mg^{-1} but a relatively lower adsorption capacity of 12.54 g mg^{-1} compared with TiO$_2$. It was reported that both the isolated metallic sites and perimeter sites of gold loaded on the TiO$_2$ surface were preferable to adsorb O$_2$ and CO instead of CO$_2$[12]. Therefore, the Au nanoparticles covered the adsorption sited of TiO$_2$ surface, thus reducing its adsorption capacity.

Table 4-9 The adsorption constant (K) and saturated adsorbed amount (X_m) of catalysts toward CO_2 at 273 K.

Sample	K	X_m (mg CO_2/g)
P25	59.53	9.88
TiO_2	102.25	24.45
1.0% Au-TiO_2	114.74	12.54
$Zr_{0.03}TiO_2$	85.25	29.33

4-9.　　Photoreduction of CO_2

The photoreduction products of CO_2 were analyzed varies irradiation intervals using GC/FID and the accumulated amounts of products were recorded.　Methane (CH_4) was the sole product for all the samples.　Figure 4-16 shows the accumulated yields of CH_4 upon the irradiation time.　The accumulated yield and quantum efficiency of methane production over different catalysts are summerized in Table 4-9.　The production of CH_4 on the commercial P25 was negligible during 24 hr irradiation, revealing a poor photoreduction activity of P25 for CO_2.　In the presences of the TiO_2, CH_4 constantly increased with irradiation time and reached the highest value of 1.03 μ mole g^{-1} catalyst at 4th hr.　Subsequently, the accumulated amount of CH_4 was declined to 0.45 μ mole at 8th hr.　The generation of CH_4 in the first and in the 8 hrs was adopted to calculate the initial and total quantum efficiency of the catalysts.　The initial and total quantum efficiencies of the TiO_2 catalyst were calculated as 3.30 % and 0.26 %, respectively.　The high specific surface area and excellent adsorption affinity of the mesoporors structure resulted in the outstandingly high initial quantum efficiency for CO_2.　However, the deterioration of CH_4 production rate was caused due to reoxidation of the CH_4 with adsorbed hydroxyl (OH) group.

Low CH_4 yield and initial quantum efficiency of 0.23 μ mole and 1.06 %, respectively were measured in the $Zr_{0.03}TiO_2$ system.　However, the CH_4 yield reached 0.81 μ mole after the illumination for 8 hr, which was 1.8 times higher than TiO_2.　This phenomenon implies that the trap centers generated by Zr^{4+} ions exhibits a lower reduction potential, and decreasing the photoreduction activity at first hour.　The 1.0% Au-TiO_2 generated 0.33 μ mole CH_4 in the beginning.　The CH_4 content continuously increased to 0.54 μ mole at the 8th hour.　The less initial rate of CH_4 formation may be attributed to the Fermi level created by gold nanoparticles on the surface which possess a lower reduction potential.
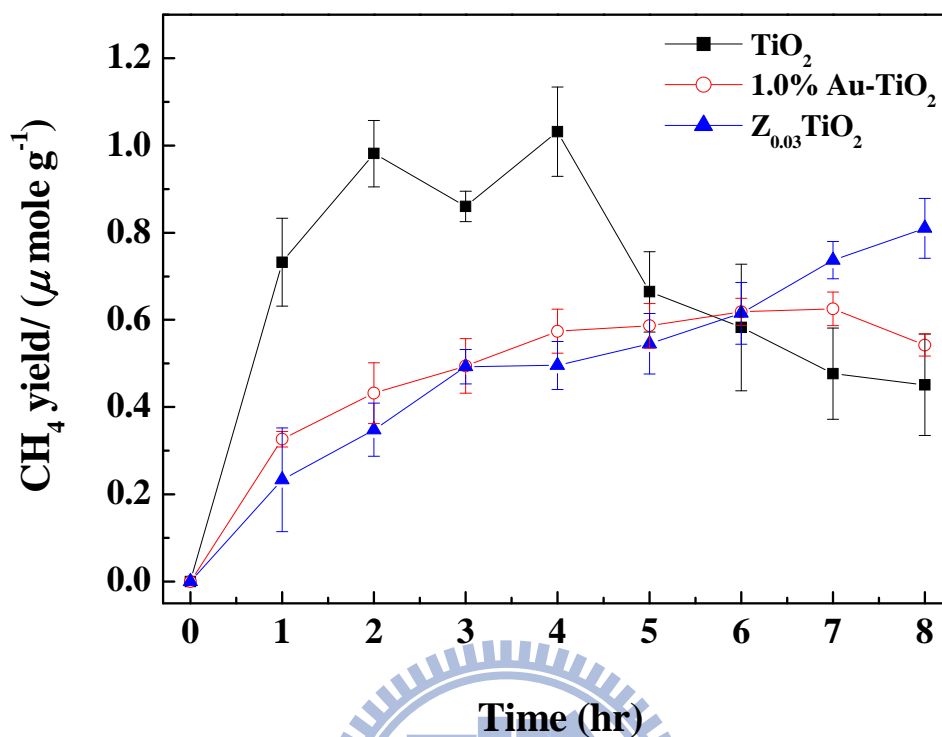
Figure 4-16 Time dependence on the production yield of CH_4 over catalysts.

Table 4-10 The methane yields, initial and total quantum efficiency (Φ_E), of catalysts

Sample	Methane yields (μ mole g^{-1})	Initial Φ_E (%)	Total Φ_E (%)
P25	-[a]	-	-
TiO_2	0.45	3.30	0.26
$Zr_{0.03}TiO_2$	0.81	1.06	0.46
1.0% Au-TiO_2	0.54	1.47	0.31

[a] Not detectable.

4-10. EPR results

EPR has been widely used to understand the photocatalytic mechanism in terms of examining the paramagnetic species formed in the photocatalysis. Electrons and holes are generated within femto-second scale when TiO_2 nanoparticles are activated with the photons having the energy larger than their bandgap. These charge carriers are subsequently trapped and followed by recombination. To acquire the EPR signals with high quality, the measurement was carryout out at 77 K to prevent severe recombination.

Figure 4-17 shows the EPR spectra of mesoporous TiO_2, $Zr_{0.03}TiO_2$ and 1.0% Au-TiO_2 samples recorded under vacuum at 77 K in the darkness and with UV irradiation. There was no obvious peak appearing in all the samples before irradiation. When the light was turned on, the pure TiO_2 sample showed two sets of g-values at $g_1 = 2.029$, $g_2 = 2.015$ and $g_3 = 2002$, and signals $g_1 = 2.023$, $g_2 = 2.015$ and $g_3 = 2.007$, which are assigned to the Ti^{4+}-$O^{-\bullet}{}_{surf}$ and Ti^{4+}-$O^{-\bullet}{}_{bulk}$ species, respectively. In addition, a set of g-values at $g_1 = 2.035$, $g_2 = 2.007$ and $g_3 = 2002$, which is assigned to Ti^{4+}-$O_2H^{\bullet}$ species. This species is formed by the reaction of O_2 and H^+ with Ti^{3+} ions on the hydrated surface. These signals decreased after irradiation for 40 min because some of them are consumed to oxidize surface contaminate. Electron trapping at Ti^{3+} species in the anatase lattice was found at $g_\perp = 1.991$ and $g_\parallel = 1.957$. In contrast to the trapped holes which are reduced after long term irradiation, the intensity of the trapped electrons increased with the irradiation time. In the $Zr_{0.03}TiO_2$ sample, the intensities of the signals of the Ti^{3+} species decreased after long term irradiation, revealing the electrons transfer from the Ti^{3+} centers to the Zr^{4+} ions locating beyond the conduction band. Trapping electrons at the impurities would suppress the charge recombination. The signals of the trapped holes remarkably increased in the $Zr_{0.03}TiO_2$ sample after long term irradiation. As the result, the doped sample exhibited higher

photocatalytic activity than the pure TiO_2. The signals of bulk trapped holes (Ti^{4+}-$O^{-\bullet}{}_{bulk}$) disappeared in the $Zr_{0.03}TiO_2$ sample, indicating the fine crystalline structure inside the lattice. The fine structure also contributes to the higher quantity of surface trapped holes and improves the photocatalytic activity. The T^{3+} species was not detected in the Au-TiO_2 sample due to efficient transfer of electrons from the condition band to the Au nanoparticles. However, such electron transfer did not enhance the intensities of the trapped holes. Mediating electrons to fill the holes in the valence band via the Au nanoparticles is thus suggested. The consumption of charge carriers at the surface also causes poor activity for RhB degradation.

To understand the role of water vapor in the reduction kinetics, the EPR spectra of the samples were further acquired under humidified N_2 atmosphere. To avoid the interference from the surface contaminant, all the samples were irradiated with UV light under humidified air at 393 K for 8h prior to the measurements. Figure 4-18 shows the EPR spectra of the pure TiO_2, $Zr_{0.03}TiO_2$, and 1.0 % Au-TiO_2 samples irradiated with UV light under humidified N_2 atmosphere. All the measurements were carried out at 77 K. Compared to the results recorded under vacuum, the presence of water vapor greatly decreased the both the signals of trapped holes and electrons. This phenomenon reveals that the OH^- and H^+ ions dissociated from water act as hole and electron scavengers, respectively, to remove the surface trapped charge carriers. Moreover, it suggests the competition between the H^+ ions and CO_2 in the photocatalytic reduction.

Figure 4-19 shows the EPR spectra of the pure TiO_2, $Zr_{0.03}TiO_2$, and 1.0 % Au-TiO_2 samples irradiated with UV light at 77K under CO_2 atmosphere. At the beginning, the signals of both the trapped holes and electrons were less intensive in all these samples. This finding indicates that the electron transfer from the conduction band to the adsorbed CO_2

molecules is highly efficient. However, the electrons promptly are delivered to the holes from the CO_2 radicals. After 40-min irradiation, the quantity of the trapped holes increased in the TiO_2 and $Zr_{0.03}TiO_2$ samples. It was reported that the CO_2 radicals are able to react with the H^+ ions, which come from the surface hydroxyl groups, to form methoxyl radicals[120]. Once the methoxyl radicals are generated, the electron mediating process between the conduction and the valence band is inhibited. The $Zr_{0.03}TiO_2$ sample had larger numbers of surface hydroxyl groups than the pure TiO_2 sample, thus more holes are stabilized at the surface.

Figure 4-20 shows the EPR spectra of the pure TiO_2, $Zr_{0.03}TiO_2$, and 1.0 % Au-TiO_2 samples irradiated with UV light at 77K under humidified CO_2 atmosphere. It is worthy to note that the co-existence of CO_2 and water vapor led the signals of the trapped holes in the mesoporous TiO_2 sample becoming intensive at the beginning of irradiation. In addition, the number of the trapped electrons increased with the irradiation time, while the bulk trapped holes decreased its intensity. This phenomenon indicates that the interfacial charge transfer is retarded in the humidified CO_2. Since fast interaction of the electrons and holes with individual CO_2 and water has been demonstrated, the inhibited interfacial charge transfer in the humidified CO_2 is attributed to the formation of reductive intermediates. Reduction of CO_2 into hydrocarbons involves with H^+ ions which are provided from water. The EPR result indicates that the first electron receiving by CO_2 and water dissociation are rapid. However, further reduction of the hydrocarbon intermediate is limited. The intermediate block the surface active sites to prevent the interfacial charge transfer to water and CO_2, consequently causes the low reduction efficiency. The Au-loaded TiO_2 samples had more intensive signals for the trapped holes. The Au nanoparticles not only had little contribution to charge utilization, but also reduce the surface active sites for CO_2 reduction.

Therefore, the Au-TiO_2 showed a lower reductive activity than pure TiO_2. Relative to

the pure TiO_2 and Au-TiO_2 samples, the $Zr_{0.03}TiO_2$ photocatalyst showed fewer amounts of surface trapped holes, indicating that the doped sample has more efficient interaction with water. Its high surface hydrophilicity and relatively poor affinity toward CO_2 could result in its preferential interaction with water instead of CO_2. Such effect also determines the low activity of the doped TiO_2 sample for CO_2 reduction.

Some of intermediates are successfully reduced to CH_4. However, reaction of the CH_4 with OH radicals again returns this product to CO_2. Such re-oxidation is dominant in the pure TiO_2-based system when the accumulated CH_4 reached 1.0 μmole/g after irradiation for 4 h, and the equilibrium is likely to achieve when the CH_4 yield decreased to 0.4-0.5 μmole/g. Loading of Au nanoparticles did not change the equilibrium. However, the $Zr_{0.03}TiO_2$ sample constantly produced CH_4 till the yield of 0.9 μmole/g. Since the doped TiO_2 sample has stronger interaction with water, larger amounts of surface OH radicals are supposed to be generated. The inhibited re-oxidation in the $Zr_{0.03}TiO_2$-based system suggests that the oxidation of CH_4 products does not take place at the surface, but mainly involves with dissociated radicals. Higher density of intermediates on the TiO_2 surface assists detachment of OH radicals, thus accelerating the backward reaction. The reduction mechanisms in the presence of the pure TiO_2, Au-TiO_2 and $Zr_{0.03}TiO_2$ are illustrated in Figure 4-21, 22, 23 and 24.
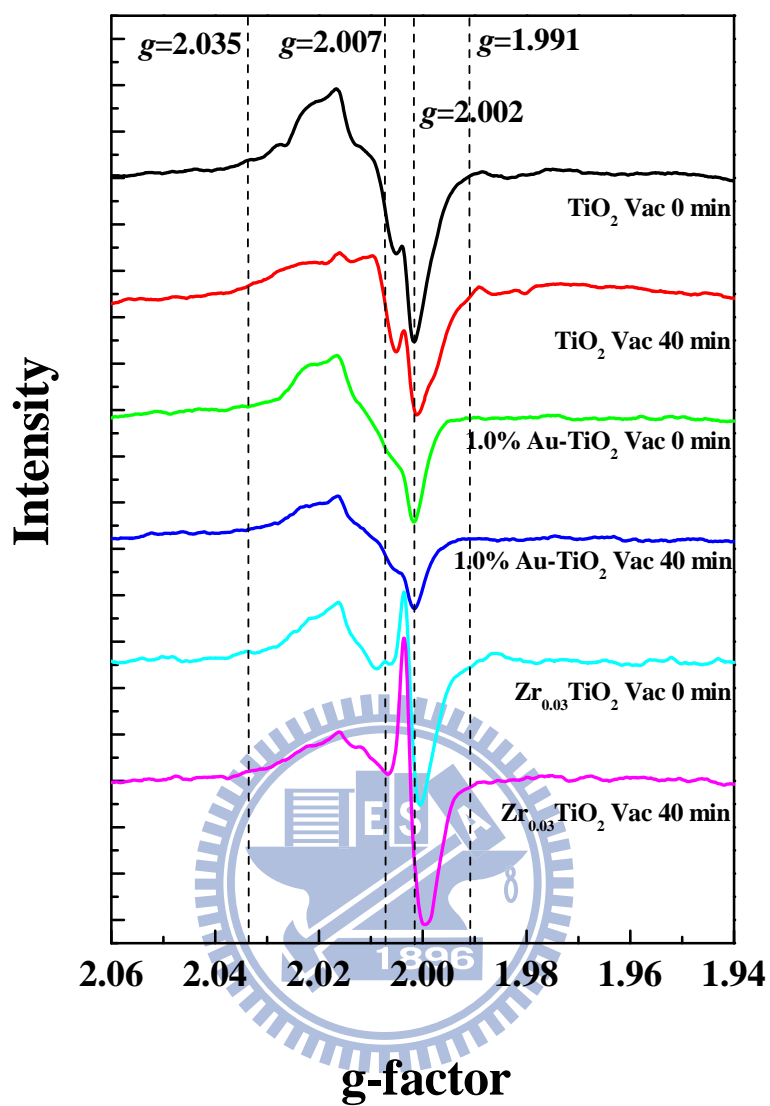
Figure 4-17 EPR spectra of mesoporus TiO_2, $Zr_{0.03}TiO_2$ and 1.0% Au-TiO_2 under UV irradiation at 77K with vacuum system.

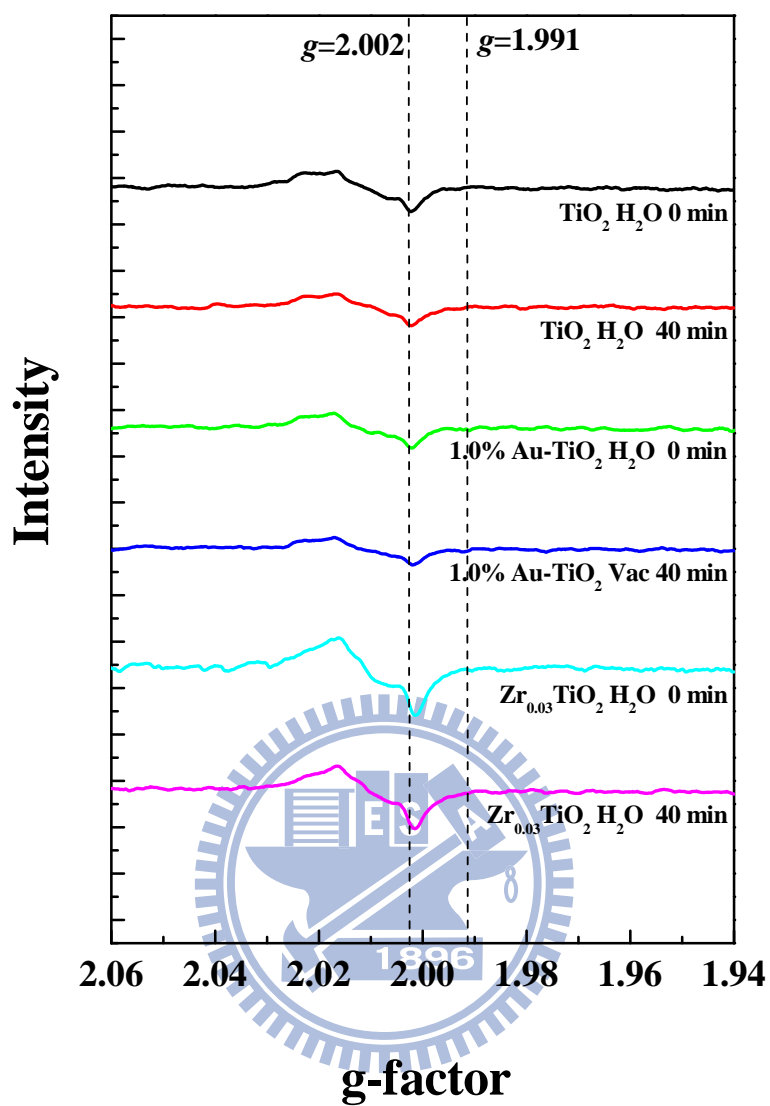Figure 4-18 EPR spectra of mesoporus TiO_2, $Zr_{0.03}TiO_2$ and 1.0% Au-TiO_2 under UV irradiation at 77K with N_2/H_2O.

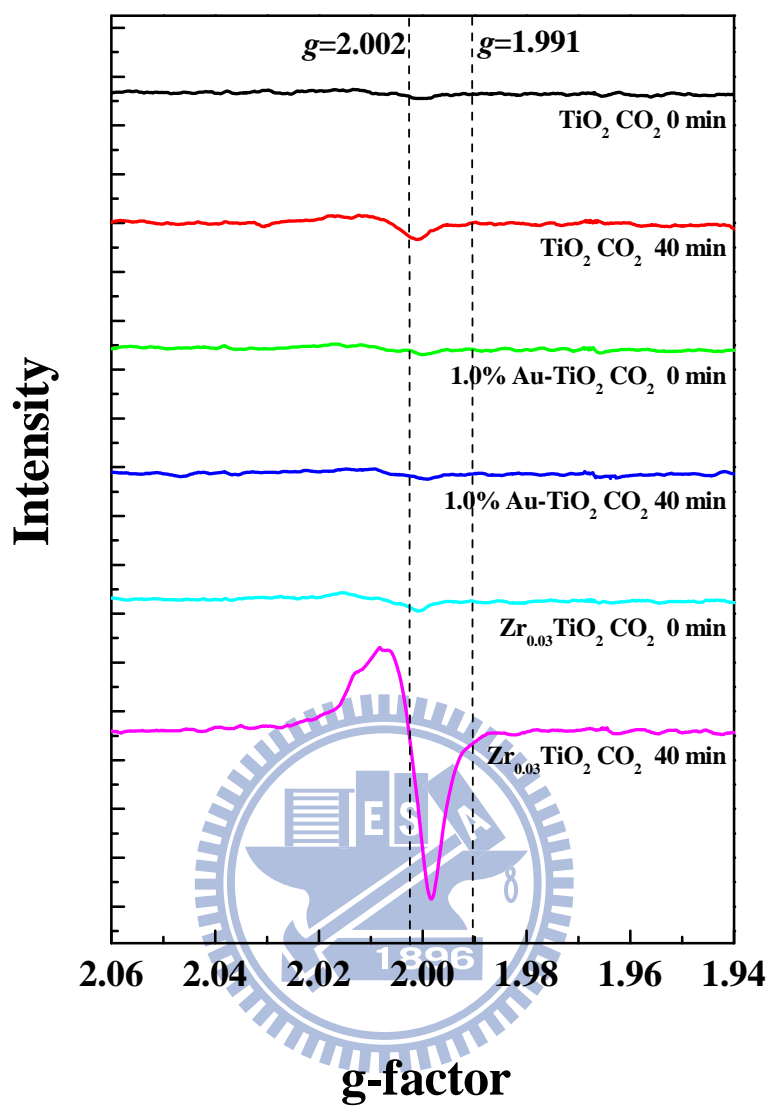Figure 4-19 EPR spectra of mesoporus TiO_2, $Zr_{0.03}TiO_2$ and 1.0% Au-TiO_2 under UV irradiation at 77K with dry CO_2 gas.
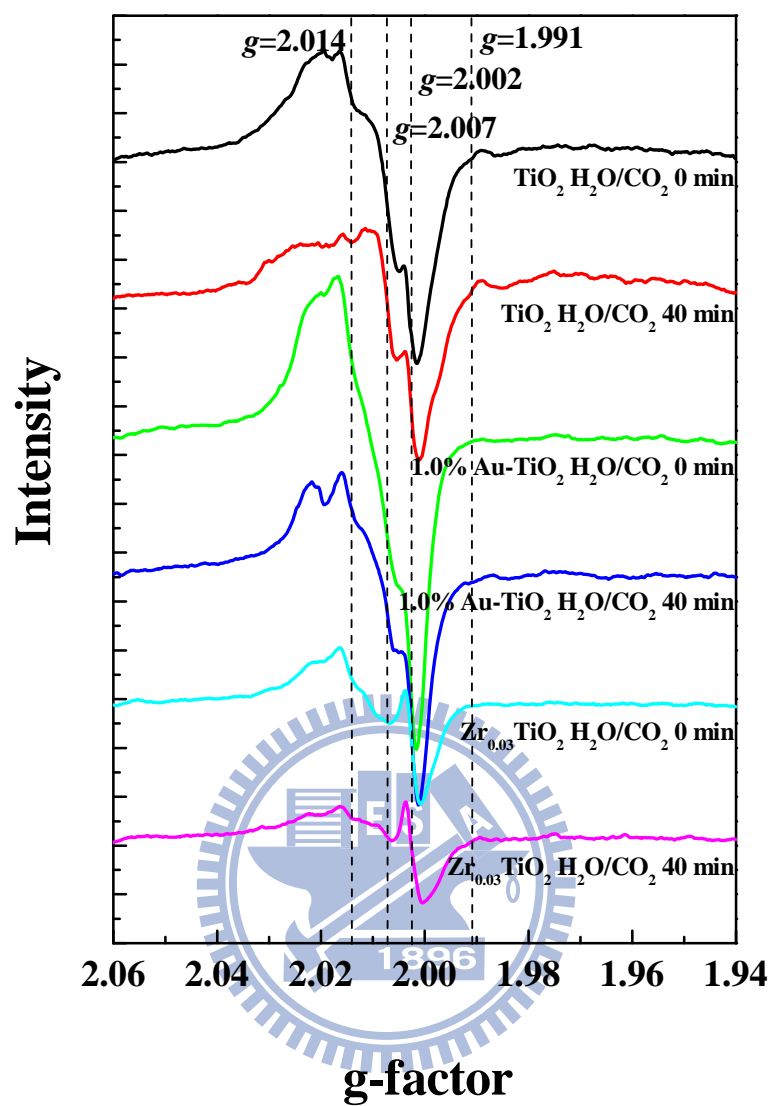
Figure 4-20 EPR spectra of mesoporous TiO_2, $Zr_{0.03}TiO_2$ and 1.0% Au-TiO_2 under UV irradiation at 77K with CO_2/H_2O.
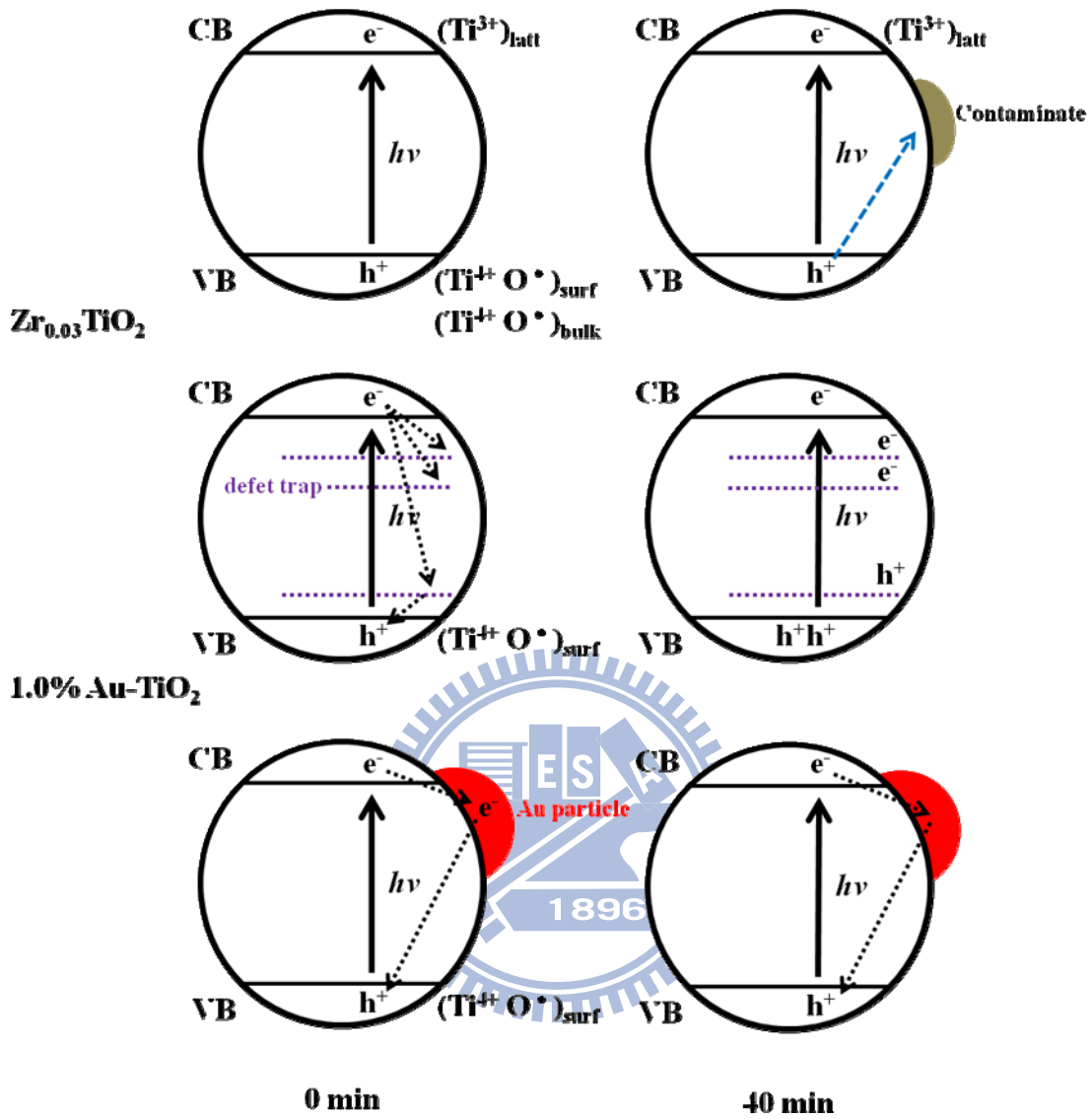
Figure 4-21 The concept of mesoporus TiO_2, $Zr_{0.03}TiO_2$ and 1.0% Au-TiO_2 under UV irradiation at 77K with vacuum system.
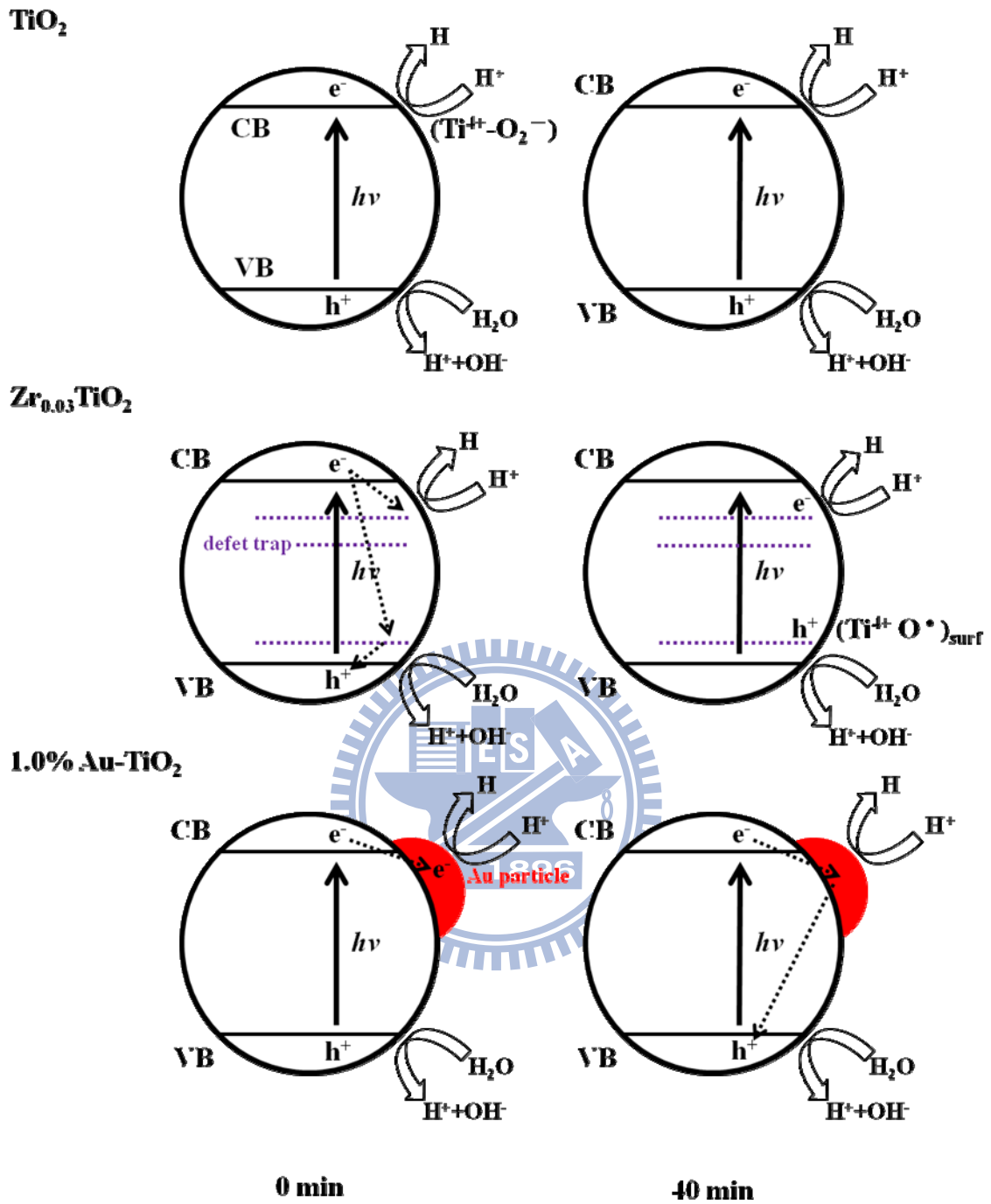
Figure 4-22 The concept of mesoporus TiO_2, $Zr_{0.03}TiO_2$ and 1.0% Au-TiO_2 under UV irradiation at 77K with N_2/H_2O.
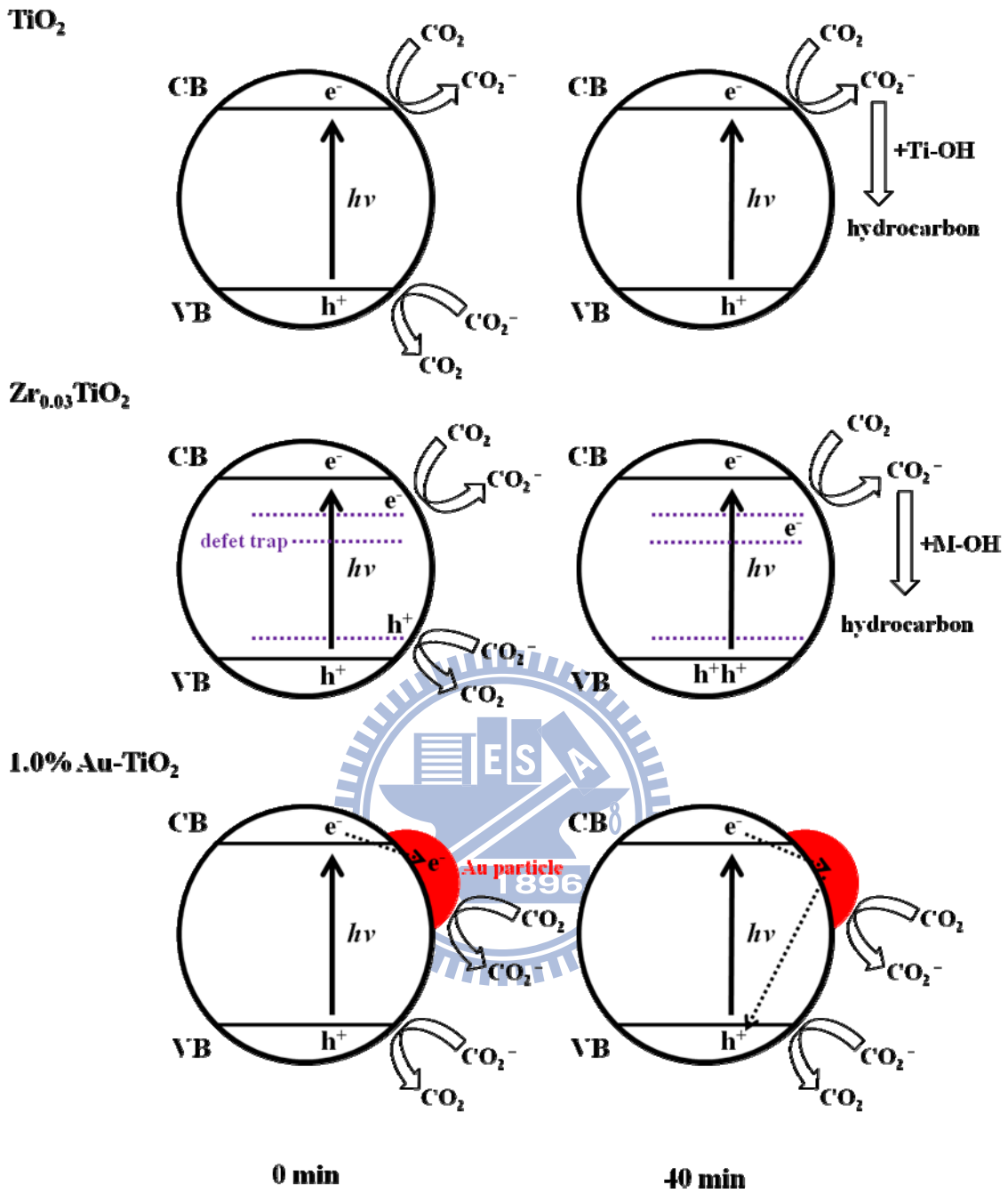
Figure 4-23 The concept of mesoporus TiO_2, $Zr_{0.03}TiO_2$ and 1.0% Au-TiO_2 under UV irradiation at 77K with dry CO_2 gas.
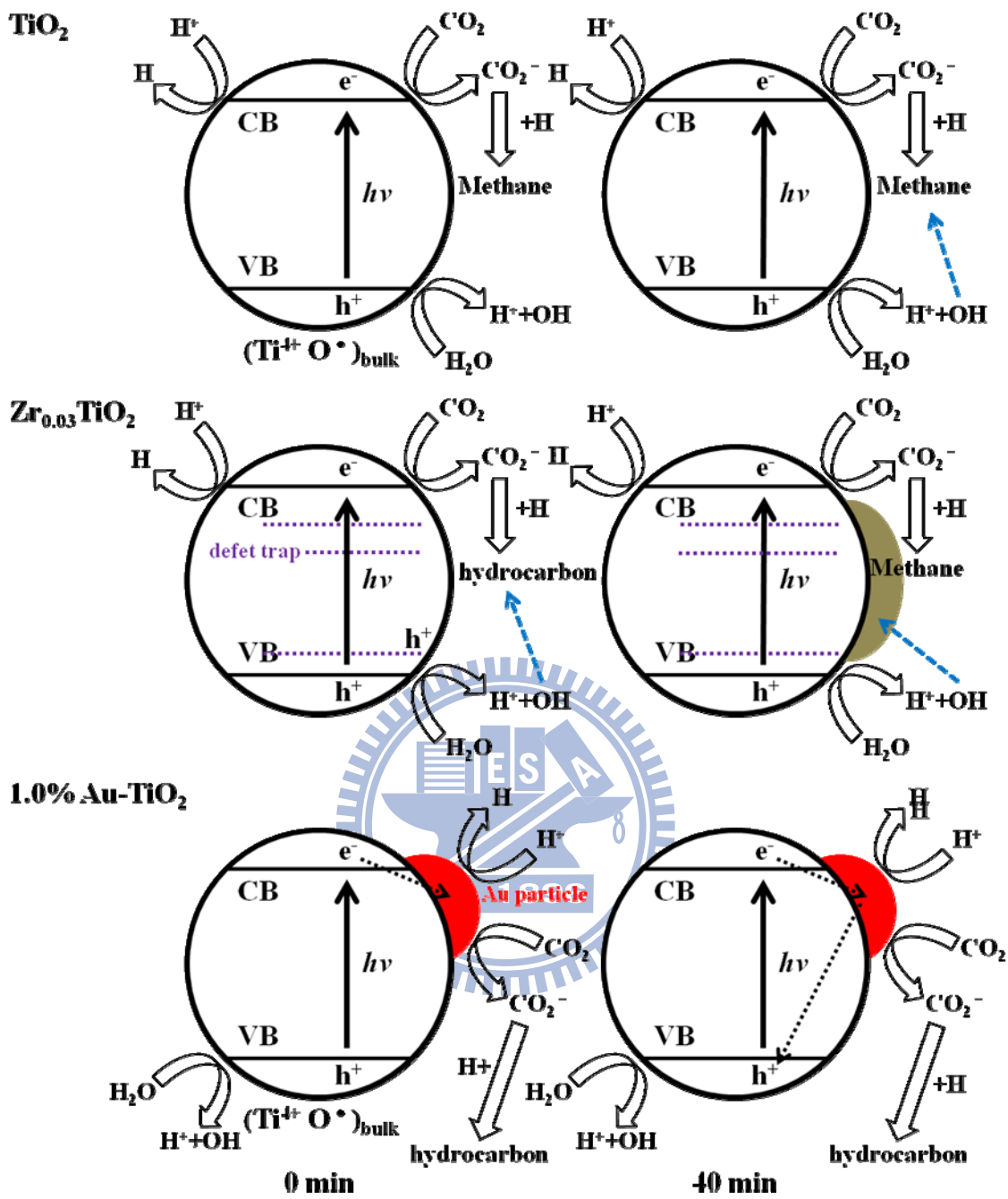
Figure 4-24 The concept of mesoporus TiO_2, $Zr_{0.03}TiO_2$ and 1.0% Au-TiO_2 under UV irradiation at 77K with CO_2/H_2O.

Chapter 5.   Conclusions

The mesoporous Zr-doped TiO_2 catalysts have been successfully synthesized via an EISA process.   Slower hydrolysis rate of Zr^{4+}-acetylacetone complex than that of Ti^{4+} complex resulted in surface doping.   The DP method was utilized to obtain small gold particles loading on the catalysts surface.   Compared to the general oxidation, the efficiency of CO_2 photoreduction were controlled by a competition between the reductive potential of catalysts toward gaseous CO_2 and oxidative reactivity of products.   The TiO_2 exhibits a high CO_2 photoreduction rate but the CH_4 generation was gradually decreased, indicating the hole pairs would generate OH radicals with water to oxidized the products.   Although the Au-loaded catalyst had a relatively low reduction potential, the hole pairs were captured by gold particle.   In addition, the Zr-doped samples demonstrate a higher specific surface area, hydrophilic property and a few defects at the surface or into the bulk.   The effect as trapping centers also caused a poor photoreduction activity but prevented the reoxidation of CH_4 with OH radicals.
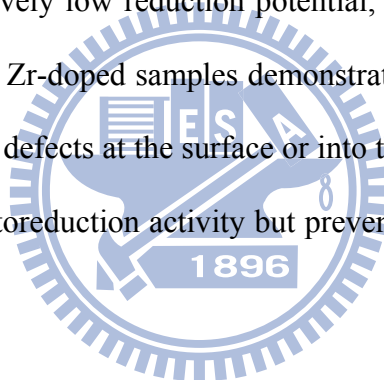
References

1. Roy, S.C., Varghese, O.K., Paulose, M., and Grimes, C.A., "Toward Solar Fuels: Photocatalytic Conversion of Carbon Dioxide to Hydrocarbons", *Acs Nano*, **2010**, 4 (3), 1259-1278.

2. Huo, Q.S., Margolese, D.I., Ciesla, U., Feng, P.Y., Gier, T.E., Sieger, P., Leon, R., Petroff, P.M., Schuth, F., and Stucky, G.D., "Generalized Synthesis of Periodic Surfactant Inorganic Composite-Materials", *Nature*, **1994**, 368 (6469), 317-321.

3. Beck, J.S., Vartuli, J.C., Roth, W.J., Leonowicz, M.E., Kresge, C.T., Schmitt, K.D., Chu, C.T.W., Olson, D.H., Sheppard, E.W., Mccullen, S.B., Higgins, J.B., and Schlenker, J.L., "A New Family of Mesoporous Molecular-Sieves Prepared with Liquid-Crystal Templates", *Journal of the American Chemical Society*, **1992**, 114 (27), 10834-10843.

4. Corma, A., "From microporous to mesoporous molecular sieve materials and their use in catalysis", *Chemical Reviews*, **1997**, 97 (6), 2373-2419.

5. He, X. and Antonelli, D., "Recent advances in synthesis and applications of transition metal containing mesoporous molecular sieves", *Angewandte Chemie-International Edition*, **2001**, 41 (2), 214-229.

6. Wight, A.P. and Davis, M.E., "Design and preparation of organic-inorganic hybrid catalysts", *Chemical Reviews*, **2002**, 102 (10), 3589-3613.

7. De Vos, D.E., Dams, M., Sels, B.F., and Jacobs, P.A., "Ordered mesoporous and microporous molecular sieves functionalized with transition metal complexes as catalysts for selective organic transformations", *Chemical Reviews*, **2002**, 102 (10), 3615-3640.

8. Brinker, C.J., Lu, Y.F., Sellinger, A., and Fan, H.Y., "Evaporation-induced self-assembly: Nanostructures made easy", *Advanced Materials*, **1999**, 11 (7), 579.

9. Yang, P.D., Zhao, D.Y., Margolese, D.I., Chmelka, B.F., and Stucky, G.D., "Generalized syntheses of large-pore mesoporous metal oxides with semicrystalline frameworks", *Nature*, **1998**, 396 (6707), 152-155.

10. Das, D., Mishra, H.K., Pradhan, N.C., Dalai, A.K., and Parida, K.M., "Studies on structural properties, surface acidity and benzene isopropylation activity of sulphated ZrO_2-TiO_2 mixed oxide catalysts", *Microporous and Mesoporous Materials*, **2005**, 80 (1-3), 327-336.

11. Zorn, M.E., Tompkins, D.T., Zeltner, W.A., and Anderson, M.A., "Photocatalytic oxidation of acetone vapor on TiO_2/ZrO_2 thin films", *Applied Catalysis B-Environmental*, **1999**, 23 (1), 1-8.

12. Haruta, M., "Novel catalysis of gold deposited on metal oxides", *Catalysis Surveys of Japan*, **1997**, 1 61-73.

13. Anpo, M., Yamashita, H., Ichihashi, Y., Fujii, Y., and Honda, M., "Photocatalytic reduction of CO_2 with H_2O on titanium oxides anchored within micropores of zeolites: Effects of the structure of the active sites and the addition of Pt", *Journal of Physical Chemistry B*, **1997**, 101 (14), 2632-2636.

14. Li, Y., Wang, W.N., Zhan, Z.L., Woo, M.H., Wu, C.Y., and Biswas, P., "Photocatalytic reduction of CO_2 with H_2O on mesoporous silica supported Cu/TiO_2 catalysts", *Applied Catalysis B-Environmental*, **2010**, 100 (1-2), 386-392.

15. Sasirekha, N., Basha, S.J.S., and Shanthi, K., "Photocatalytic performance of Ru doped anatase mounted on silica for reduction of carbon dioxide", *Applied Catalysis B-Environmental*, **2006**, 62 (1-2), 169-180.

16. Fujishima, A. and Honda, K., "Electrochemical Photolysis of Water at a Semiconductor Electrode", *Nature*, **1992**, 238 37-38.

17. Hoffmann, M.R., Martin, S.T., Choi, W.Y., and Bahnemann, D.W., "Environmental Applications of Semiconductor Photocatalysis", *Chemical Reviews*, **1995**, 95 (1), 69-96.

18. Bilmes, S.A., Mandelbaum, P., Alvarez, F., and Victoria, N.M., "Surface and electronic structure of titanium dioxide photocatalysts", *Journal of Physical Chemistry B*, **2000**, 104 (42), 9851-9858.

19. Linsebigler, A.L., Lu, G.Q., and Yates, J.T., "Photocatalysis on TiO_2 Surfaces-Principles, Mechanisms, and Selected Results", *Chemical Reviews*, **1995**, 95 (3), 735-758.

20. Parida, K.M., Sahu, N., Biswal, N.R., Naik, B., and Pradhan, A.C., "Preparation, characterization, and photocatalytic activity of sulfate-modified titania for degradation of methyl orange under visible light", *Journal of Colloid and Interface Science*, **2008**, 318 (2), 231-237.

21. Zhang, Z.B., Wang, C.C., Zakaria, R., and Ying, J.Y., "Role of particle size in nanocrystalline TiO_2-based photocatalysts", *Journal of Physical Chemistry B*, **1998**, 102 (52), 10871-10878.

22. Gratzel, M., "Photoelectrochemical cells", *Nature*, **2001**, 414 (6861), 338-344.

23. Sanjines, R., Tang, H., Berger, H., Gozzo, F., Margaritondo, G., and Levy, F., "Electronic-Structure of Anatase TiO_2 Oxide", *Journal of Applied Physics*, **1994**, 75 (6), 2945-2951.

24. Diebold, U., "The surface science of titanium dioxide", *Surface Science Reports*, **2003**, 48 (5-8), 53-229.

25. Ebelmen, H.M., *Annales de Chimie et de Physique*, **1846**, 16 129.

26. Barringer, E.A. and Bowen, H.K., "Formation, Packing, and Sintering of Monodisperse TiO_2 Powders", *Journal of the American Ceramic Society*, **1982**, 65 (12), C199-C201.

27. Hench, L.L. and West, J.K., "The Sol-Gel Process", *Chemical Reviews*, **1990**, 90 (1), 33-72.

28. Cushing, B.L., Kolesnichenko, V.L., and O'Connor, C.J., "Recent advances in the liquid-phase syntheses of inorganic nanoparticles", *Chemical Reviews*, **2004**, 104 (9), 3893-3946.

29. Davis, M.E. and Lobo, R.F., "Zeolite and Molecular-Sieve Synthesis", *Chemistry of Materials*, **1992**, 4 (4), 756-768.

30. Ying, J.Y., Mehnert, C.P., and Wong, M.S., "Synthesis and applications of supramolecular-templated mesoporous materials", *Angewandte Chemie-International Edition*, **1999**, 38 (1-2), 56-77.

31. Sayari, A., Danumah, C., and Moudrakovski, I.L., "Boron-Modified MCM-41 Mesoporous Molecular-Sieves", *Chemistry of Materials*, **1995**, 7 (5), 813-815.

32. Hoffmann, F., Cornelius, M., Morell, J., and Froba, M., "Silica-based mesoporous organic-inorganic hybrid materials", *Angewandte Chemie-International Edition*, **2006**, 45 (20), 3216-3251.

33. Vartuli, J.C., Schmitt, K.D., Kresge, C.T., Roth, W.J., Leonowicz, M.E., Mccullen, S.B., Hellring, S.D., Beck, J.S., Schlenker, J.L., Olson, D.H., and Sheppard, E.W., "Effect of Surfactant Silica Molar Ratios on the Formation of Mesoporous Molecular-Sieves - Inorganic Mimicry of Surfactant Liquid-Crystal Phases and Mechanistic Implications", *Chemistry of Materials*, **1994**, 6 (12), 2317-2326.

34. Forster, S. and Antonietti, M., "Amphiphilic block copolymers in structure-controlled nanomaterial hybrids", *Advanced Materials*, **1998**, 10 (3), 195.

35. Kramer, E., Forster, S., Goltner, C., and Antonietti, M., "Synthesis of nanoporous silica with new pore morphologies by templating the assemblies of ionic block copolymers", *Langmuir*, **1998**, 14 (8), 2027-2031.

36. Zhao, D., Yang, P., Melosh, N., Feng, J., Chmelka, B.F., and Stucky, G.D., "Continuous mesoporous silica films with highly ordered large pore structures", *Advanced Materials*, **1998**, 10 (16), 1380-1385.

37. Zhao, D.Y., Feng, J.L., Huo, Q.S., Melosh, N., Fredrickson, G.H., Chmelka, B.F., and Stucky, G.D., "Triblock copolymer syntheses of mesoporous silica with periodic 50 to 300 angstrom pores", *Science*, **1998**, 279 (5350), 548-552.

38. Antonelli, D.M. and Ying, J.Y., "Synthesis of Hexagonally Packed Mesoporous TiO_2 by a Modified Sol-Gel Method", *Angewandte Chemie-International Edition in English*, **1995**, 34 (18), 2014-2017.

39. Kim, A., Bruinsma, P., Chen, Y., Wang, L.Q., and Liu, J., "Amphoteric surfactant templating route for mesoporous zirconia", *Chemical Communications*, **1997**, (2), 161-162.

40. Yang, P.D., Zhao, D.Y., Margolese, D.I., Chmelka, B.F., and Stucky, G.D., "Block

copolymer templating syntheses of mesoporous metal oxides with large ordering lengths and semicrystalline framework", *Chemistry of Materials*, **1999**, 11 (10), 2813-2826.

41. Soler-Illia, G.J.D.A., Crepaldi, E.L., Grosso, D., and Sanchez, C., "Block copolymer-templated mesoporous oxides", *Current Opinion in Colloid & Interface Science*, **2003**, 8 (1), 109-126.

42. Calleja, G., Serrano, D.P., Sanz, R., Pizarro, P., and Garcia, A., "Study on the synthesis of high-surface-area mesoporous TiO_2 in the presence of nonionic surfactants", *Industrial & Engineering Chemistry Research*, **2004**, 43 (10), 2485-2492.

43. Wu, L., Yu, J.C., Wang, X.C., Zhang, L.Z., and Yu, J.G., "Characterization of mesoporous nanocrystalline TiO_2 photocatalysts synthesized via a sol-solvothermal process at a low temperature", *Journal of Solid State Chemistry*, **2005**, 178 (1), 321-328.

44. Yue, Y.H. and Gao, Z., "Synthesis of mesoporous TiO_2 with a crystalline framework", *Chemical Communications*, **2000**, (18), 1755-1756.

45. Kluson, P., Kacer, P., Cajthaml, T., and Kalaji, M., "Preparation of titania mesoporous materials using a surfactant-mediated sol-gel method", *Journal of Materials Chemistry*, **2001**, 11 (2), 644-651.

46. Yu, J.G., Wang, G.H., Cheng, B., and Zhou, M.H., "Effects of hydrothermal temperature and time on the photocatalytic activity and microstructures of bimodal mesoporous TiO_2 powders", *Applied Catalysis B-Environmental*, **2007**, 69 (3-4), 171-180.

47. Wu, M.M., Lin, G., Chen, D.H., Wang, G.G., He, D., Feng, S.H., and Xu, R.R., "Sol-hydrothermal synthesis and hydrothermally structural evolution of nanocrystal titanium dioxide", *Chemistry of Materials*, **2002**, 14 (5), 1974-1980.

48. Peng, T.Y., Zhao, D., Dai, K., Shi, W., and Hirao, K., "Synthesis of titanium dioxide nanoparticles with mesoporous anatase wall and high photocatalytic activity", *Journal of Physical Chemistry B*, **2005**, 109 (11), 4947-4952.

49. Wang, H.W., Kuo, C.H., Lin, H.C., Kuo, I.T., and Cheng, C.F., "Rapid formation of active mesoporous TiO_2 photocatalysts via micelle in a microwave hydrothermal process", *Journal of the American Ceramic Society*, **2006**, 89 (11), 3388-3392.

50. Wang, Y.Q., Tang, X.H., Yin, L.X., Huang, W.P., Hacohen, Y.R., and Gedanken, A., "Sonochemical synthesis of mesoporous titanium oxide with wormhole-like framework structures", *Advanced Materials*, **2000**, 12 (16), 1183-1186.

51. Yu, J.C., Zhang, L.Z., and Yu, J.G., "Direct sonochemical preparation and characterization of highly active mesoporous TiO_2 with a bicrystalline framework", *Chemistry of Materials*, **2002**, 14 (11), 4647-4653.

52. Soler-Illia, G.J.D.A., Louis, A., and Sanchez, C., "Synthesis and characterization of mesostructured titania-based materials through evaporation-induced self-assembly", *Chemistry of Materials*, **2002**, 14 (2), 750-759.

53. Liu, K.S., Fu, H.G., Shi, K.H., Xin, B.F., Jing, L.Q., and Zhou, W., "Hydrophilicity and formation mechanism of large-pore mesoporous TiO_2 thin films with tunable pore diameters", *Nanotechnology*, **2006**, 17 (15), 3641-3648.

54. Beyers, E., Cool, P., and Vansant, E.F., "Stabilisation of mesoporous TiO_2 by different bases influencing the photocatalytic activity", *Microporous and Mesoporous Materials*, **2007**, 99 (1-2), 112-117.

55. Antonelli, D.M. and Ying, J.Y., "Synthesis and characterization of hexagonally packed mesoporous tantalum oxide molecular sieves", *Chemistry of Materials*, **1996**, 8 (4), 874-881.

56. Yoshitake, H., Sugihara, T., and Tatsumi, T., "Preparation of wormhole-like mesoporous TiO_2 with an extremely large surface area and stabilization of its surface by chemical vapor deposition", *Chemistry of Materials*, **2002**, 14 (3), 1023-1029.

57. On, D.T., "A simple route for the synthesis of mesostructured lamellar and hexagonal phosphorus-free titania (TiO_2)", *Langmuir*, **1999**, 15 (25), 8561-8564.

58. Zheng, J.Y., Pang, J.B., Qiu, K.Y., and Wei, Y., "Synthesis and characterization of mesoporous titania and silica-titania materials by urea templated sol-gel reactions", *Microporous and Mesoporous Materials*, **2001**, 49 (1-3), 189-195.

59. Soler-Illia, G.J.D.A., Scolan, E., Louis, A., Albouy, P.A., and Sanchez, C., "Design of meso-structured titanium oxo based hybrid organic-inorganic networks", *New Journal of Chemistry*, **2001**, 25 (1), 156-165.

60. Miller, J.B. and Ko, E.I., "Control of mixed oxide textural and acidic properties by the sol-gel method", *Catalysis Today*, **1997**, 35 (3), 269-292.

61. Gao, X.T. and Wachs, I.E., "Titania-silica as catalysts: molecular structural characteristics and physico-chemical properties", *Catalysis Today*, **1999**, 51 (2), 233-254.

62. Yu, J.C., Lin, J., and Kwok, R.W.M., "$Ti_{1-x}Zr_xO_2$ solid solutions for the photocatalytic degradation of acetone in air", *Journal of Physical Chemistry B*, **1998**, 102 (26), 5094-5098.

63. Lukac, J., Klementova, M., Bezdicka, P., Bakardjieva, S., Subrt, J., Szatmary, L., Bastl, Z., and Jirkovsky, J., "Influence of Zr as TiO_2 doping ion on photocatalytic degradation of 4-chlorophenol", *Applied Catalysis B-Environmental*, **2007**, 74 (1-2), 83-91.

64. Gao, B.F., Lim, T.M., Subagio, D.P., and Lim, T.T., "Zr-doped TiO_2 for enhanced photocatalytic degradation of bisphenol A", *Applied Catalysis a-General*, **2010**, 375 (1), 107-115.

65. Schattka, J.H., Shchukin, D.G., Jia, J.G., Antonietti, M., and Caruso, R.A., "Photocatalytic activities of porous titania and titania/zirconia structures formed by using a polymer gel templating", *Chemistry of Materials*, **2002**, 14 (12), 5103-5108.

66. Zhou, W., Liu, K.S., Fu, H.G., Pan, K., Zhang, L.L., Wang, L., and Sun, C.C., "Multi-modal mesoporous TiO_2-ZrO_2 composites with high photocatalytic activity and hydrophilicity", *Nanotechnology*, **2008**, 19 (3), -.

67. Sekulic, J., Magraso, A., ten Elshof, J.E., and Blank, D.H.A., "Influence of ZrO_2 addition on microstructure and liquid permeability of mesoporous TiO_2 membranes", *Microporous and Mesoporous Materials*, **2004**, 72 (1-3), 49-57.

68. Yuan, Q., Liu, Y., Li, L.L., Li, Z.X., Fang, C.J., Duan, W.T., Li, X.G., and Yan, C.H., "Highly ordered mesoporous titania-zirconia photocatalyst for applications in degradation of rhodamine-B and hydrogen evolution", *Microporous and Mesoporous Materials*, **2009**, 124 (1-3), 169-178.

69. Serrano, D.P., Calleja, G., Sanz, R., and Pizarro, P., "Development of crystallinity and photocatalytic properties in porous TiO_2 by mild acid treatment", *Journal of Materials Chemistry*, **2007**, 17 (12), 1178-1187.

70. Ao, Y.H., Xu, J.J., and Fu, D.G., "Study on the effect of different acids on the structure and photocatalytic activity of mesoporous titania", *Applied Surface Science*, **2009**, 256 (1), 239-245.

71. Kartini, I., Meredith, P., Da Costa, J.C.D., and Lu, G.Q., "A novel route to the synthesis of mesoporous Titania with full anatase nanocrystalline domains", *Journal of Sol-Gel Science and Technology*, **2004**, 31 (1-3), 185-189.

72. Tan, R.Q., He, Y., Zhu, Y.F., Xu, B.Q., and Cao, L.L., "Hydrothermal preparation of mesoporous TiO_2 powder from $Ti(SO_4)_2$ with poly(ethylene glycol) as template", *Journal of Materials Science*, **2003**, 38 (19), 3973-3978.

73. Kim, D.S. and Kwak, S.Y., "The hydrothermal synthesis of mesoporous TiO_2 with high crystallinity, thermal stability, large surface area, and enhanced photocatalytic activity", *Applied Catalysis a-General*, **2007**, 323 110-118.

74. Liu, K.S., Fu, H.G., Shi, K.Y., Xiao, F.S., Jing, L.Q., and Xin, B.F., "Preparation of large-pore mesoporous nanocrystalline TiO_2 thin films with tailored pore diameters", *Journal of Physical Chemistry B*, **2005**, 109 (40), 18719-18722.

75. Lu, Y.F., Fan, H.Y., Stump, A., Ward, T.L., Rieker, T., and Brinker, C.J., "Aerosol-assisted self-assembly of mesostructured spherical nanoparticles", *Nature*, **1999**, 398 (6724), 223-226.

76. Mann, S. and Ozin, G.A., "Synthesis of inorganic materials with complex form", *Nature*, **1996**, 382 (6589), 313-318.

77. Raman, N.K., Anderson, M.T., and Brinker, C.J., "Template-based approaches to the preparation of amorphous, nanoporous silicas", *Chemistry of Materials*, **1996**, 8 (8),

1682-1701.

78. Choi, W.Y., Termin, A., and Hoffmann, M.R., "The Role of Metal-Ion Dopants in Quantum-Sized TiO_2-Correlation between Photoreactivity and Charge-Carrier Recombination Dynamics", *Journal of Physical Chemistry*, **1994**, 98 (51), 13669-13679.

79. Dvoranova, D., Brezova, V., Mazur, M., and Malati, M.A., "Investigations of metal-doped titanium dioxide photocatalysts", *Applied Catalysis B-Environmental*, **2002**, 37 (2), 91-105.

80. Di Paola, A., Garcia-Lopez, E., Ikeda, S., Marci, G., Ohtani, B., and Palmisano, L., "Photocatalytic degradation of organic compounds in aqueous systems by transition metal doped polycrystalline TiO_2", *Catalysis Today*, **2002**, 75 (1-4), 87-93.

81. Lin, S.D., Bollinger, M., and Vannice, M.A., "Low-Temperature CO Oxidation over Au/TiO_2 and Au/SiO_2 Catalysts", *Catalysis Letters*, **1993**, 17 (3-4), 245-262.

82. Herrmann, J.M., Tahiri, H., AitIchou, Y., Lassaletta, G., GonzalezElipe, A.R., and Fernandez, A., "Characterization and photocatalytic activity in aqueous medium of TiO_2 and $Ag-TiO_2$ coatings on quartz", *Applied Catalysis B-Environmental*, **1997**, 13 (3-4), 219-228.

83. Subramanian, V., Wolf, E.E., and Kamat, P.V., "Catalysis with TiO_2/gold nanocomposites. Effect of metal particle size on the Fermi level equilibration", *Journal of the American Chemical Society*, **2004**, 126 (15), 4943-4950.

84. Tsubota, S., Cunningham, D.A.H., Bando, Y., and Haruta, M., "Preparation of nanometer gold strongly interacted with TiO_2 and the structure sensitivity in low-temperature oxidation of CO", *Preparation of Catalysts Vi*, **1995**, 91 227-235.

85. Comotti, M., Li, W.C., Spliethoff, B., and Schuth, F., "Support effect in high activity gold catalysts for CO oxidation", *Journal of the American Chemical Society*, **2006**, 128 (3), 917-924.

86. Wolf, A. and Schuth, F., "A systematic study of the synthesis conditions for the preparation of highly active gold catalysts", *Applied Catalysis a-General*, **2002**, 226 (1-2), 1-13.

87. Grunwaldt, J.D., Kiener, C., Wogerbauer, C., and Baiker, A., "Preparation of supported gold catalysts for low-temperature CO oxidation via "size-controlled" gold colloids", *Journal of Catalysis*, **1999**, 181 (2), 223-232.

88. Azizi, Y., Pitchon, V., and Petit, C., "Effect of support parameters on activity of gold catalysts: Studies of ZrO_2, TiO_2 and mixture", *Applied Catalysis a-General*, **2010**, 385 (1-2), 170-177.

89. Usubharatana, P., McMartin, D., Veawab, A., and Tontiwachwuthikul, P., "Photocatalytic process for CO_2 emission reduction from industrial flue gas streams", *Industrial & Engineering Chemistry Research*, **2006**, 45 (8), 2558-2568.

90.   Riemer, P., "Greenhouse gas mitigation technologies, an overview of the CO_2 capture, storage and future activities of the IEA Greenhouse gas R&D programme", *Energy Conversion and Management*, **1996**, 37 (6-8), 665-670.

91.   Meisen, A. and Shuai, X.S., "Research and development issues in CO_2 capture", *Energy Conversion and Management*, **1997**, 38 S37-S42.

92.   Kosugi, T., Hayashi, A., Matsumoto, T., Akimoto, K., Tokimatsu, K., Yoshida, H., Tomoda, T., and Kaya, Y., "Time to realization: Evaluation of CO_2 capture technology R&Ds by GERT (Graphical evaluation and review technique) analysese", *Energy*, **2004**, 29 (9-10), 1297-1308.

93.   Dijkstra, J.W. and Jansen, D., "Novel concepts for CO_2 capture", *Energy*, **2004**, 29 (9-10), 1249-1257.

94.   Sakakura, T., Choi, J.C., and Yasuda, H., "Transformation of carbon dioxide", *Chemical Reviews*, **2007**, 107 (6), 2365-2387.

95.   Graetzel, M., "*Energy Resources through Photochemistry and Catalysis*". **1983** New York: Academic Press.

96.   Koci, K., Obalova, L., and Lacny, Z., "Photocatalytic reduction of CO_2 over TiO_2 based catalysts", *Chemical Papers*, **2008**, 62 (1), 1-9.

97.   Inoue, T., Fujishima, A., Konishi, S., and Honda, K., "Photoelectrocatalytic Reduction of Carbon-Dioxide in Aqueous Suspensions of Semiconductor Powders", *Nature*, **1979**, 277 (5698), 637-638.

98.   Kaneco, S., Kurimoto, H., Shimizu, Y., Ohta, K., and Mizuno, T., "Photocatalytic reduction of CO_2 using TiO_2 powders in supercritical fluid CO_2", *Energy*, **1999**, 24 (1), 21-30.

99.   Mizuno, T., Adachi, K., Ohta, K., and Saji, A., "Effect of CO_2 pressure on photocatalytic reduction of CO_2 using TiO_2 in aqueous solutions", *Journal of Photochemistry and Photobiology a-Chemistry*, **1996**, 98 (1-2), 87-90.

100.   Anpo, M., Yamashita, H., Ichihashi, Y., and Ehara, S., "Photocatalytic Reduction of Co2 with H2o on Various Titanium-Oxide Catalysts", *Journal of Electroanalytical Chemistry*, **1995**, 396 (1-2), 21-26.

101.   Liu, B.J., Torimoto, T., Matsumoto, H., and Yoneyama, H., "Effect of solvents on photocatalytic reduction of carbon dioxide using TiO_2 nanocrystal photocatalyst embedded in SiO_2 matrices", *Journal of Photochemistry and Photobiology a-Chemistry*, **1997**, 108 (2-3), 187-192.

102.   Tseng, I.H., Chang, W.C., and Wu, J.C.S., "Photoreduction of CO_2 using sol-gel derived titania and titania-supported copper catalysts", *Applied Catalysis B-Environmental*, **2002**, 37 (1), 37-48.

103.   Halmann, M., Katzir, V., Borgarello, E., and Kiwi, J., "Photoassisted Carbon-Dioxide Reduction on Aqueous Suspensions of Titanium-Dioxide", *Solar Energy Materials*,

1984, 10 (1), 85-91.

104. Anpo, M. and Yamashita, H., "*Heterogeneous   Photocatalysis*". **1997**, London, U.K. Wiley. 133.

105. Yamashita, H., Nishiguchi, H., Kamada, N., Anpo, M., Teraoka, Y., Hatano, H., Ehara, S., Kikui, K., Palmisano, L., Sclafani, A., Schiavello, M., and Fox, M.A., "Photocatalytic Reduction of CO_2 with H_2O on TiO_2 and Cu/TO_2 Catalysts", *Research on Chemical Intermediates*, **1994**, 20 (8), 815-823.

106. Yang, C.C., Yu, Y.H., van der Linden, B., Wu, J.C.S., and Mul, G., "Artificial Photosynthesis over Crystalline TiO_2-Based Catalysts: Fact or Fiction?", *Journal of the American Chemical Society*, **2010**, 132 (24), 8398-8406.

107. Ishitani, O., Inoue, C., Suzuki, Y., and Ibusuki, T., "Photocatalytic Reduction of Carbon-Dioxide to Methane and Acetic-Acid by an Aqueous Suspension of Metal-Deposited TiO_2", *Journal of Photochemistry and Photobiology a-Chemistry*, **1993**, 72 (3), 269-271.

108. Zhang, Q.H., Han, W.D., Hong, Y.J., and Yu, J.G., "Photocatalytic reduction of CO_2 with H2O on Pt-loaded TiO_2 catalyst", *Catalysis Today*, **2009**, 148 (3-4), 335-340.

109. Kaneco, S., Kurimoto, H., Ohta, K., Mizuno, T., and Saji, A., "Photocatalytic reduction of CO_2 using TiO_2 powders in liquid CO_2 medium", *Journal of Photochemistry and Photobiology a-Chemistry*, **1997**, 109 (1), 59-63.

110. Kaneco, S., Shimizu, Y., Ohta, K., and Mizuno, T., "Photocatalytic reduction of high pressure carbon dioxide using TiO_2 powders with a positive hole scavenger", *Journal of Photochemistry and Photobiology a-Chemistry*, **1998**, 115 (3), 223-226.

111. Yamashita, H., Fujii, Y., Ichihashi, Y., Zhang, S.G., Ikeue, K., Park, D.R., Koyano, K., Tatsumi, T., and Anpo, M., "Selective formation of CH_3OH in the photocatalytic reduction of CO_2 with H_2O on titanium oxides highly dispersed within zeolites and mesoporous molecular sieves", *Catalysis Today*, **1998**, 45 (1-4), 221-227.

112. Kohno, Y., Hayashi, H., Takenaka, S., Tanaka, T., Funabiki, T., and Yoshida, S., "Photo-enhanced reduction of carbon dioxide with hydrogen over Rh/TiO_2", *Journal of Photochemistry and Photobiology a-Chemistry*, **1999**, 126 (1-3), 117-123.

113. Tseng, I.H., Wu, J.C.S., and Chou, H.Y., "Effects of sol-gel procedures on the photocatalysis of Cu/TiO_2 in CO_2 photoreduction", *Journal of Catalysis*, **2004**, 221 (2), 432-440.

114. Nguyen, T.V. and Wu, J.C.S., "Photoreduction of CO_2 in an optical-fiber photoreactor: Effects of metals addition and catalyst carrier", *Applied Catalysis a-General*, **2008**, 335 (1), 112-120.

115. Nguyen, T.V., Wu, J.C.S., and Chiou, C.H., "Photoreduction of CO_2 over Ruthenium dye-sensitized TiO_2-based catalysts under concentrated natural sunlight", *Catalysis Communications*, **2008**, 9 (10), 2073-2076.

116. Chang, S.M. and Doong, R.A., "Characterization of Zr-doped TiO_2 nanocrystals prepared by a nonhydrolytic sol-gel method at high temperatures", *Journal of Physical Chemistry B*, **2006**, 110 (42), 20808-20814.

117. Kumar, K.N.P., Kumar, J., and Keizer, K., "Effect of Peptization on Densification and Phase-Transformation Behavior of Sol Gel-Derived Nanostructured Titania", *Journal of the American Ceramic Society*, **1994**, 77 (5), 1396-1400.

118. Ravikovitch, P.I. and Neimark, A.V., "Experimental confirmation of different mechanisms of evaporation from ink-bottle type pores: Equilibrium, pore blocking, and cavitation", *Langmuir*, **2002**, 18 (25), 9830-9837.

119. Luca, V., "Comparison of Size-Dependent Structural and Electronic Properties of Anatase and Rutile Nanoparticles", *Journal of Physical Chemistry C*, **2009**, 113 (16), 6367-6380.

120. Dimitrijevic, N.M., Vijayan, B.K., Poluektov, O.G., Rajh, T., Gray, K.A., He, H.Y., and Zapol, P., "Role of Water and Carbonates in Photocatalytic Transformation of CO_2 to CH_4 on Titania", *Journal of the American Chemical Society*, **2011**, 133 (11), 3964-3971.

Appendix A. Calibration curve

(a)

$$y = 278830x - 2228$$
$$R^2 = 0.9945$$
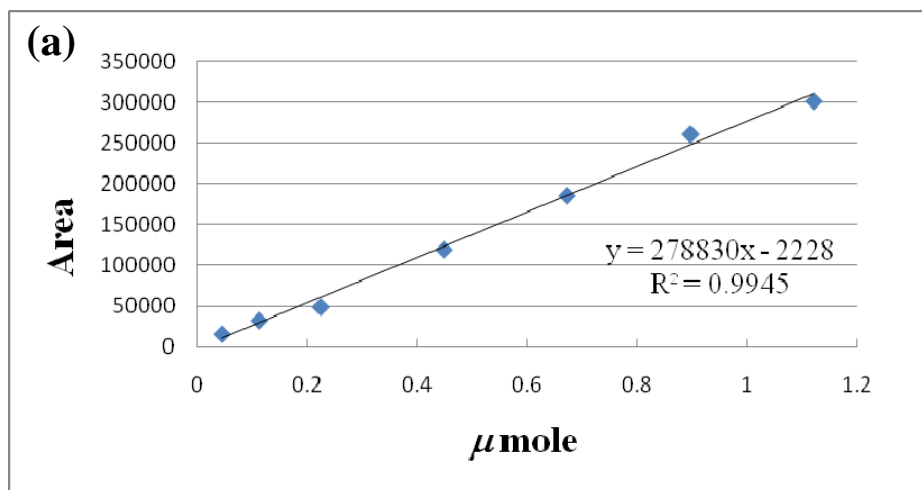
(b)

RT: 0.00 - 3.99
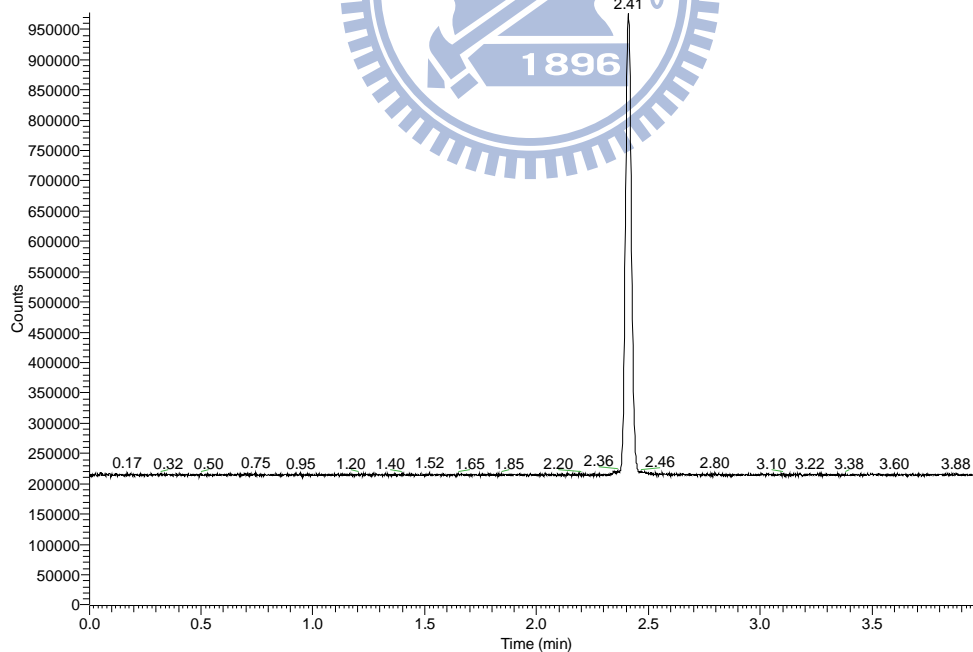
NL:
9.77E5
FID
Analog 2
CH4-
500uL-1-
2010-10-27

Appendix A. (a) The calibration curve of CH_4 and (b) FID pattern.

Appendix B. XPS patterns of catalysts
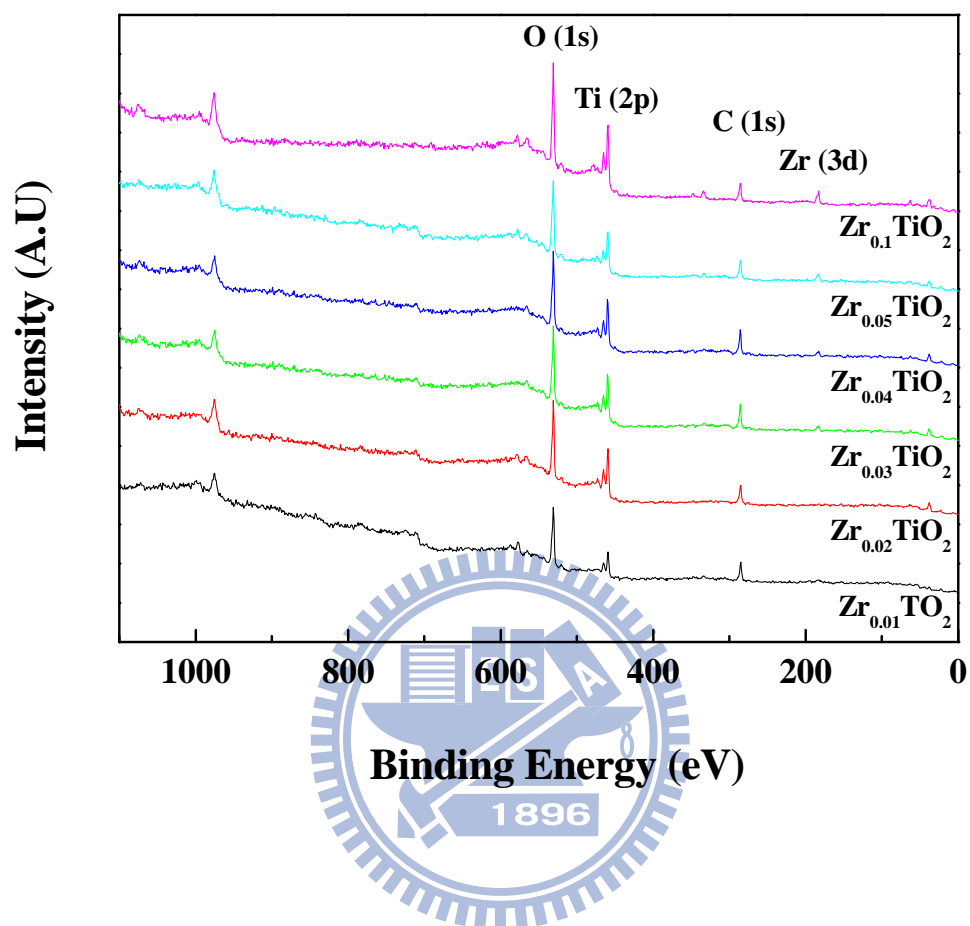
Appendix B-1. The wide-range scanned XPS spectra of Zr_xTiO_2 samples.
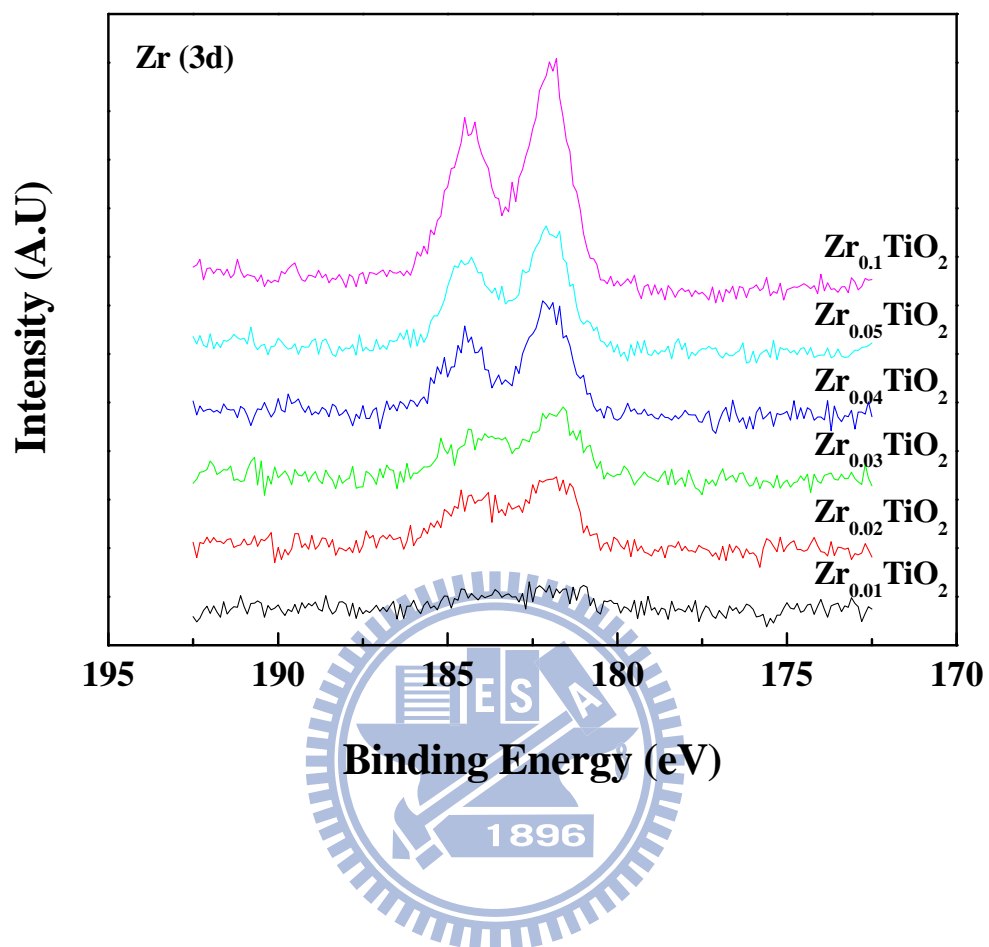
Appendix B-2. The high resolution scanned of Zr (3d) XPS spectra of Zr_xTiO_2 samples.
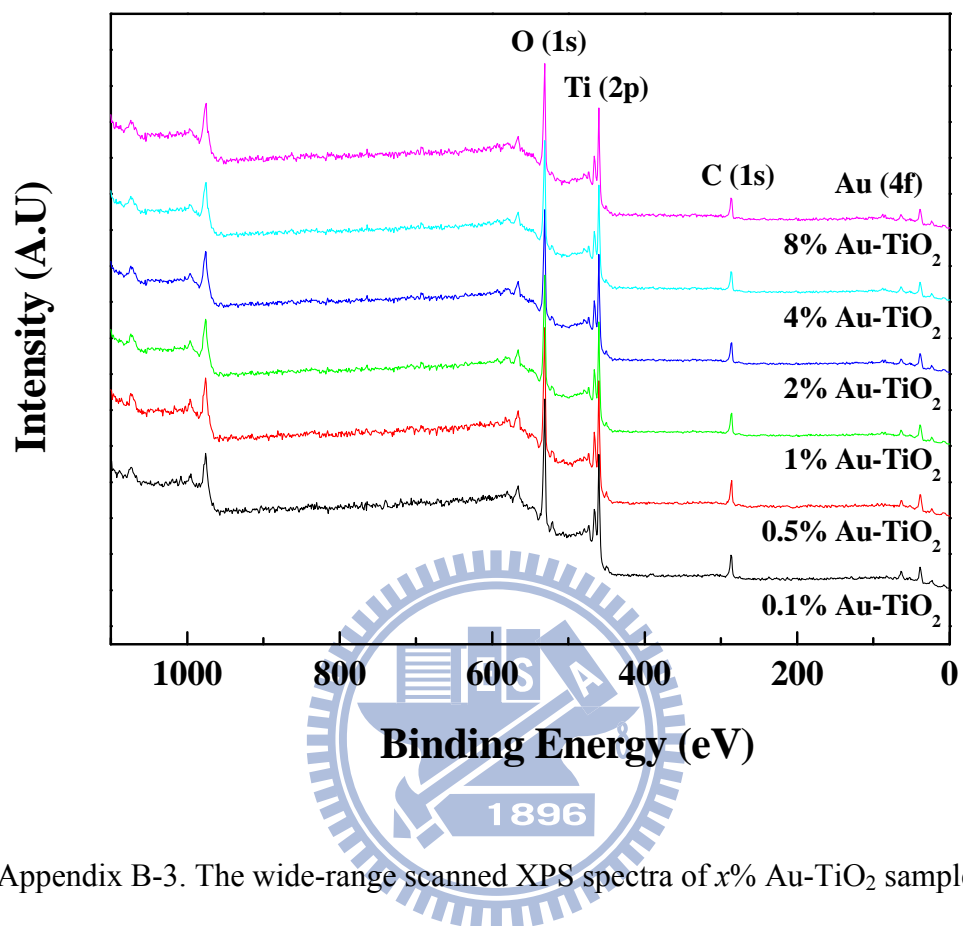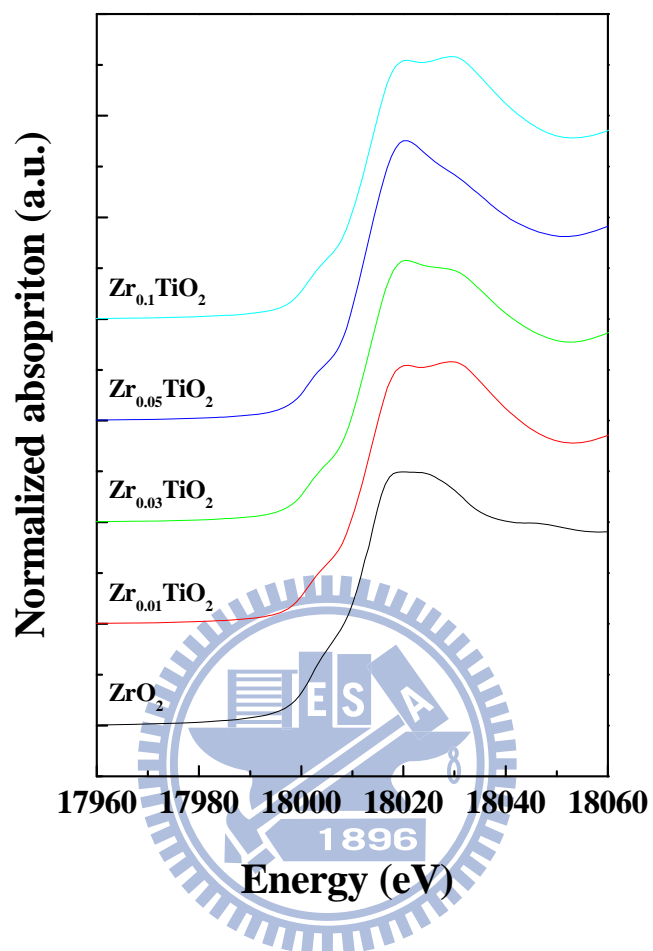
Appendix B-3. The wide-range scanned XPS spectra of x% Au-TiO$_2$ samples.

Appendix C. TEM images of catalysts
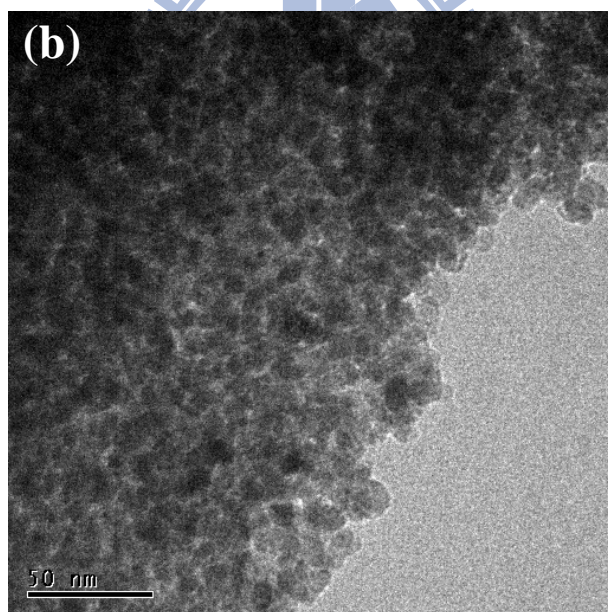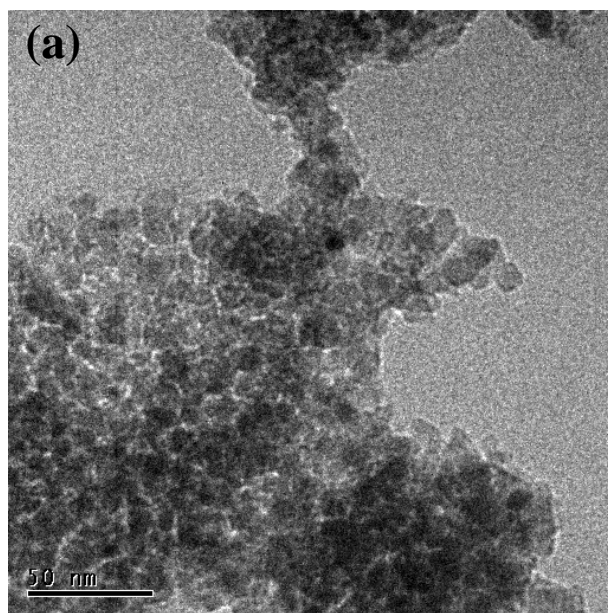
Appendix C. TEM images of (a) $Zr_{0.05}TiO_2$ and (b) $Zr_{0.1}TiO_2$.

Appendix D. Zr K-edge XAS spectra of catalysts

Appendix D-1. Complete Zr K-edge XANES spectra of mesoporous ZrO_2 and Zr_xTiO_2 samples.
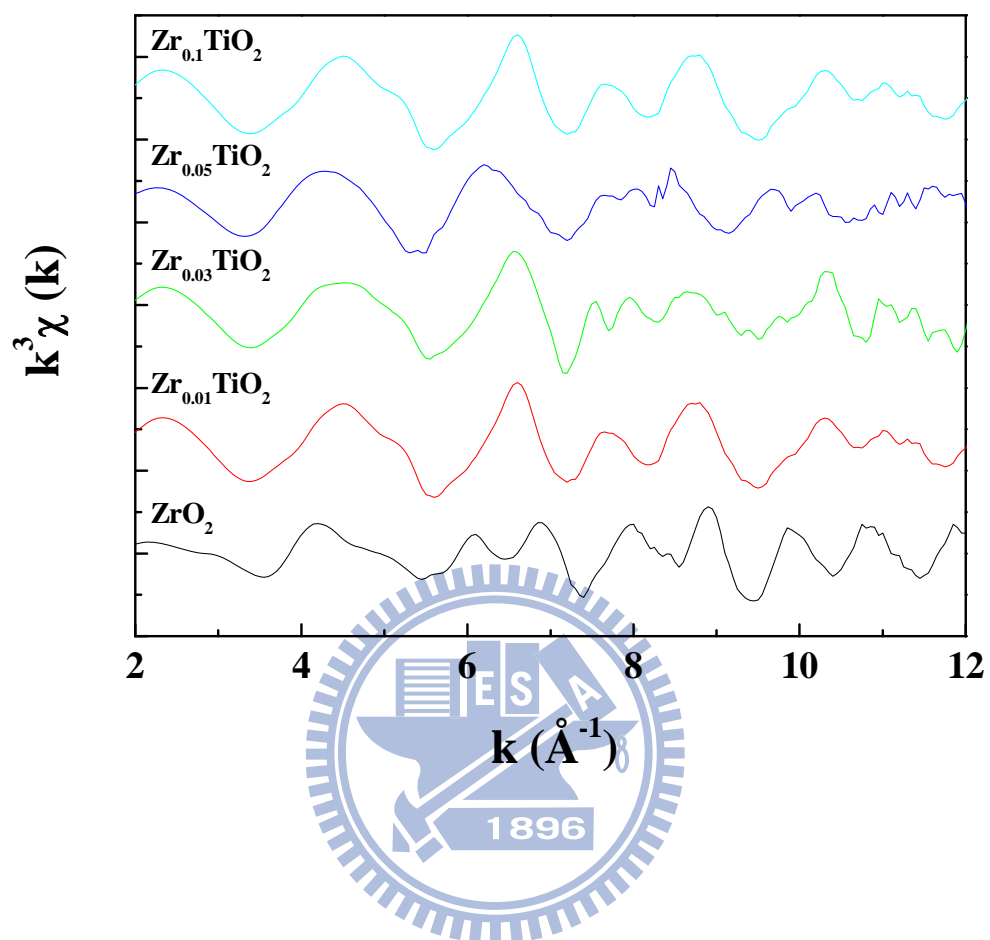
Appendix D-2. Zr K-edge EXAFS spectra of mesoporous ZrO_2 and Zr_xTiO_2 samples.

Appendix E. CO_2 adsorption-desorption isotherm of catalysts
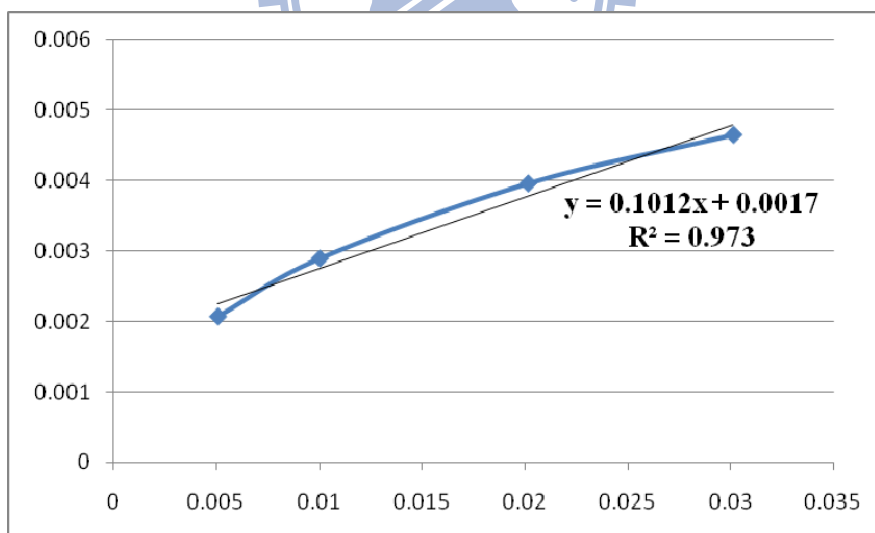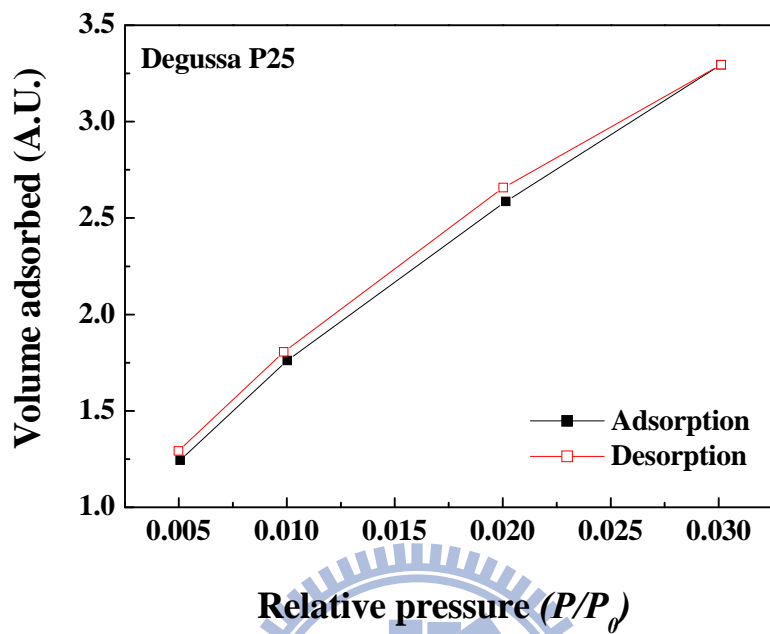
Appendix E-1. CO_2 adsorption and desorption isotherm of Degussa P25.

Appendix E-2. The CO_2 adsorption/desorption isotherm reports of Degussa P25.

Relative Pressure (P/P_0)	Quantity Adsorbed (cm^3/g STP)	Quantity Adsorbed (mg/g STP)
0.5×10^{-2}	1.24	2.44
1.0×10^{-2}	1.76	3.46
2.0×10^{-2}	2.59	5.08
3.0×10^{-2}	3.29	6.47
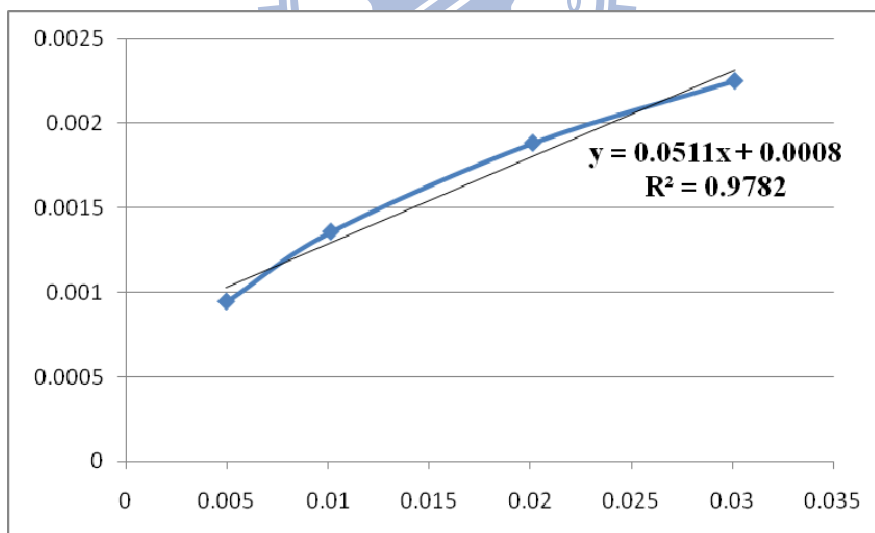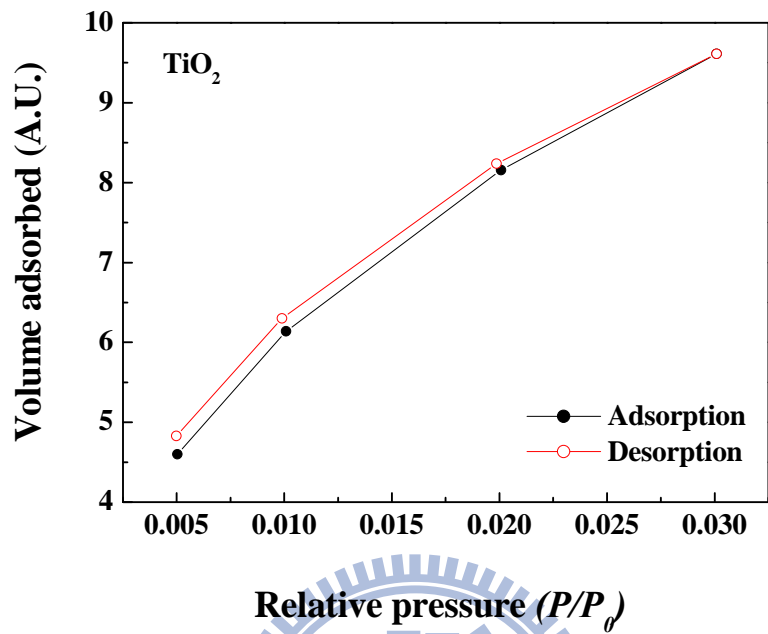
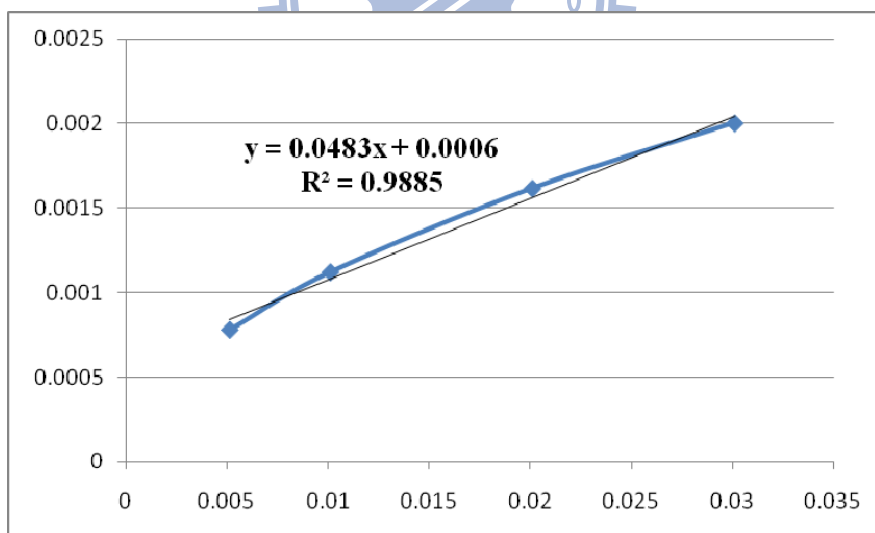Appendix E-3. CO_2 adsorption and desorption isotherm of TiO_2.

Appendix E-4. The CO_2 adsorption/desorption isotherm reports of TiO_2.

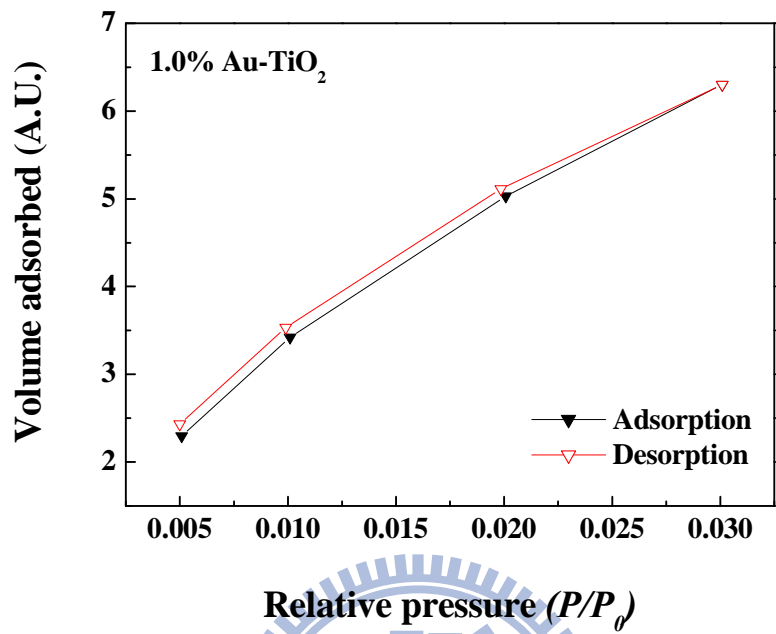| Relative Pressure (P/P_0)	Quantity Adsorbed (cm^3/g STP)	Quantity Adsorbed (mg/g STP)
0.5×10^{-2}	2.67	5.25
1.0×10^{-2}	3.80	7.45
2.0×10^{-2}	5.44	10.68
3.0×10^{-2}	6.81	13.37
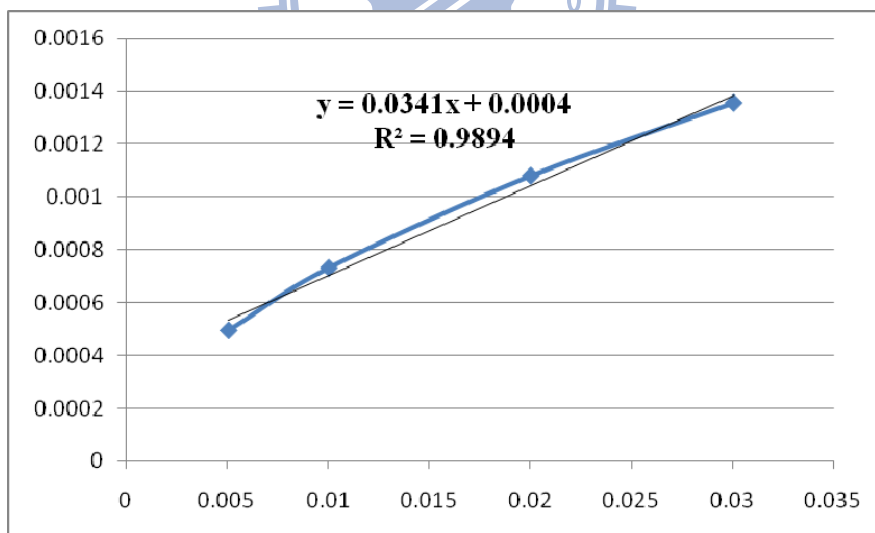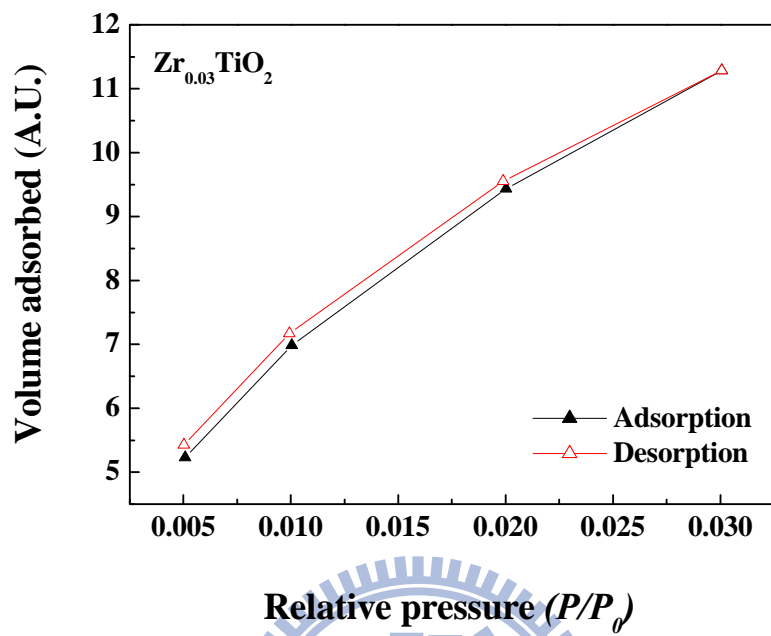
Appendix E-5. CO_2 adsorption and desorption isotherm of $Zr_{0.03}TiO_2$.

Appendix E-6. The CO_2 adsorption/desorption isotherm reports of $Zr_{0.03}TiO_2$.

| Relative Pressure (P/P_0)	Quantity Adsorbed (cm^3/g STP)	Quantity Adsorbed (mg/g STP)
0.5×10^{-2}	5.23	10.27
1.0×10^{-2}	6.99	13.72
2.0×10^{-2}	9.44	18.54
3.0×10^{-2}	11.28	22.16

Appendix E-7. CO_2 adsorption and desorption isotherm of 1.0% Au-TiO$_2$.

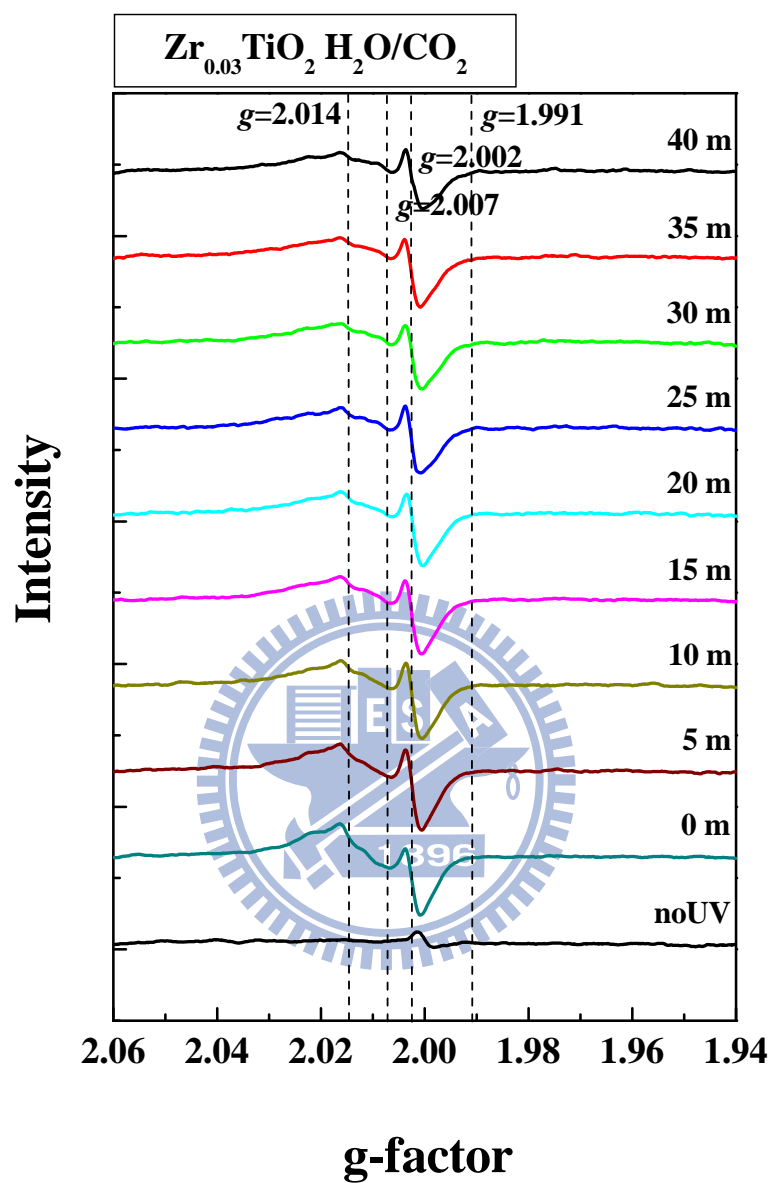Appendix E-8. The CO_2 adsorption/desorption isotherm reports of 1.0% Au-TiO$_2$.

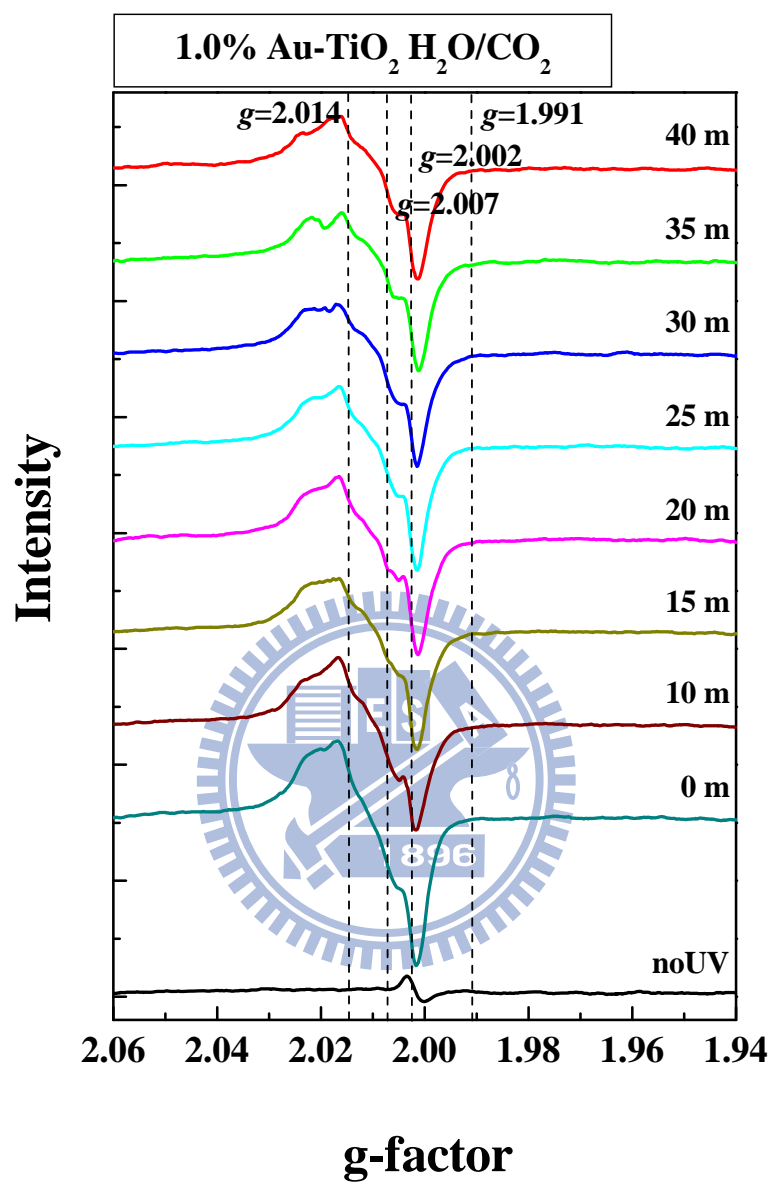| Relative Pressure (P/P_0)	Quantity Adsorbed (cm^3/g STP)	Quantity Adsorbed (mg/g STP)
0.5×10^{-2}	3.34	6.56
1.0×10^{-2}	4.58	9.00
2.0×10^{-2}	6.33	12.42
3.0×10^{-2}	7.65	15.03

Appendix F. CO$_2$ adsorption-desorption isotherm of catalysts
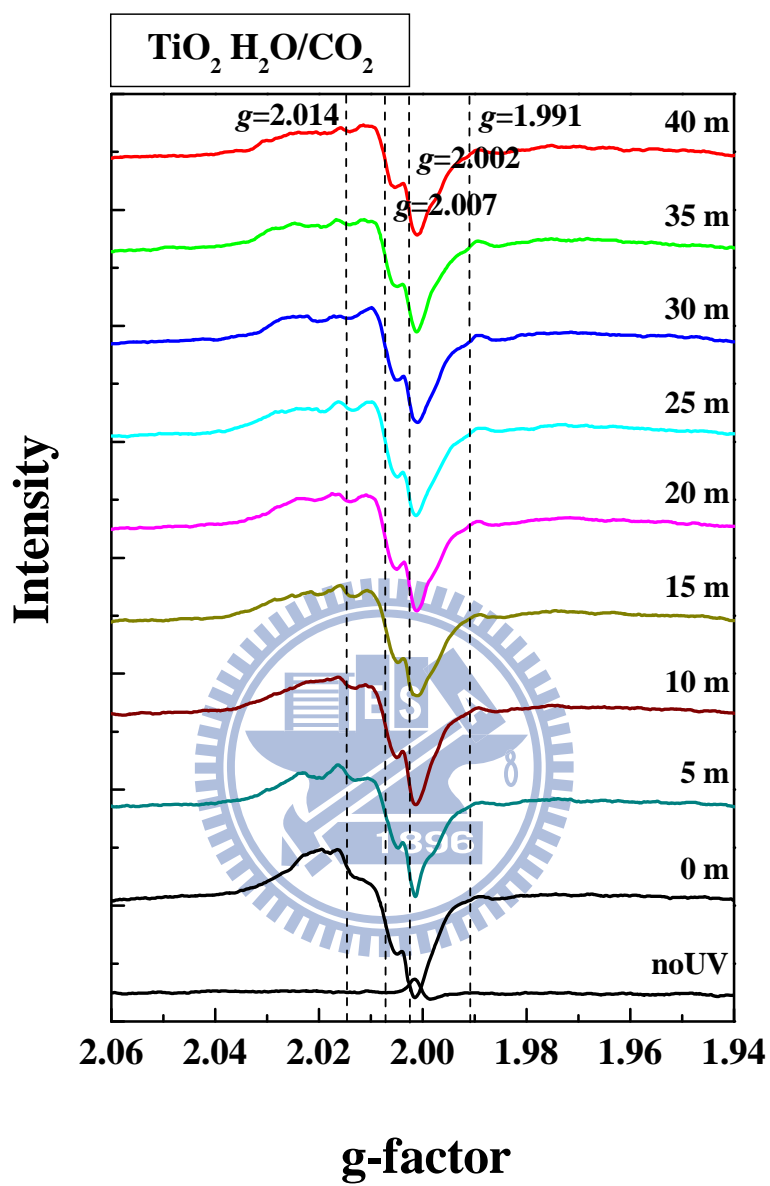
Appendix F-1. EPR spectra of mesoporus TiO$_2$ under UV irradiation at 77K with CO$_2$/H$_2$O.

Appendix F-2. EPR spectra of $Zr_{0.03}TiO_2$ under UV irradiation at 77K with CO_2/H_2O.

Appendix F-3. EPR spectra of 1.0% Au-TiO$_2$ under UV irradiation at 77K with CO$_2$/H$_2$O.